

Exploring the Effects of Catalysts in Li-O₂ Batteries

Zur Erlangung des akademischen Grades eines

DOKTORS DER NATURWISSENSCHAFTEN

(Dr. rer. nat.)

von der KIT-Fakultät für Chemie und Biowissenschaften
des Karlsruher Instituts für Technologie (KIT)

genehmigte

DISSERTATION

von

M.Sc. Lihua Zhu

aus

Shandong, China

Dekan: Prof. Dr. Reinhard Fischer

Referent: Prof. Dr. Helmut Ehrenberg

Korreferent: Prof. Dr. Stefano Passerini

Tag der mündlichen Prüfung: 24.07.2019

Die vorliegende Arbeit wurde im Zeitraum vom Oct. 2015 bis Juli 2019 am Institut für Organische Chemie der Fakultät für Chemie und Biowissenschaften am Karlsruher Institut für Technologie (KIT) unter der Leitung von Prof. Dr. Helmut Ehrenberg angefertigt.

Hiermit versichere ich, die vorliegende Arbeit selbstständig verfasst und keine anderen als die angegebenen Quellen und Hilfsmittel verwendet sowie Zitate kenntlich gemacht zu haben. Die Dissertation wurde bisher an keiner anderen Hochschule oder Universität eingereicht.

Karlsruhe, den 03.06.2019

Lihua Zhu

Table of Contents

Abstract.....	1
Zusammenfassung	3
1. Introduction.....	6
1.1 Working principle of Li-O ₂ batteries.....	6
1.2 Challenges for Li-O ₂ batteries	8
1.3 The progress of oxygen electrodes for Li-O ₂ batteries.....	12
1.3.1 Carbon oxygen electrodes.....	13
1.3.2 Non-carbon oxygen electrodes	16
1.4 The effects of catalysts on the electrochemical performance of Li-O ₂ batteries.....	21
1.4.1 Solid catalysts.....	21
1.4.2 Soluble catalysts	26
2. Aim of the thesis	32
3. Experimental part.....	33
3.1 Material preparation.....	33
3.1.1 Preparation of porous carbon from biomass.....	33
3.1.2 MnO ₂ @rGO material preparation	33
3.1.3 Co ₃ O ₄ nanoplate preparation	33
3.2 Cell preparation and electrochemical measurements	34
3.2.1 Preparation of electrolytes	34
3.2.2 Preparation of electrodes	34
3.2.3 Battery preparation	35
3.2.4 Electrochemical measurements	35
3.3 Characterizations of the raw materials and the discharged/charged electrodes.....	36
3.3.1 Scanning electron microscope	36
3.3.2 X-ray diffraction	36
3.3.3 Raman spectroscopy	36
3.3.4 Thermal analysis.....	37
3.3.5 X-ray photoelectron spectroscopy	37
3.3.6 X-ray absorption near edge structure.....	37
3.3.7 Transmission electron microscopy	38

4. Results and discussion	39
4.1 Carbon materials as cathode for Li-O ₂ batteries	39
4.2 Improvements of electrochemical performance by solid catalysts	49
4.2.1 MnO ₂ as solid cathode catalyst for Li-O ₂ batteries	49
4.2.2 Co ₃ O ₄ as solid cathode catalyst for Li-O ₂ batteries	61
4.3 Improvements of electrochemical performance by soluble catalysts	75
5. Summary	87
6. Reference	92
7. Appendix	105
7.1 List of Abbreviations	105
7.2 Posters	107
7.3 Publications	107
8. Acknowledgements	108

Abstract

Abstract

Carbon materials are the most widely explored oxygen electrode materials for Li-O₂ batteries. In this thesis, we synthesized microporous honeycomb-like carbon from by-products through simple hydrothermal treatment and high temperature KOH activation process. The obtained porous carbon was applied as oxygen electrodes for Li-O₂ batteries. Li-O₂ batteries with the porous carbon electrodes exhibit low discharge capacity and poor capacity retention ability. The maximum discharge capacity is 1216 mAh g⁻¹ and the capacity is only 331 mAh g⁻¹ after nine cycles. This indicates that the porous carbon derived from wood (PCW) possesses poor electrochemical activity. The poor electrochemical activity can be ascribed to its small pore size and plentiful O-containing surface groups (O, 8.4 at%). The micropores are too small for the deposition of discharge products and easy to be blocked. The plentiful O-containing surface groups can aggravate side reactions between discharge products and carbon. Moreover, 3D rGO (reduced graphene oxide) nanosheets were also applied to investigate its electrochemical activity in Li-O₂ batteries. rGO based batteries deliver a maximum discharge capacity of 4866 mAh g⁻¹, and the discharge capacity is 3200 mAh g⁻¹ at the ninth cycle. The capacity retention ability is still not so high, though rGO based batteries exhibit much higher capacity and capacity retention ability than PCW based batteries. The discharge products of rGO based batteries form a passivation film, which covered on the electrode surface. This passivation film will obstruct the free transportation of electrolyte, oxygen, and electrons during cycling.

In order to enhance the capacity and cycleability, solid cathode catalysts (MnO₂ and Co₃O₄) were applied to improve the catalytic activity. MnO₂@rGO used in this work is synthesized from a simple neutral solution reaction between KMnO₄ and rGO. MnO₂ content in MnO₂@rGO composite is 8.85 wt%. These MnO₂ particles grow uniformly on the rGO surface with the particle size smaller than 20 nm. When the MnO₂@rGO composites were applied as oxygen electrodes for Li-O₂ batteries, it combines the advantages of surface, interface, and nano-size engineering. Based on these advantages, MnO₂@rGO based Li-O₂ battery delivers an initial discharge capacity of 5139 mAh g⁻¹ and a high capacity of 4262 mAh g⁻¹ (80% capacity retention) after 15 cycles at a current density of 100 mA g⁻¹. Moreover, the discharge products of MnO₂@rGO based batteries exhibit small platelet aggregations, which is beneficial for the transportation of electrolyte and oxygen during cycling. The rGO framework possesses a porous multilayer structure, which provides an excellent electrical conductivity, promotes oxygen and ion diffusion, and provides storage space for the discharge products. The nano-sized MnO₂ possesses a high exposed surface,

Abstract

which enhances surface transport of LiO_2 species and avoids the accumulation of discharge products on electrode surface. Furthermore, a transition between lithiated and non-lithiated manganese oxide during discharge and charge process was observed. This transition apparently helps to promote electron transfer between discharge products and the catalyst and thereby to reduce the overpotential of the oxygen evolution reaction.

Co_3O_4 nanoparticles with exposed {112} facets were synthesized by simple hydrothermal and high-temperature calcination method. It was also investigated as cathode catalyst for Li- O_2 batteries. Profiting from the synergistic effect of nano-sized Co_3O_4 and rGO, Li- O_2 cells exhibit a maximum discharge capacity of 3625 mAh g^{-1} with a current density of 250 mA g^{-1} and the capacity is 1933 mAh g^{-1} after 9 cycles. The morphology of discharge products for $\text{Co}_3\text{O}_4/\text{rGO}$ based battery is non-aggregated toroid with the size of 300-400 nm. This structure can provide free pathway for electrolyte, oxygen and electron transportation. Moreover, the battery presents unique cycling stability of 125 cycles with a constant cut-off capacity of $1000 \text{ mAh g}_{\text{rGO}}^{-1}$ (250 mA g^{-1}) and super rate capability when current densities increased from 100 to 1000 mA g^{-1} . Co_3O_4 catalyzes the oxygen reduction reaction and oxygen evolution reaction (ORR/OER) by enhancing the surface transport of LiO_2 species and undergoing lithiated and non-lithiated reaction during discharge and charge process.

Both solid catalysts (MnO_2 and Co_3O_4) share a common way to improve the electrochemical performance: enhancing the mass transport of LiO_2 species and undergoing lithiated and non-lithiated reaction during discharge and charge process to promote the electron transfer from discharge products to catalysts.

In order to overcome the limitation of few catalytically active region (the immobile area next to the interface between the catalysts and the discharge products, solid-solid interface), dual soluble catalysts (LiI and DBBQ, 2,5-di-tert-butyl-1,4-benzoquinone) were applied. The initial discharge capacity of PCW based Li- O_2 battery with dual catalysts is nearly three times enhanced (from 876 to 2592 mAh g^{-1}). Moreover, the capacity retention capability is also dramatically improved by dual soluble catalysts (from 38 to 56 %). These improvements are facilitated by the formation and decomposition of discharge products in solution.

Zusammenfassung

Zusammenfassung

Kohlenstoffmaterialien sind die am häufigsten erforschten Sauerstoffelektrodenmaterialien für Li-O₂ Batterien. In dieser Arbeit synthetisierten wir mikroporösen, wabenartigen Kohlenstoff aus Nebenprodukten durch einfache hydrothermale Behandlung und Hochtemperatur-KOH-Aktivierungsprozess. Der erhaltene poröse Kohlenstoff wurde als Sauerstoffelektrode für Li-O₂ Batterien angewendet. Li-O₂ Batterien mit dem verwendeten porösen Kohlenstoffelektroden, zeigen eine geringe Entladekapazität und eine schlechte Zyklenstabilität. Die maximale Entladekapazität beträgt 1216 mAh g⁻¹ und nach neun Zyklen beträgt diese nur noch 331 mAh g⁻¹. Dies deutet darauf hin, dass der aus Holz gewonnene poröse Kohlenstoff (PCW) eine schlechte elektrochemische Aktivität besitzt. Die schlechte elektrochemische Aktivität ist auf die geringe Porengröße und die reichlich vorhandenen Sauerstoff-haltigen Oberflächengruppen (O, 8,4 at%) zurückzuführen. Die Mikroporen sind für die Ablagerung von Entladungsprodukten zu klein und sind leicht zu blockieren. Die vorhandenen Sauerstoff-haltigen Oberflächengruppen können zu Nebenreaktionen zwischen Entladungsprodukten und Kohlenstoff führen. Darüber hinaus wurden 3D rGO Nanoschichten (reduziertes Graphenoxid) verwendet, um die elektrochemische Aktivität von Li-O₂ Batterien zu untersuchen. Batterien auf rGO-Basis bieten eine maximale Entladekapazität von 4866 mAh g⁻¹ und nach neun Zyklen beträgt diese 3200 mAh g⁻¹. Die Zyklenstabilität ist immer noch nicht so hoch, obwohl rGO-basierte Batterien eine viel höhere Kapazität und Zyklenstabilität aufweisen als PCW-basierte Batterien. Die Entladungsprodukte von rGO Batterien bilden einen Passivierungsfilm, der die Elektrodenoberfläche bedeckt. Dieser Passivierungsfilm behindert den freien Transport von Elektrolyt, Sauerstoff und Elektronen während des Zyklus. Sowohl für PCW- als auch für rGO-Materialien gibt es viele Entladungsprodukte, die während des Entladungsprozesses an die amorphe Phase von Kohlenstoff gebunden werden, was zu weiteren Nebenreaktionen zwischen Kohlenstoff und Entladungsprodukten führen kann.

Um die Kapazität und Zyklierbarkeit zu verbessern, wurden Katalysatoren mit festen Kathoden (MnO₂ und Co₃O₄) eingesetzt, um die katalytische Aktivität zu verbessern. Das in dieser Arbeit verwendete MnO₂@rGO wird aus einer einfachen Neutralisationsreaktion zwischen KMnO₄ und rGO hergestellt. Der MnO₂-Gehalt in MnO₂@rGO-Komposit beträgt 8,85 Gew.-%. Diese kleine Menge von MnO₂-Partikeln wächst gleichmäßig auf der rGO-Oberfläche mit einer Partikelgröße von weniger als 20 nm. Wenn MnO₂@rGO als Sauerstoffelektroden für Li-O₂ Batterien verwendet wird, kann es von den Vorteilen der Oberflächen-, Schnittstellen- und Nanotechnik

Zusammenfassung

profitieren. Basiert auf diesen Vorteilen bietet der Li-O₂-Akku auf MnO₂@rGO-Basis eine anfängliche Entladekapazität von 5139 mAh g⁻¹ und eine hohe Kapazität von 4262 mAh g⁻¹ (80% Zyklenstabilität) nach 15 Zyklen bei einer Stromdichte von 100 mA g⁻¹. Darüber hinaus zeigen die Entladungsprodukte von Batterien auf MnO₂@rGO-Basis kleine Plättchenaggregationen, was für den Transport von Elektrolyt und Sauerstoff während des Zyklus vorteilhaft ist. Das rGO-Gerüst mit mehrschichtiger poröser Struktur bietet eine hervorragende elektrische Leitfähigkeit, fördert die Sauerstoff- und Ionendiffusion und bietet Lagerraum für Entladungsprodukte. MnO₂-Nanopartikelartikel mit reichlich freiliegender Oberfläche können den Oberflächentransport von LiO₂-Spezies verbessern, um die Akkumulation von Entladungsprodukten auf der Elektrodenoberfläche zu vermeiden. MnO₂-Nanopartikel, die gleichmäßig auf der Oberfläche von rGO wachsen, können den direkten Kontakt zwischen rGO und LiOH vermeiden und deren Reaktion verhindern. Darüber hinaus interagiert LiOH an seiner Grenzfläche mit MnO₂, um eine Brückenbildung zwischen dem Entladungsprodukt und dem Katalysator zu bilden. Dies erhöht den Elektronentransfer von LiOH zum Katalysator, was das Überpotential- und die O₂-Desorptionsenergie reduziert.

Co₃O₄ Nanopartikel mit exponierten {112} -Facetten wurden durch Hydrothermal- und Hochtemperatur-Kalziniervorgängen synthetisiert. Es wurde ebenfalls als Kathodenkatalysator für Li-O₂ Batterien untersucht. Li-O₂ Zellen profitieren von dem synergistischen Effekt von Co₃O₄ und rGO in Nanogröße und weisen eine maximale Entladekapazität von 3625 mAh g⁻¹ mit einer Stromdichte von 250 mA g⁻¹ auf. Die Kapazität beträgt nach 9 Zyklen 1933 mAh g⁻¹. Die Morphologie der Entladungsprodukte für Akkus auf Co₃O₄/rGO-Basis ist ein nicht aggregierter Ringkern mit einer Größe von 300 bis 400 nm. Diese Struktur sorgt für einen freien Weg für den Elektrolyt-, Sauerstoff- und Elektronentransport. Darüber hinaus zeigt die Batterie eine einzigartige Zyklenfestigkeit von 125 Zyklen mit einer konstanten Abschaltkapazität von 1000 mAh g_{rGO}⁻¹ (250 mA g⁻¹) und einer Super-Rate-Fähigkeit bei einer Erhöhung der Stromdichte von 100 auf 1000 mA g⁻¹. Co₃O₄ katalysiert die Sauerstoffreduktion und die Sauerstoffentwicklung (ORR/OER), indem der Massentransport von LiO₂-Spezies verbessert wird und eine Brücke für den Elektronentransfer vom Entladungsprodukt zum Katalysator aufgebaut wird.

Beide Festkörperkatalysatoren (MnO₂ und Co₃O₄) verbessern die Elektrochemische Leistung auf gleicher Weise: Verbesserung des Massentransport von LiO₂-Spezies und des Elektronentransfers von Entladungsprodukten auf Katalysatoren durch Bildung einer Brücke.

Zusammenfassung

Um die Begrenzung eines katalytisch aktiven Bereiches (der unbewegliche Bereich neben der Grenzfläche zwischen den Katalysatoren und den Entladungsprodukten, Festkörper / Festkörper-Grenzfläche) zu überwinden, werden zwei lösliche Katalysatoren (LiI und DBBQ, 2,5-Di-tert-butyl-1,4-Benzochinon) verwendet. Die anfängliche Entladekapazität von Li-O₂-Akkus auf PCW-Basis mit zwei Katalysatoren wurde erfolgreich auf das ca. dreifache erhöht (von 876 auf 2592 mAh g⁻¹). Darüber hinaus wird das Kapazitätsretentionsvermögen durch lösliche Katalysatoren deutlich verbessert (von 38 bis 56%). Diese Verbesserungen werden durch die Bildung und Zersetzung von Entladungsprodukten in Lösung gefördert. Die durch die Bildung von Entladungsprodukten in Lösung profitierende Entladungsprodukte, die an der amorphen Phase von PCW-Kohlenstoff gebunden sind, und der Graphitierungsgrad, der beschädigt wird, konnten beide reduziert werden.

1. Introduction

1. Introduction

Nowadays, the development of society and economy is closely related to energy, which consequently leads to a series of directly correlated issues, such as continuous consumption of nonrenewable fossil fuels and the corresponding problem of environmental pollution.[1],[2],[3],[4],[5]

In order to eliminate the risk of energy crisis and fight environmental pollution, a lot of effort has been put into inventing and exploring renewable energy sources, such as solar energy, hydrogen energy, biomass energy, highly efficient chemical power devices, geothermal energy, wind energy, or tidal energy. When it comes to energy storage devices, current research is focusing on the development of electronic equipment with high power and energy density, namely fuel cell,[6] photovoltaic cell,[7] capacitor,[8] Lithium-ion battery,[9] Lithium-sulfur battery,[10] Lithium-air battery,[11] etc. Out of so many kinds of energy storage devices, rechargeable Lithium-oxygen (Li-O₂) batteries have been named “holy grail” and have been attracting quite a lot of interest due to their super high theoretical energy density of 3600 Wh kg⁻¹, which is based on the electrochemical reaction of $2\text{Li} + \text{O}_2 + 2\text{e}^- \rightleftharpoons \text{Li}_2\text{O}_2$, $E^\circ = 2.96 \text{ V vs Li/Li}^+$. [12],[13]

1.1 Working principle of Li-O₂ batteries

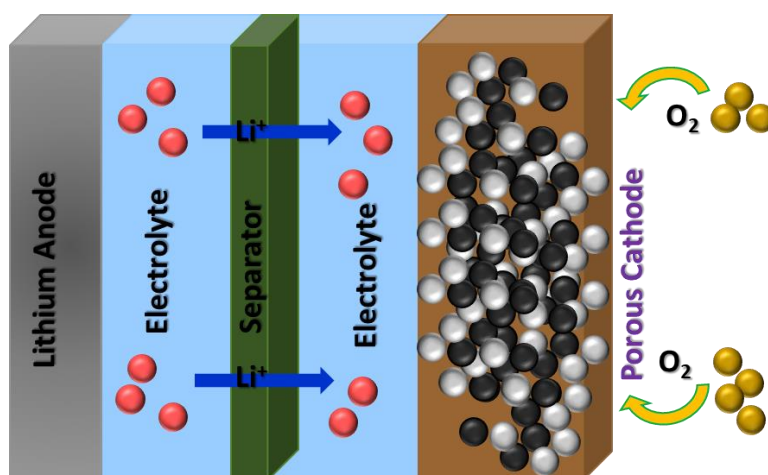


Figure 1.1. Schematic representation of a rechargeable Li-O₂ battery.

Li-O₂ battery is mainly composed of a Li-metal anode, a Li conducting organic electrolyte, a separator and a porous catalytic cathode (Figure 1.1).[14],[15] Among them, electrolytes and catalytic cathodes are widely studied parts of Li-O₂ batteries. The role of porous cathodes is to provide a site for the oxygen reduction reaction and the oxygen evolution reaction. The real

1. Introduction

cathode active material is oxygen, which is not stored in cathodes. The employment of unlimited source of oxygen as the cathode material makes the Li-O₂ battery a promising, widely used power device.

To further understand the working principle of Lithium-oxygen battery, many researchers have devoted themselves to an in-depth exploration of mechanism of O₂ reduction to Li₂O₂ in discharge process. The reduction is generally depicted as a process consisting of the following steps:[16],[17]



As shown in equation (1), O₂ is firstly reduced to superoxide anion (O₂⁻) on cathode surface through a one electron transfer process. Then it will complex with Li cation to form lithium superoxide (LiO₂).[17] The formation of lithium peroxide (Li₂O₂) follows two pathways: One is the reduction of LiO₂ on cathode to form Li₂O₂ (equation (2)); Another possibility is the disproportionation of LiO₂ to form Li₂O₂ and O₂ (equation (3)).[18] The energy density of Li-O₂ battery can reach an outstanding value of 11140 Wh kg⁻¹(excluding O₂ in practical application.[19]

In charge process, the lowest energy reaction pathway for the decomposition of Li₂O₂ is initial delithiation process (equation (4)) and then oxygen evolution step (equation 5).[20] According to the first-principle calculation, oxygen evolution step determines the Li₂O₂ decomposition rate.[20]



Although Li-O₂ batteries can only be used in a laboratory now, their high energy density makes them promising candidates for the next-generation energy storage system that could be employed in the field of military, electro-mobiles as well as outdoor and marine electronic devices. Recently, L. Wang's group developed a flexible Lithium-air battery device, operated in air atmosphere that could be used as a charging device for mobile phones.[21] The research was a preliminary attempt testing the practical application of Li-air batteries.

1. Introduction

1.2 Challenges for Li-O₂ batteries

High energy density makes Li-O₂ battery a promising power device. Nevertheless, many urgent technical problems still need to be efficiently solved before its practical application as next-generation energy storage device occurs. Firstly, Li-O₂ cells are operated in an open environment, in which organic electrolyte evaporates easily. The environment also makes the Lithium metal anode prone to corrosion. Secondly, oxygen electrodes face the challenges of parasitic reactions and electrical passivation during the discharge/charge process.[22],[23]. Electrical passivation is caused by the growth of insoluble and insulating irreversible passivation film during the discharge process.[30],[31] This passivation film leads to poor rate ability and early cell death.[32] Parasitic reactions aggravate the instability of Li-O₂ battery system and lead to the decomposition of oxygen electrode and electrolyte.[16],[33] Besides that, the parasitic products formed at the interface between discharge products and porous cathode tend to further accelerate the electrical passivation.[30] Last but not least, oxygen reduction reaction and oxygen evolution reaction rate are very low in cathode without catalysts. All these factors greatly affect the discharge capacity, cycle life and safety of Li-O₂ batteries.

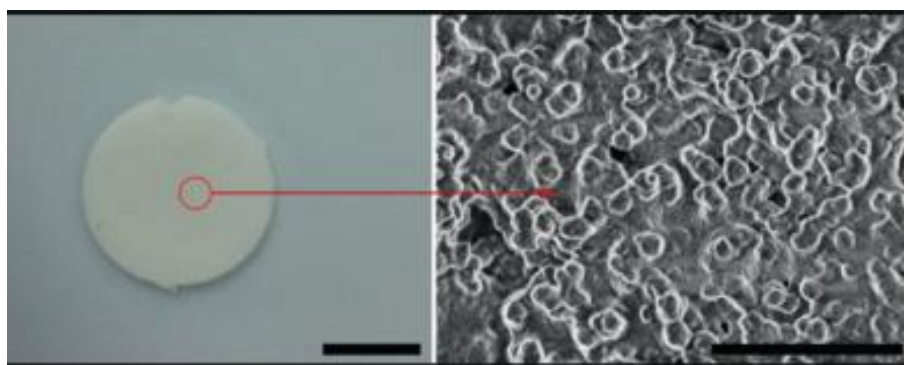


Figure 1.2. Photographic and SEM images of gel polymer electrolyte (GPE).[24]

Concerning the evaporation problem, a lot of effort has been put into the development of an alternative for organic electrolyte. Solid electrolyte, gel electrolyte, and ionic liquid have been put forward as the alternatives. Y. Wang at al. reported the application of polymer electrolyte (Figure 1.2), which dramatically enhanced the cycleability of Li-air batteries (400 cycles).[24] Moreover, ternary imidazolium-pyrrolidinium based ionic liquid (Figure 1.3) was studied as electrolyte for Li-O₂ batteries.[25] In this mixed ionic liquid electrolyte, PYR14TFSI ionic liquid can stabilize the battery system under an oxidative environment and BMIMTFSI can provide good ionic conductivity. Batteries with 4:1 (volume ratio) BMIM⁺:PYR14⁺ ILs mixture maintain a stable

1. Introduction

capacity of 50 cycles.[25]

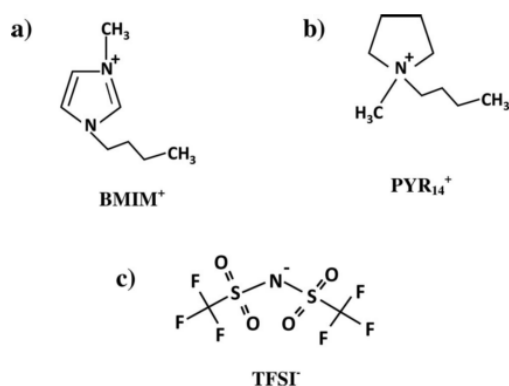


Figure 1.3. Schematic illustration of ions comprising the ILs.[25]

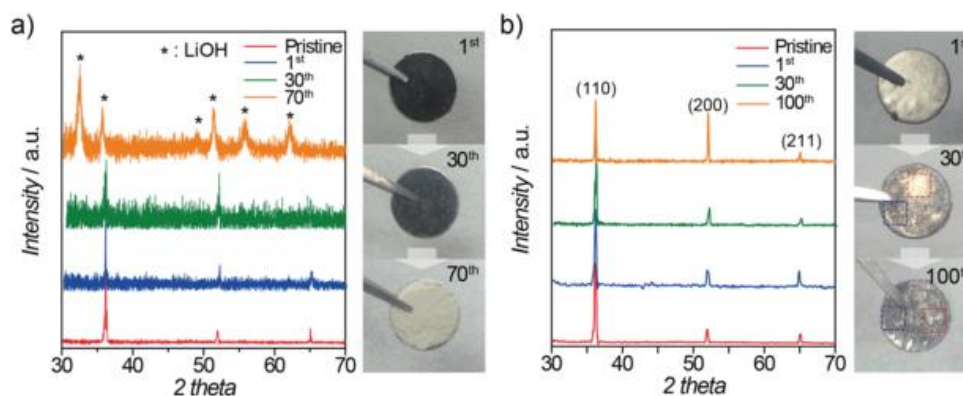


Figure 1.4. XRD spectra and color changes of the Li metals of a) the PE and b) PU cells at different cycle numbers.[26]

Regarding the easy corrosive nature of Li metal, some researchers have applied solid electrolyte as a means of protection. For example, Y. Sun's team designed bi-compartment two solution cells, where the electrodes (anode and cathode) are separated by a solid electrolyte membrane, allowing free transport of Li ions and protecting Li metal anode.[27] Some other researchers have used impermeable separators to prevent water from reaching the Li metal anode. J. Choi's group synthesized moisture and oxygen impermeable separator (PU) and used it in Li-O₂ batteries.[26] Benefiting from the protection of PU, the Li metal exhibited no visible color change or no detectable side reaction products after cycling (Figure 1.4).[26] There are also other methods of protecting Li metal anode, such as application of Li₂CO₃ surface coating (Figure 1.5).[28] Lithium-air batteries with the protection of Li₂CO₃ exhibited a long cycle life of 700 cycles.[28] Apart from taking actions to protect Li metal anode, alternating Li metal to other stable anode also appears to be a good solution. For example, a lithiated Al-carbon composite electrode with a uniform SEI film was applied as anode for Lithium-air battery.[29] The Li-air battery with a

1. Introduction

lithiated Al-carbon anode exhibited higher cycleability than Li-air battery with a Li-anode.

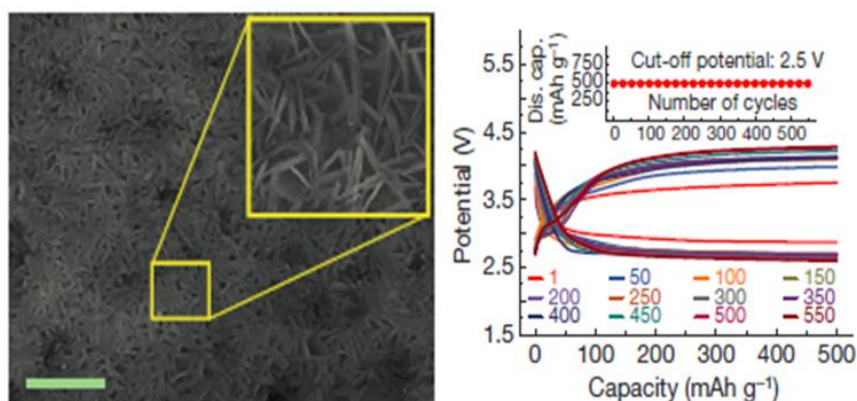


Figure 1.5. The SEM image of the protected anode and performance of anode based lithium-air battery system.[29]

It has been reported by P. Bruce’s group that the passivation film is primarily formed by the growth of discharge products on the sticky oxygen electrode surface and that the discharge products on electrode surface can easily react with oxygen electrode.[30] The research proved that the growth of discharge products in solution is an effective method to avoid the formation of passivation film, and therefore, reducing the risk of side reactions. Moreover, the formation of discharge products in solution can also promote the rate capability and enhance the discharge capacity of Li-O₂ battery.[31] The group also found that the O₂ reduction in an aprotic solvent containing Li⁺ follows the surface pathway growth when $\Delta G^\circ \gg 0$ (low DN) and the solution pathway formation when $\Delta G^\circ \ll 0$ (high DN) (Figure 1.6).[31] Moreover, the O₂ is reduced in solution in high DN and high potential.

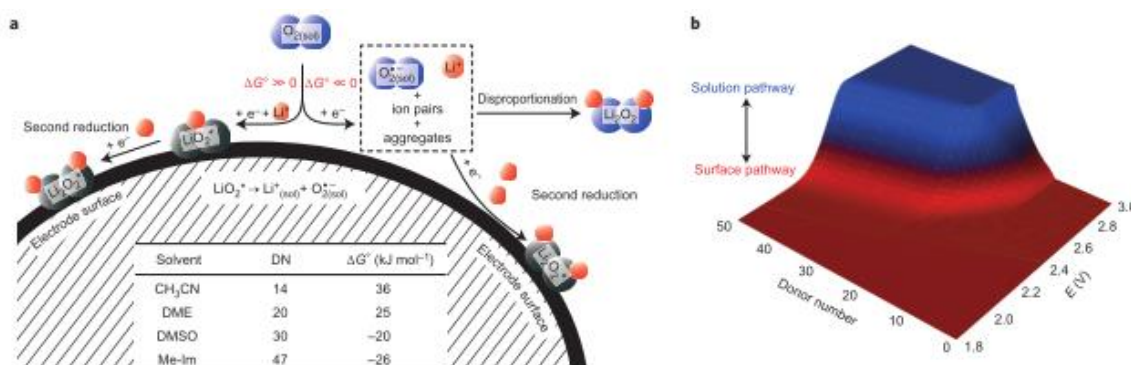


Figure 1.6. Schematic of the O₂ reduction mechanism and plot showing how it is affected by DN and potential.[31]

Applying redox mediators is an adaptable method of accelerating oxygen reduction and oxygen evolution reaction. H. Lim et al. reported a novel Li-O₂ battery with high reversibility and good rate ability using a soluble catalyst (LiI) combined with a hierarchical nanoporous oxygen

1. Introduction

electrode (Figure 1.7).[32] When current rate was gradually raised from 200 to 6000 mA g⁻¹, the polarization degree did not increase drastically.[32] C. Grey's group used a reduced graphene oxide electrode and a redox mediator (LiI) to reversibly form and remove crystalline LiOH with particle sizes larger than 15 μm.[33] When cycled at 1 A g⁻¹, the voltage gap was only ~0.2 V. Even at higher rates of 8 A g⁻¹, the voltage gap remained very small (0.7 V).[33] When the cut-off capacity was limited to 1000, 5000, and 8000 mAh g⁻¹, the cells showed a little increase in voltage polarization during cycling (Figure 1.8).[33]

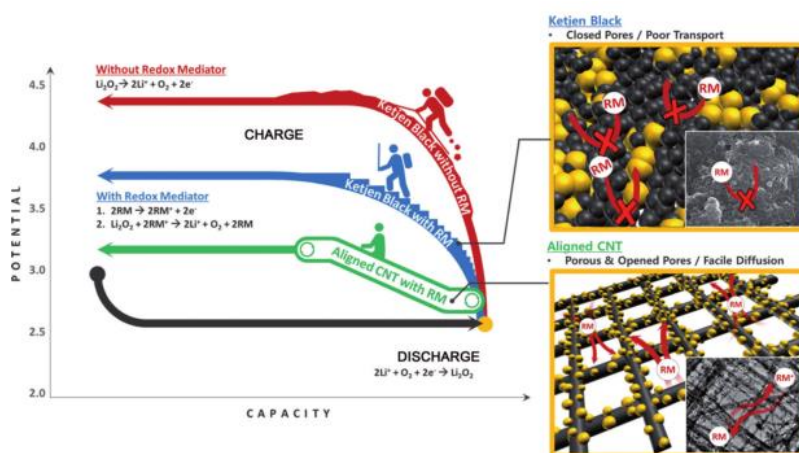


Figure 1.7. Schematic illustration of the role of the redox mediator (RM) in a Li-O₂ battery system.[32]

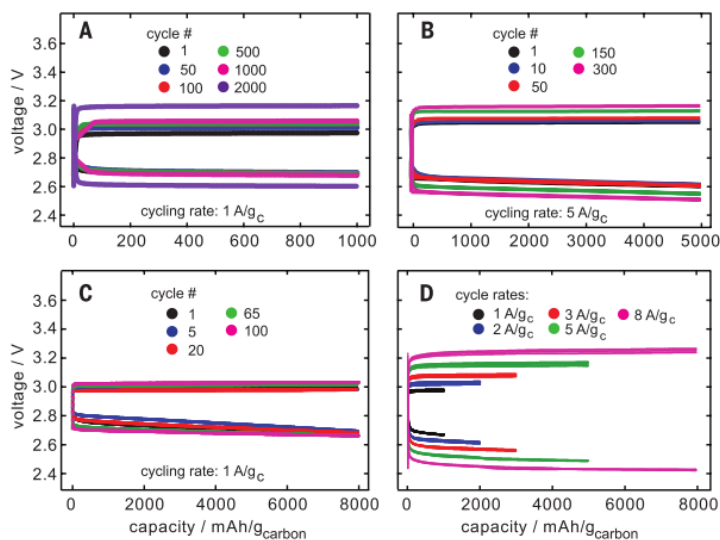


Figure 1.8. Electrochemical performance of the Li-O₂ battery with a reduced graphene oxide electrode and a redox mediator (LiI).[33]

Some metal or metal oxides can serve as cathode catalysts for Li-O₂ batteries to enhance electrochemical activity. H. Zhou's group applied core-shell-structured CNT@RuO₂ composite as cathode for Li-O₂ batteries.[34] Batteries with CNT@RuO₂ showed a high round-trip efficiency

1. Introduction

(79%), a low voltage gap (0.72 V) and excellent rate performance (Figure 1.9).[34] J. Chen's group synthesized MnO₂/HPC hybrids (MnO₂ nanostructures on hierarchically porous carbon) and investigated them as oxygen electrodes for Li-O₂ batteries (Figure 1.10).[30]. MnO₂/HPC hybrids exhibited superior ORR and OER catalytic activity as cathode materials for Li-O₂ battery. Batteries catalyzed by MnO₂ exhibited an enhanced cycle number of 300 cycles.[30] Even the MnO₂/HPC based battery was operated at high current density of 5,000 mA g⁻¹, it could still deliver a discharge capacity of 2,260 mAh g⁻¹. [30]

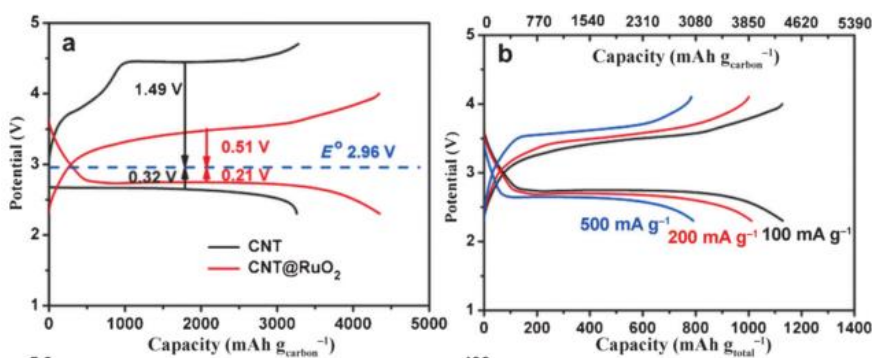


Figure 1.9. Discharge/charge profiles of the Li-O₂ batteries with the pristine CNTs and CNT@RuO₂ composite (a) and the first discharge/charge profiles of CNT@RuO₂ at a current of 100, 200, and 500 mA g⁻¹. [34]

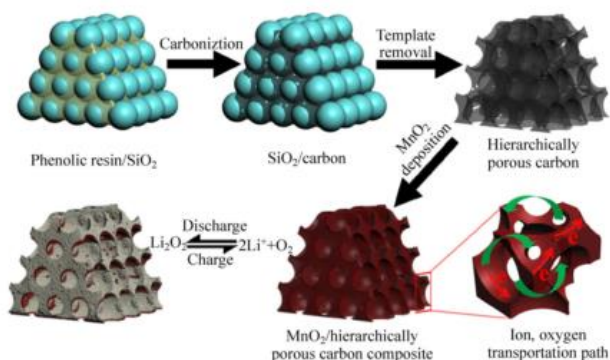


Figure 1.10. Schematic illustration of the synthesis of MnO₂/HPC nanocomposite and its application in a Li-O₂ battery. [30]

1.3 The progress of oxygen electrodes for Li-O₂ batteries

Porous oxygen electrodes play a variety of roles in the Li-O₂ battery system: (i) they act as an active catalyst materials for oxygen reduction/oxygen evolution reaction (ORR/OER).[33] (ii) they serve as a conductive framework for electron transfer.[35] (iii) they provide a matrix to deposit discharge products.[36],[37] (iv) they have a porous network that supports the diffusion of oxygen.[38],[1] [33] It is therefore important to develop suitable oxygen electrode materials to

1. Introduction

improve the electrochemical performance of Li-O₂ batteries. Intensive research efforts have been devoted to the design and synthesis of appropriate oxygen electrode materials in recent years. The oxygen electrode materials that have been tested include both carbon and no-carbon materials.

1.3.1 Carbon oxygen electrodes

Carbon materials, including commercial carbon,[32] porous carbon,[32] carbon fiber,[39] carbon tube,[34] graphene[14], are the most widely used oxygen electrode materials for Li-O₂ batteries. Their morphology, pore size, surface area, and surface defects greatly influence the electrochemical performance of carbon based Li-O₂ batteries.[37],[40],[15]

The electrochemical activity of commercial carbon as oxygen electrodes for Li-O₂ batteries has been studied by many research groups. J. Chen's group has tested the electrochemical performance of Super P based Li-O₂ batteries. Super P based Li-O₂ batteries can cycle only 34 times at a current density of 350 mA g⁻¹ (Figure 1.11), which can be ascribed to their small pore volume and poor catalytic activity.

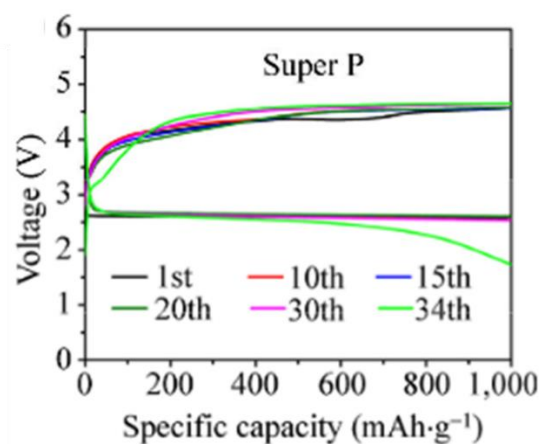


Figure 1.11. Discharge-charge curves of the Li-O₂ batteries with Super P as cathode.[30]

Porous carbon materials can also serve as oxygen diffusion medium and provide electrochemical reaction active sites for reversible ORR/OER due to their controllable morphology, pore size distribution, and surface area. Most porous carbon materials used in Li-O₂ batteries are prepared from template methods. L. Zhao et al. used colloidal silica particles as the template to synthesize meso/macro-porous carbon materials of different pore size (20-100 nm) (Figure 1.12).[37] This research primarily focused on the exploration of the optimal pore size that would enhance discharge capacity. They found that discharge capacity increased when the pore size was enlarged, reaching the maximum value of 7169 mAh g⁻¹ when the pore size was 80 nm.[37] Recently, Y.

1. Introduction

Xia's team reported the application of ordered hierarchical mesoporous/macroporous carbon (MMCSAs) as oxygen electrodes for Li-O₂ batteries. MMCSAs was synthesized by macroporous silicon skeleton template. Benefiting from their hierarchical mesoporous/macroporous structure, Li-O₂ batteries with MMCSAs exhibited high rate ability when current densities increased from 50 to 1000 mA g⁻¹ (Figure 1.13).[1]

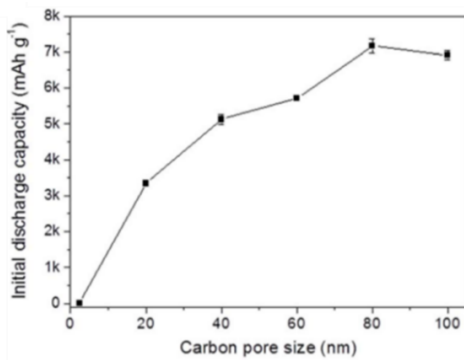


Figure 1.12. The correlation between carbon pore size and cell capacity.[37]

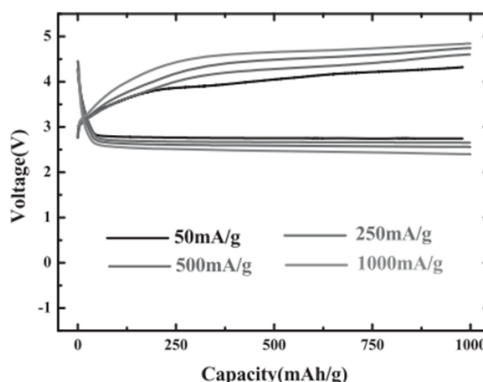


Figure 1.13. Discharge/charge curves of a Li-O₂ battery with different applied current densities.[1]

Carbon nanofibers (CNF) with good conductivity, high surface area, compact structure, and few defects have been widely applied to improve the electrochemical activity of oxygen electrodes in recent years. The morphology of carbon nanofibers greatly impacts their electrochemical activity. L. Ming's group synthesized vertically aligned coral-like carbon nanofibers (VA-NCCF) and applied them as oxygen electrode materials for Li-O₂ batteries (Figure 1.14).[41] Li-O₂ batteries with VA-NCCF can get a very high energy efficiency (90%) and a small voltage gap (0.3 V).[41] This excellent performance can be ascribed to the unique vertically aligned and coral-like N-doped carbon microstructure, which provides suitable pathways for the transportation of electrolyte, oxygen and electron.[41]

1. Introduction

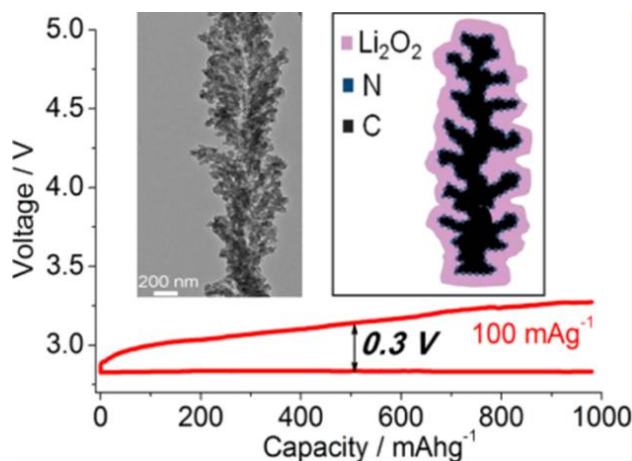


Figure 1.14. The morphology and discharge/charge voltage profile of the VA-NCCF.[41]

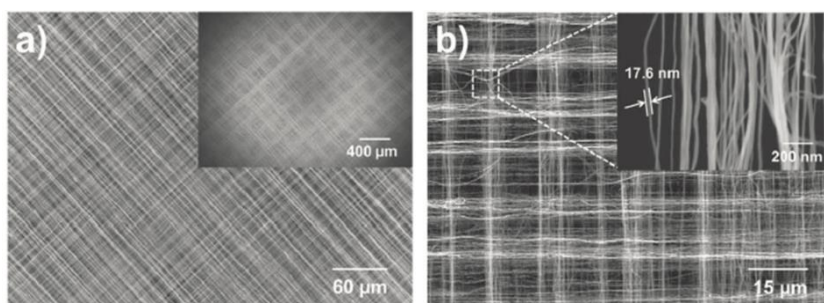


Figure 1.15. SEM images of the CNT fibril at low and high magnification.[42]

Many research groups are also working with carbon nanotubes (CNT), which can provide abundant diffusion channels for oxygen to reach the inner side of oxygen electrodes. Hierarchical fibril CNT with controlled porosity was prepared and used as oxygen electrodes for Li-O₂ batteries by K. Kang's group (Figure 1.15). Hierarchical fibril CNT with controlled porosity can efficiently prevent the formed discharge products from blocking the pores of oxygen electrodes. Due to the facile porous structure of hierarchical fibril CNT, batteries with hierarchical fibril CNT showed outstanding cycleability even in high current density.

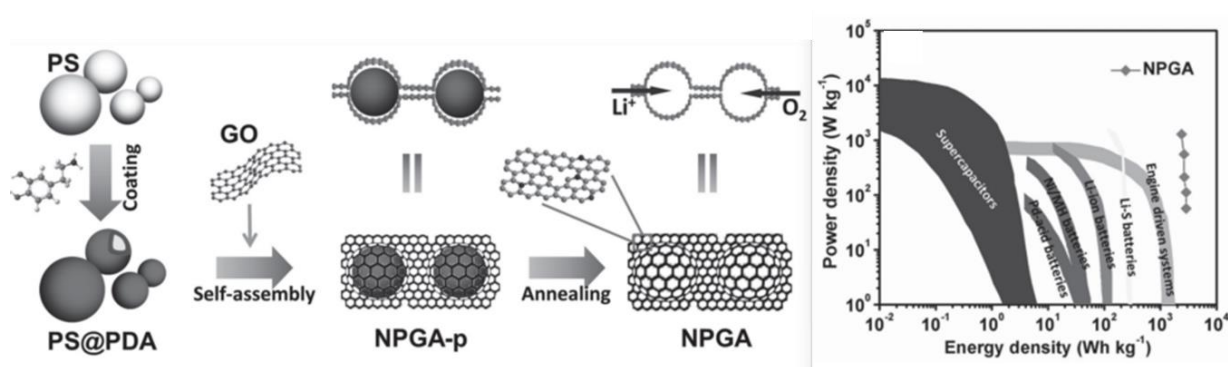


Figure 1.16. Schematic process for synthesis of NPGA and Ragone plot of the Li-O₂ batteries with NPGA.[15]

1. Introduction

Graphene materials stand out when compared with other carbon materials due to their stable mechanical properties, high surface area, and good electric conductivity. Moreover, surface functional groups have a great influence on their electrochemical activity. 3D porous N-doped graphene aerogels (NPGAs) were synthesized through polymerization and hydrothermal process by J. Qiu's group (Figure 1.16).[15] NPGAs are composed of interconnected nanocages. Compared to other battery systems, NPGAs based Li-O₂ batteries exhibit superior energy density. The high energy density of Li-O₂ batteries with NPGAs can be attributed to their high pore volume, well-developed interconnected channels, and crumpled graphene sheets.[15] J. Zhang's team reported the use of hierarchically porous graphene, which was synthesized using a colloidal micro-emulsion method (Figure 1.17).[43] In this hierarchically porous structure, nanopores provide abundant catalytic active sites for ORR/OER reactions and micropores offer suitable channels for rapid electrolyte and oxygen transportation.

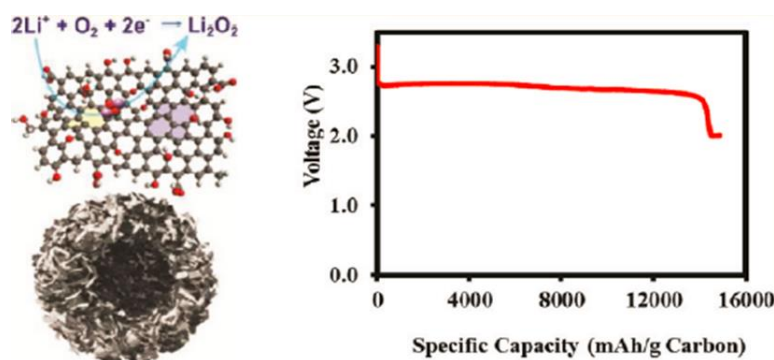


Figure 1.17. Schematic structure of a functionalized graphene sheet and the discharge curves of Li-O₂ battery with functionalized graphene sheet.[43]

1.3.2 Non-carbon oxygen electrodes

Because of the instability of carbon materials, which tend to decompose when exposed to voltage higher than 3.5 V, the use of non-carbon materials as oxygen electrodes for Li-O₂ batteries is being tested.[23] Non-carbon oxygen electrode materials include mainly the following types: precious metal,[4] metal compound (metal oxides and metal nitrides),[44],[35] metal organic compounds, and polymer.[45]

Li-O₂ batteries with porous precious metals as oxygen electrodes present excellent electrochemical performance, which is ascribed to their high physical and chemical stability, conductivity, and catalytic activity.[46] H. Zhou et al. successfully synthesized nanoporous Ru, which can serve as a binder and carbon-free oxygen electrodes for Li-O₂ batteries (Figure 1.18).[4]

1. Introduction

Binder and carbon-free Ru electrodes can forbid the parasitic reactions originated from carbon and binder. These parasitic reactions are often responsible for early cell death of Li-O₂ batteries. Porous Ru based Li-O₂ batteries exhibit a long cycle life of 100 cycles with a cut-off capacity of 1000 mAh g⁻¹ in a narrow voltage window between 2.75-3.75 V.[4] Besides that, the group also reported the application of Ru/ITO composite (Ru nanoparticles deposited on conductivity indium tin oxide) as oxygen electrodes for Li-O₂ batteries.[47] Except for Ru, Pt and Au are also believed to expose high ORR and OER catalytic activity for Li-O₂ batteries (Figure 1.19).[48]. Regardless of their advantages, high price limits their application.

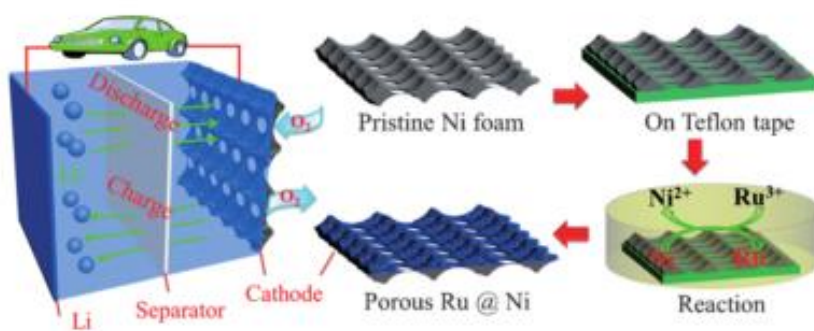


Figure 1.18. Synthesis process of porous Ru@Ni cathode and their application in Li-O₂ batteries.[4]

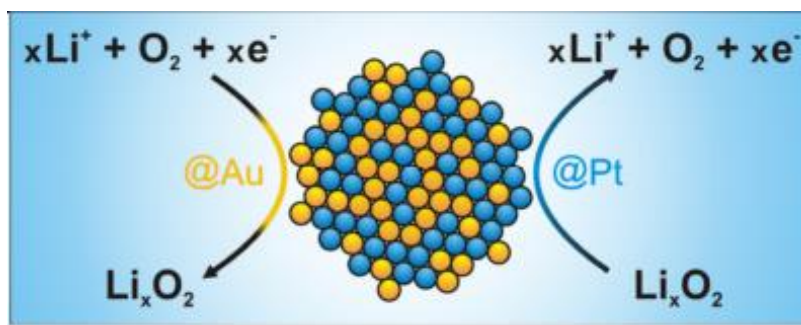


Figure 1.19. The kinetics of ORR and OER in Li-O₂ batteries enhanced by Pt and Au particles.[48]

Metal oxides/nitrides also present good catalytic activity in ORR/OER process, which makes them promising oxygen electrode materials for Li-O₂ batteries.[49] They are also much cheaper than precious metals. K. Sun's team synthesized self-standing Ni@Co₃O₄ web-like nanofiber arrays (Ni@Co-WNFs) through a simple hydrothermal process (Figure 1.20).[50] In the synthesis process, macroporous Ni foam serves as the skeleton to deposit Co₃O₄. The macroporous structure of Ni foam can promote the formation of micro/macroporous Ni@Co₃O₄ with unique web structure.[50] Ni@Co₃O₄ with micro/macropores can be used as a binder and carbon-free oxygen electrode for Li-O₂ batteries. Li-O₂ batteries based on Ni@Co₃O₄ electrode exhibit a high

1. Introduction

discharge capacity of 17118 mAh g⁻¹ at a current density of 0.1 mA cm⁻¹. [50]

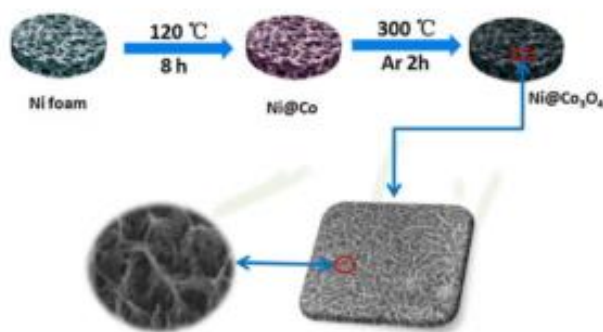


Figure 1.20. The synthesis process and microstructure of Ni@Co₃O₄. [50]

X. Zhang et al. synthesized 3D ordered macroporous LaFeO₃ (Figure 1.21) through a template method and applied it as oxygen electrodes for Li-O₂ batteries. [36] Macroporous LaFeO₃ with open and interconnected structure can provide abundant electrochemistry active sites for ORR and OER. Moreover, the 3D ordered macroporous structure can provide facile Li⁺ and oxygen diffusion pathways. When compared with LaFeO₃ nanoplates, the cycling stability of 3D ordered macroporous LaFeO₃ based Li-O₂ batteries improves dramatically and the voltage gap is reduced.

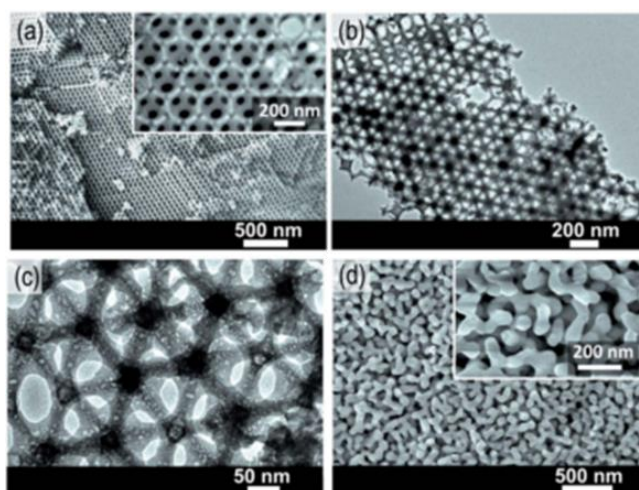


Figure 1.21. The FESEM and TEM images of 3DOM-LFO. [36]

Metal-organic frameworks (MOFs) have many advantages when they are applied as oxygen electrodes for Li-O₂ batteries. [51] Firstly, they possess abundant ordered micropores, which are suitable for oxygen diffusion. Secondly, the metallic active sites along the microporous channels can combine with oxygen, which can catalyze the ORR/OER in molecular level. Thirdly, their high surface area and high oxygen adsorption capacity can provide more reactive substance

1. Introduction

(oxygen) during discharge process. Last but not least, they also possess abundant mesopores, which can promote the electrolyte transportation and provide space for the depositing of discharge products. Q. Li's group reported the application of Mn-MOF-74 as oxygen electrodes for Li-O₂ batteries. The surface area of Mn-MOF-74 is 1316 m² g⁻¹ and the O₂ absorption amount is 15.0 mg g⁻¹. Batteries with Mn-MOF-74 exhibit a high capacity of 9420 mAh g⁻¹ (Figure 1.22).[45] This value is four times higher than super P based Li-O₂ batteries. Moreover, another MOFs (Ni-MOFs with a 3D micro/nano-structure) have also been explored as oxygen electrodes for Li-O₂ batteries.[51] Because of their hexagonal plate shape with C, O, Ni, and N elements uniformly distributed (Figure 1.23),[51] batteries with Ni-MOFs exhibit a high round-trip efficiency of 80% and an excellent stability of 170 cycles without a noticeable increase of voltage gap.[51]

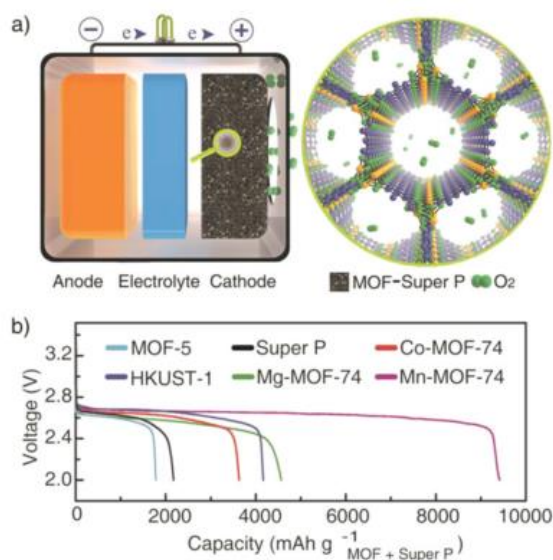


Figure 1.22. Schematic of Li-O₂ batteries with MOF-Super P composite as the cathode and discharge profiles of the Li-O₂ cells based on MOF-Super P.[45]

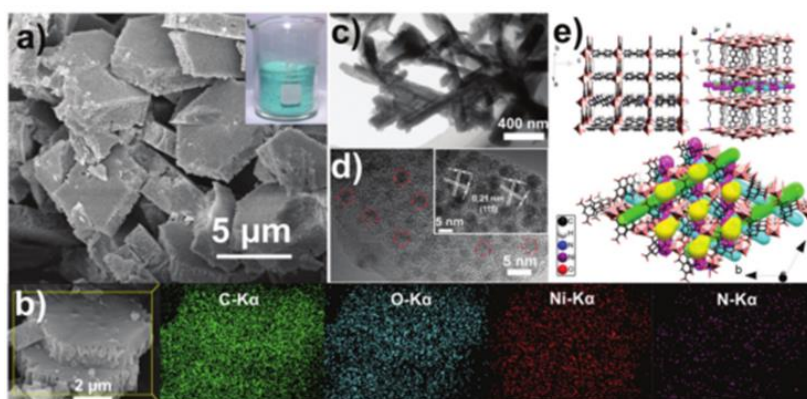


Figure 1.23. The morphology and structure of Ni-MOFs.[51]

1. Introduction

Conductive polymer with porous structure can also serve as oxygen electrodes for Li-O₂ batteries. Amanchukwu et al. reported that electron-conducting polymer poly(3,4-ethylenedioxythiophene) (PEDOT) can support oxygen reduction to form Li₂O₂ in a non-aqueous environment.[52] They found that the formation of sulfone functionalities on the PEDOT surface and cleavage of the polymer repeat unit with cycling can reduce electron conductivity, and eventually lead to poor cycling (Figure 1.24).[52] Y. Cui's group designed a high reversible oxygen electrode with hydrophilic nano-PPy tubes (TPPy) (Figure 1.25).[53] High hydrophilicity of the TPPy keeps hollow pores of the nanotubes open, which affords sufficient paths for O₂ diffusion.[53] This promotes equal distribution of oxygen and equal deposition of discharge products. Moreover, proper wetness of TPPy surface enables the formation of an organic electrolyte layer of proper thickness, which promotes the cathodic reaction.[53] Compared to PPy with granular morphology (GPPy) and commercial carbon, TPPy exhibit much higher rate ability.

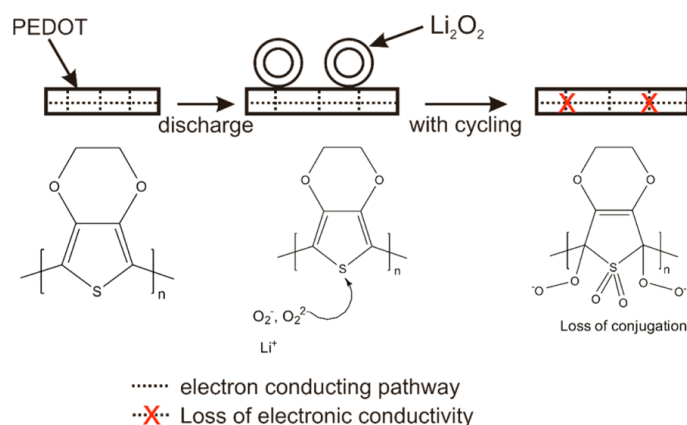


Figure 1.24. Degradation mechanism of Li-O₂ batteries with PEDOT as oxygen electrodes.[52]

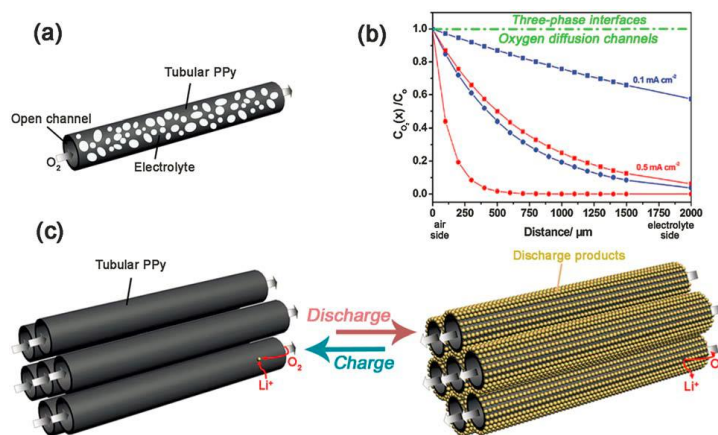


Figure 1.25. Schematic representations of the organic electrolyte and oxygen distributions on hydrophilic PPy nanotubes, and the schematic discharge-charge process.[53]

1. Introduction

1.4 The effects of catalysts on the electrochemical performance of Li-O₂ batteries

As mentioned above, carbon materials are the most widely used oxygen electrodes for Li-O₂ batteries. However, because the catalytic activity of pure carbon is not ideal, it cannot efficiently catalyze the reversible formation/decomposition of discharge products. Moreover, carbon surface is sticky, which aggravates the formation of passivation film on electrode surface. The insoluble and wide-bandgap insulated discharge products (passivation film) tend to gradually block the oxygen and electrolyte diffusion pathways, inhibiting the charge transfer.[30],[32] This leads to early cell death,[54] high charging overpotential,[55] low rate capability[16],[56] as well as poor cycling stability[57],[58] of Li-O₂ batteries. What is worse, the high decomposition voltage of Li₂O₂ with pure carbon electrode induces the decomposition of electrolyte and carbon electrode. To obtain high discharge capacity, redox mediators (RMs) are employed by many research groups as homogeneous catalysts to promote the discharge performance.[26],[59] Moreover, oxidation mediators, which can transfer the electron between the electrode surface and discharge products, are also explored as catalysts to facilitate the charging process. Based on the solubility in electrolyte, catalysts are divided into solid catalysts and soluble catalysts.

1.4.1 Solid catalysts

Noble metals (Ag,[23] Pt[60] and Ru[4] et al.), metal oxides (MnO₂,[61] Co₃O₄[62] and Fe₂O₃[63] et al.), and perovskites (CaMnO₃,[44] LaNiO₃[2] and LaFeO₃[36] et al.) are the widely studied solid catalysts. These catalysts can improve the kinetics of the discharge reaction by tuning the adsorption energy of O₂ and LiO_x intermediates on them.[64] Typically, solid catalysts are mixed with carbon frameworks to lower the cost and enhance the conductivity, which combines the advantages of both catalysts and carbon materials. Many carbon frameworks loaded with noble metals, metal oxides or perovskites present superior electrochemical performance as the air electrodes for Li-O₂ cells.[44]

Noble metals employed as catalysts for Li-O₂ batteries can effectively reduce the discharge/charge overpotential. S. Zhou's group reported the synthesis of Ru-doped multi-walled carbon nanotube paper (Ru@MWCNTP) through a wet chemical method (Figure 1.26).[65] Li-O₂ batteries with Ru nanoparticles as catalysts can reduce 0.68 V of the charge voltage and increase 0.07 V of the discharge voltage.[65] This means Ru@MWCNTP possesses both ORR and OER catalytic activity. Moreover, batteries catalyzed by Ru nanoparticles show repeatable discharge/charge profiles of 20 cycles with a cut-off capacity of 5000 mAh g⁻¹. [65] Without Ru catalyst, pure

1. Introduction

MWCNTP based batteries exhibit very fast capacity decay. The improved performance of Ru@MWCNTP based Li-O₂ batteries can be attributed to good conductivity and facile oxygen pathway provided by carbon nanotube and high catalytic activity originated from Ru nanoparticles.[65]

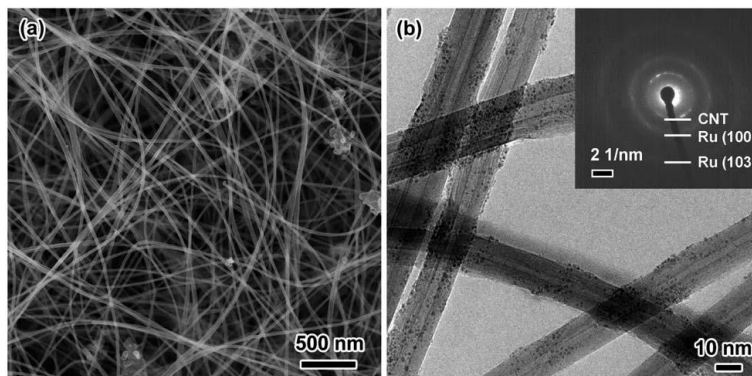


Figure 1.26. The SEM image of MWCNTP and high resolution TEM of Ru@MWCNTP.[65]

J. Liu et al. found that crystalline LiO₂ can be stabilized in a Li-O₂ battery by using a suitable graphene and iridium (Ir) nanoparticles as cathode.[3] It has been discovered that LiO₂ has lower decomposition voltage than Li₂O₂. As a result, Ir-rGO based battery shows a very low charge potential of ~3.2 V and its rise to 3.5 V after 40 cycles.[3] In comparison, rGO based battery shows a much higher charge potential of ~4.2 V.[3]

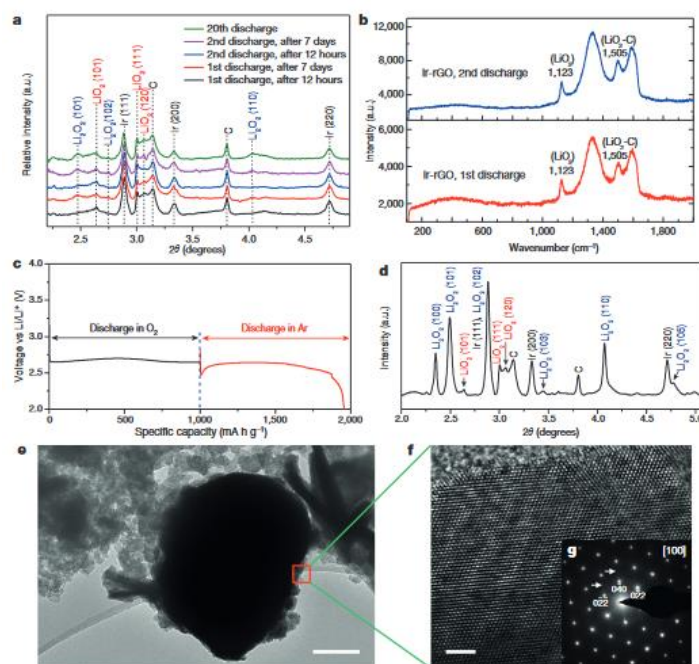


Figure 1.27. XRD, Raman and TEM characterization of the discharge products of the Ir-rGO based Li-O₂ batteries.[3]

1. Introduction

K. Amine's team reported Li-O₂ batteries catalyzed by Pt/M-NT (Pt/ α -MnO₂ nanotube) exhibit high catalytic activity with very low charge potential.[66] In the research, Pt/M-NT was synthesized from the atomic layer deposition (ALD) method and nanostructured palladium was applied on porous carbon with the controlled size of 2-8 nm (Figure 1.28).[67] Apart from the above listed noble metals, Au and Pd are also explored by many research groups as oxygen electrode catalysts for Li-O₂ batteries. They also present unique electrochemical performance.[68]

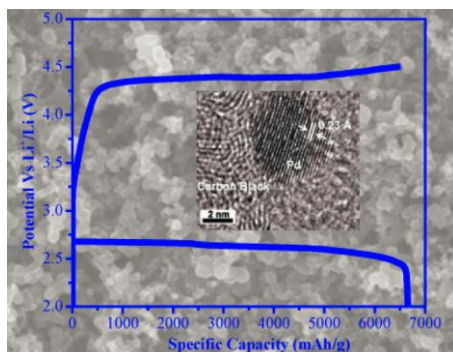


Figure 1.28. The morphology and discharge-charge profiles of porous carbon supported palladium nanoparticles.[66]

Metal compounds (such as Co₃O₄, RuO₂, MnO₂, TiO₂, MoN and TiN et al.) are also widely studied by researchers as catalysts for Li-O₂ batteries. They can enhance mass transport of LiO₂ species, which can prevent the formation of passivation film on oxygen electrode surface. D. Kim's group synthesized porous carbonized-Co₃O₄ with inverse opal nanostructures (C-Co₃O₄ IO) through a complementary colloid process and a block copolymer self-assembly process (Figure 1.29).[62] Compared to Li-O₂ batteries with pure KB, the discharge capacity of batteries catalyzed by C-Co₃O₄ was doubled.[62]

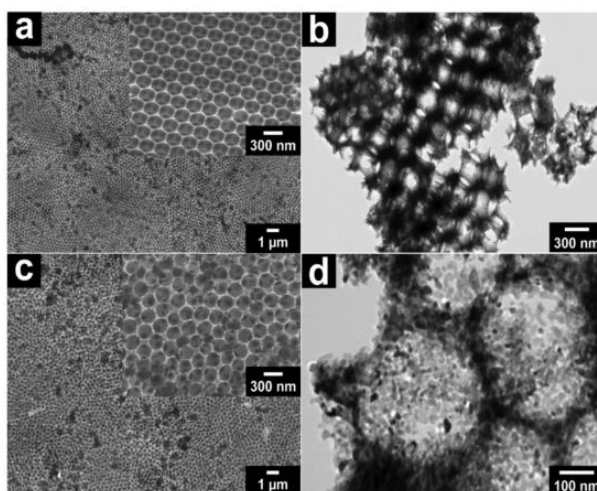


Figure 1.29. FE-SEM and TEM images of Co₃O₄ IO.[62]

1. Introduction

$\text{Mn}_3\text{O}_4/\text{RGO}$ composite, which Mn_3O_4 nanoparticles are uniformly dispersed on rGO surface, was synthesized from a solution method (Figure 1.30).[69] $\text{Li}-\text{O}_2$ batteries catalyzed by $\text{Mn}_3\text{O}_4/\text{RGO}$ exhibited an excellent initial discharge capacity of $16000 \text{ mAh g}_{\text{RGO}}^{-1}$, which is much higher than the capacity of pure rGO based batteries ($7000 \text{ mAh g}_{\text{RGO}}^{-1}$).[69]

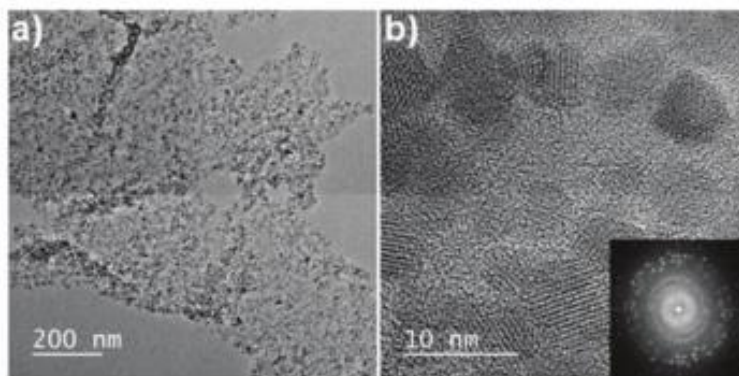


Figure 1.30. The (HR)TEM images of the as-prepared $\text{Mn}_3\text{O}_4/\text{rGO}$ nanocomposites.[69]

Except for metal oxides, some metal nitrides can also serve as catalysts for $\text{Li}-\text{O}_2$ batteries. H. Zhou's group successfully synthesized TiN nanoparticles supported on Vulcan XC-72 (n-TiN/VC) and used them as oxygen electrodes for $\text{Li}-\text{O}_2$ batteries.[70] Compared to VC based $\text{Li}-\text{O}_2$ batteries, the discharge capacity of batteries with n-TiN doubled and the overpotential was also greatly reduced (Figure 1.31).[70]

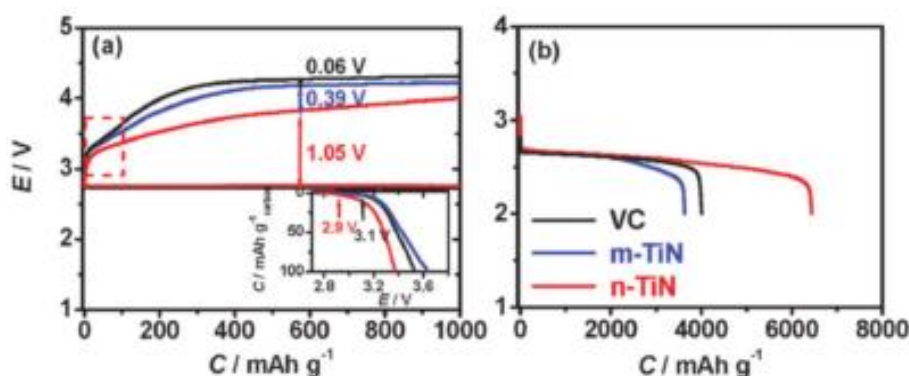


Figure 1.31. Discharge/recharge curves of VC, m-TiN/VC, and n-TiN/VC as cathode catalysts of $\text{Li}-\text{O}_2$ batteries.[70]

Many heteroatoms (N, S and B) doped carbons also show good catalytic activity for $\text{Li}-\text{O}_2$ batteries. For example, L. Dai's group synthesized nitrogen-doped holey graphene (N-HGr) as cathode catalyst for $\text{Li}-\text{O}_2$ batteries (Figure 1.32).[14] Batteries catalyzed by N-HGr show a good coulombic efficiency of 85% and a high discharge capacity of 17000 mAh g^{-1} . [14] This can be ascribed to the synergistic effect of graphene framework and N originated active sites.[14] Our

1. Introduction

group also carried out some tests regarding heteroatom doped carbon as cathode catalyst for Li-O₂ batteries. We found that B doped porous carbon exhibited good catalytic activity for Li-O₂ batteries.[71]

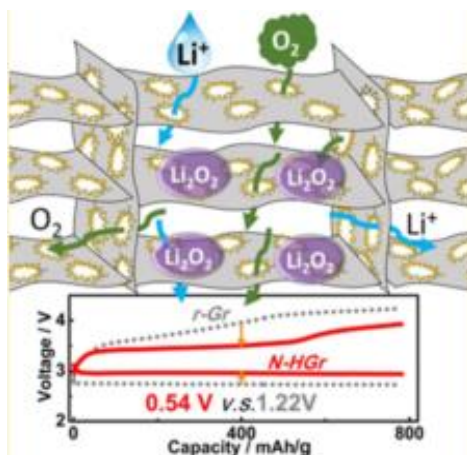


Figure 1.32. Schematic of N-HGr as air electrode and discharge-charge profiles of rGO and N-HGr.[14]

Some perovskites show high electrocatalytic activity when they are applied as cathode catalysts for Li-O₂ batteries. J. Zhang' team applied porous LaNiO₃ nanocubes as cathode catalyst for Li-O₂ batteries.[2] Batteries catalyzed by LaNiO₃ exhibited enhanced capacity (3407 mAh g⁻¹) and good cycle stability (23 cycles).[2] This can be ascribed to the synergistic effect of porous structure, large specific surface area and high electrocatalytic activity of porous LaNiO₃ nanocubes.[2] J. Xu' group synthesized three-dimensional ordered macroporous LaFeO₃ (3DOM-LFO) and employed it as electro-catalyst in Li-O₂ batteries (Figure 1.33).[36] Batteries with 3DOM-LFO show low voltage gap (~1.4 V), high specific capacity (~15000 mAh g⁻¹), good rate capability (from 0.025 to 0.2 mA cm⁻²) and excellent cycle stability (124 cycles).[36]

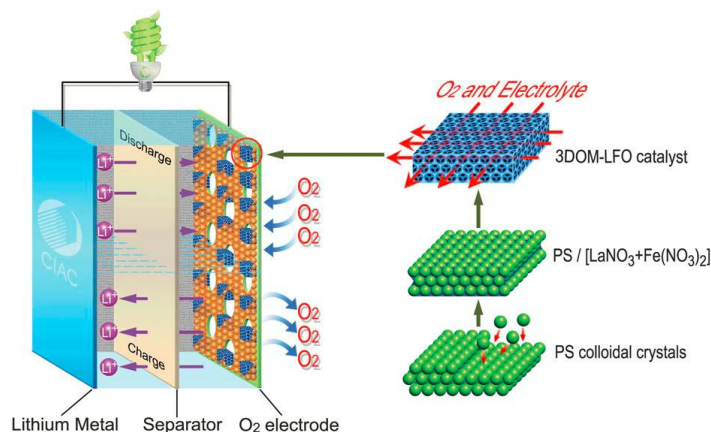


Figure 1.33. Schematic illustration for preparation of 3DOM-LFO catalyst and structure of the rechargeable Li-O₂ batteries.[36]

1. Introduction

1.4.2 Soluble catalysts

Although the solid type catalysts positively affect the electrochemical performance of Li-O₂ batteries, the catalytically active region is limited to the immobile area next to the interface between the catalysts and the discharge products (solid-solid interface).[32] Numerous research groups have devoted themselves to developing efficient soluble catalysts for high performance Li-O₂ batteries, such as EV (ethyl viologen, ORR), CoQ10 (Coenzyme Q10, ORR), DBBQ (ORR), H₂O (ORR), LiI (OER), TTF (tetrathiafulvalene, OER), DMPZ (dimethylphenazine, OER) and TEMPO (tetramethylpiperidinyloxy, OER).[26],[16],[72]

Some soluble catalysts can improve the electrochemical performance of Li-O₂ battery by influencing the discharge process. Soluble catalysts or salts with high donor effectively enhance the discharge capacity and reduce the discharge overpotential, which can be ascribed to the solution phase growth of discharge products in discharge process.[73],[16] This means the formation of discharge products is no longer limited to the surface growth, which can result in the formation of passivation films.

Owen' team added ethyl viologen (EV) to electrolyte to improve the ORR process.[74] They demonstrated that EV efficiently promoted Li₂O₂ formation and increased the discharge capacity. EV²⁺ was reduced at the electrode and then reacted with O₂ to form LiO₂ to regenerate itself (EV²⁺+e⁻ → EV⁺, EV⁺+O₂+2Li⁺ → EV²⁺+LiO₂).[74] EV worked as a shuttle to transport electrons between O₂ and LiO₂. LiO₂ was further reduced by another reduced EV molecule to the final product Li₂O₂ (EV⁺+LiO₂+Li⁺ → EtV²⁺+Li₂O₂).[74] DBBQ and CoQ10 promote the discharge performance by forming new complex intermediates to replace LiO₂.

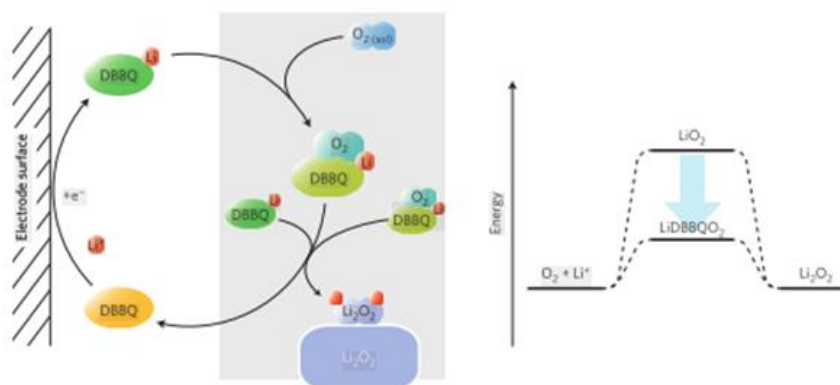


Figure 1.34. Schematics of reactions on discharge (left) and the effect of DBBQ on the potential determining step (right).[54]

1. Introduction

Bruce's group found that the introduction of DBBQ in the electrolyte can promote the solution phase formation of Li_2O_2 , which further enhances the discharge capacity (Figure 1.34).[16] In the exiting of DBBQ, the discharge capacity exhibits an amazing improvement, which is 80-100 times higher than the battery without DBBQ in the electrolyte. The adding of DBBQ in the electrolyte can change the reaction pathway into a lower binding energy route, which positively affects the formation of LiDBBQO_2 intermediate. Finally, the soluble LiDBBQO_2 intermediators will move to the adjacent solution and form Li_2O_2 in solution. The formation of discharge products in solution can restrain the formation of passivation film in the electrode surface, which can block the oxygen and electrolyte diffusion pathways.

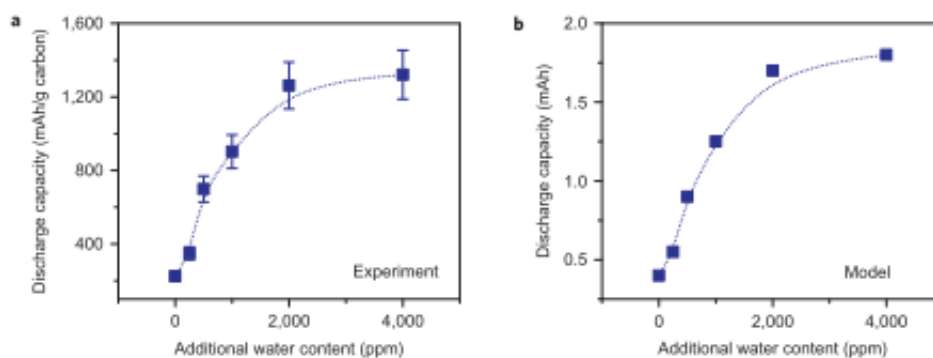


Figure 1.35. The relationship between the discharge capacity and water content in the electrolyte.[22]

Although they have no redox center and cannot operate as redox shuttles or redox mediators, water and some protic molecules can also increase the discharge capacity and current density (similar effects to ORR catalysts).[75],[76],[22] Gasteiger's group reported the enhancement of discharge capacity by adding water in the electrolyte (Figure 1.36).[77] They found that Li-O_2 battery capacity improves at a relatively low water concentration.[77] One possible reason is the fact that water can increase the solubility of the discharge products in the electrolyte, making it impossible for the solid type passivation film to form. The increase of solubility may be ascribed to the connections between the discharge products and the carbon substrate becoming weaker with the help of water. Another possible reason is the fact that discharge products grow on the electrode in the form of cracked layers. The solid-state diffusion of oxygen through a Li_2O_2 deposit is very slow in room temperature. However, the cracked layers make oxygen diffusion easier compared to the film type discharge products, leading to enhancement of the discharge capacity. Aetukuri et al. has also discovered that the discharge capacity continues to increase with the increase of the water content when the water content is lower than 3000 ppm (Figure 1.35).

1. Introduction

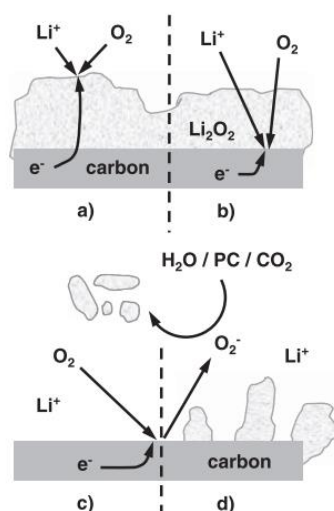


Figure 1.36. The possible mechanisms of ORR process at the air electrode for Li-O₂ batteries with aprotic organic electrolyte.[77]

Li et al. reported applying trace amount of water in electrolytes to catalyze the cathode reactions of lithium-oxygen cells.[72] The cathode used in this research is ruthenium and manganese dioxide nanoparticles supported on carbon black Super P. Applying trace amount of water and ruthenium and manganese dioxide based cathode results in a small discharge/charge potential gap of 0.32V and superior cycling stability of 200 cycles.[72] Grey' team studied the synergistic effect of DBBQ and H₂O on the oxygen chemistry in a nonaqueous Li-O₂ battery.[78] Water stabilizes the quinone monoanion and dianion, shifting the reduction potentials of the quinone and monoanion to more positive values (vs Li/Li⁺).[78] Water can slow down the reaction of reduced quinone with O₂ through the formation of LiDBBQ.nH₂O mediator. LiDBBQ.nH₂O can diffuse for a longer distance away from the electrode surfaces before it reduces O₂. It enlarges the reaction zone in the electrolyte and allows the reactions to occur deeper in the electrolyte.[78] When water and the quinone are used together, the battery discharge voltage, rate, together with capacity, considerably increases and fewer side reactions occur.[78] This is due to the fact that the cell discharge operates via a two-electron oxygen reduction reaction to form Li₂O₂.

Some soluble catalysts can serve as redox mediators to reduce the charge potentials. This kind of catalysts can affect the chemical oxidization process of discharge products. An example could be the soluble LiI, which can reach the interior of the porous air electrode to promote the decomposition of nonconductive discharge products in lower voltage.[32],[79],[80] LiI can reduce decomposition voltage of Li₂O₂ through the oxidation reaction of $3\text{I}^- \rightarrow \text{I}_3^- + 2\text{e}^-$ and $\text{I}_3^- \rightarrow 3/2\text{I}_2 + \text{e}^-$ and chemical reaction of $2\text{Li}_2\text{O}_2 + 6\text{I}_2 \rightarrow 4\text{LiI}_3 + 2\text{O}_2$ (Figure 1.37).[79],[79] Lim et al. reported applying soluble catalyst combined with a hierarchical nanoporous air electrode.[32] The battery,

1. Introduction

combining an ideal air electrode and a soluble catalyst, can deliver a high reversible capacity of 900 times (1000 mAh g^{-1}) up to 900 cycles with reduced polarization ($\sim 0.25 \text{ V}$).[32] Not only lithium ions and oxygen, but also soluble catalysts can be rapidly transported through the porous three dimensional network of the air electrode.[32] Watanabe's group explored the influence of electrolyte solvent (tetraglyme (G4) and dimethyl sulfoxide (DMSO)) and concentration on the redox potential for both I^-/I_3^- and I_3^-/I_2 redox couples.[55] DMSO solvent provides the most effective redox mediation among the electrolytes. However, it also exhibits the highest degree of redox shuttling.[55] They suggested that future cell design utilizing a mediator should balance both effective limitation of redox shuttle and easiness of mediator diffusion to discharge products. Shao-Horn's team carefully studied the role of iodide in the formation of lithium hydroxide in Li-O_2 batteries.[80] They reported that adding iodide to electrolytes containing water can promote the formation of $\text{LiOOH}\cdot\text{H}_2\text{O}$, $\text{LiOH}\cdot\text{H}_2\text{O}$ and LiOH at the expense of Li_2O_2 . When the ratio of $\text{H}_2\text{O}:\text{LiI}$ was lower than 5, LiOH instead of Li_2O_2 was formed.[80] Burke et al. confirmed that LiI and H_2O additives promoted efficient $4 e^-$ oxygen reduction to LiOH in discharge.[81] Unfortunately, LiOH is not reversibly oxidized to O_2 on charge and a complicated mix of redox shuttling and side reactions is observed.[81] Zhou's group reported that LiI can promote the superoxide-related nucleophilic attack toward electrolyte by catalyzing the decomposition of peroxide intermediate, resulting in the accumulation of LiOH . [82] However, Grey's team reported the reversibly formation and decomposition of LiOH with the catalysis of LiI . [33] They used LiI and H_2O as additives in electrolyte to reversibly form and remove crystalline LiOH during discharge/charge.[33] This leads to high specific capacities, excellent energy efficiency (93.2%) with a small voltage gap of only 0.2 volt.[33]

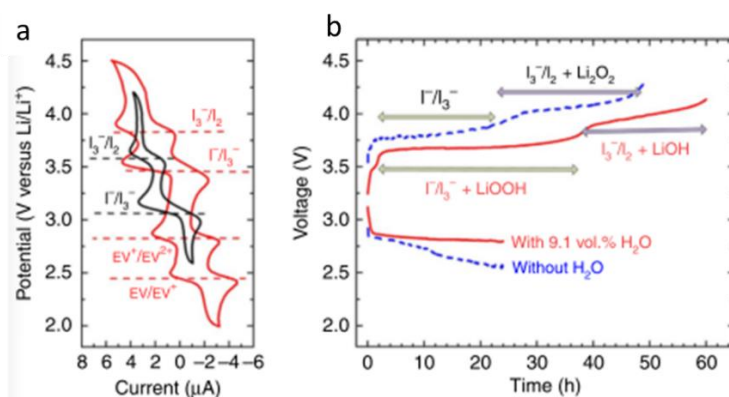


Figure 1.37. Electrochemical performance of Li-O_2 cells with LiI in the electrolyte.[79]

TTF were also explored as a redox mediator, which can improve the recharge kinetics of Li-O_2

1. Introduction

Moreover, the carbon instability is significantly mitigated (<0.008% decomposition per cycle compared with 0.12% without mediators) through the forming/decomposing discharge products in solution and avoiding high charge potentials.[57] Kwak et al. synthesized antimony tin oxide (ATO) with a porous inverse opal structure as cathode and applied DBBQ and TEMPO as ORR and OER catalysts in electrolyte.[86] Batteries with dual soluble catalysts showed a synergistic combination without any negative interference with each other, which results in higher capacity and rechargeability.[86] The battery presented a cycle stability of 50 cycles in a voltage range of 2.0–4.8 V with a cut-off capacity of 0.5 mAh and a current density of 0.0442 mA cm⁻². Zhu et al. studied the use of soluble redox catalysts (EV (ethyl viologen) and LiI) for large-scale energy storage.[87] This device enables the reversible formation and decomposition of Li₂O₂ via redox targeting reactions in a gas diffusion tank, which obviates the passivation and pore clogging of the cathode. [87] The battery can cycle 30 times with a cut-off capacity of 2.0 mAh and a current density of 0.125 mA cm⁻².

2. Aim of the thesis

2. Aim of the thesis

Li-O₂ batteries have been studied for decades of years, which are promising to be more safety and higher energy density than traditional Li-ion batteries. Carbon materials are widely explored as cathode electrode materials for Li-O₂ batteries due to their good conductivity for electron transfer, large pore volume to deposit the discharge products, and porous structure for oxygen diffusion. However, the electrochemical activity of carbon material is greatly influenced by pore size, morphology and functional groups. Two kinds of carbon (PCW and rGO) were applied as cathode materials for Li-O₂ batteries in this work and their electrochemical activity was also studied. We want to study the influence of raw material structure on electrochemical performance.

The catalytic activity for pure carbon is not so ideal, which cannot high efficiently catalyze the formation/decomposition of discharge products. In addition, carbon surface is riddled with dangling bonds, which will aggravate the formation of passivation film on electrode surface. The application of solid catalysts are the most widely used methods to enhance the catalytic activity. Transition metal oxides as solid catalysts for Li-O₂ batteries stand out in series of solid catalyst due to their low cost and high catalytic activity. However, the detailed catalytic mechanism of transition metal oxides is unclear. Only some research groups reported that transition metal oxides can enhance the mass transport of LiO₂ species. In this thesis we want to synthesize different solid catalysts to improve the catalytic activity of oxygen electrode and study their catalytic mechanism in details.

The catalytically active region, solid-solid interface (the immobile area next to the interface between the catalysts and the discharge products), was limited for solid catalysts. In this thesis, we want to apply both OER catalyst and ORR catalyst in electrolyte to overcome this limitation and promote the formation/decomposition of discharge products in solution.

Not only the developing of advanced oxygen electrode materials and catalysts are very important, but the deep study of the function mechanism through modern testing methods is also significant. In this thesis, we want to apply SEM, XRD and Raman tests to determine the structure evolution of discharge products and cathode materials during discharge and charge process for further understanding the catalytic mechanism.

3. Experimental part

3. Experimental part

3.1 Material preparation

3.1.1 Preparation of porous carbon from biomass

The biomass-derived carbon used as electrode material was prepared by hydrothermal carbonization and KOH activation. Firstly, 4.0 g cleaned wood powder was uniformly dispersed by ultrasonic treatment in 80 ml of distilled water containing 2 ml of sulfuric acid, then the mixture was transferred into a stainless steel autoclave and heated at 200 °C for 12h. Then the collected solid biochar was uniformly mixed with KOH ($m_C/m_{\text{KOH}} = 1/1.5$) and the mixture was activated at 850 °C for 2 h with heating rate of 3 °C min⁻¹ under flowing N₂ atmosphere. At last, the obtained black powder was washed with 10 wt% HCl and distilled water and dried in an oven at 80 °C to get the final porous carbon materials (PCW).

3.1.2 MnO₂@rGO material preparation

MnO₂@rGO was prepared by mixing 100 mg rGO with 500 ml 1mM KMnO₄/5 mM Na₂SO₄. The mixture was stirred for 1h. This procedure relies on the chemical reaction between KMnO₄ and graphitic carbon to generate MnO₂. The multilayer rGO served as reactive template to grow the MnO₂. Na₂SO₄ acts as a buffering agent to keep the solution neutral. The obtained suspension was collected by suction filtration and washed with distilled water several times. The resulting product was dried at 80°C for 12 h in the oven.

3.1.3 Co₃O₄ nanoplate preparation

Co₃O₄ was prepared as shown on Figure 3.1. Typically, 4 mmol Co(AC)₂ were dissolved in a mixture of 6 ml ethylene glycol and 74 ml deionized water and stirred for 10 min. Then 0.22 mg urea was added to the solution. The mixture was stirred for another 30 min. Afterwards 60 mg rGO (China, Dasheng graphene Co. Ltd) was added to the solution and stirred further for 30 min. After thorough mixing, the suspension was transferred into a 100 ml steel autoclave. The autoclave was sealed, heated to 170 °C at a rate of 3 °C/min and maintained for 12h at this temperature. After cooling to room temperature, the solid product was collected and washed with deionized water several times. The obtained solid product was dried in the oven at 80 °C overnight, and calcined at 500 °C for 1h in air (heating rate 5 °C/min). Final solid product Co₃O₄ was received.

3. Experimental part

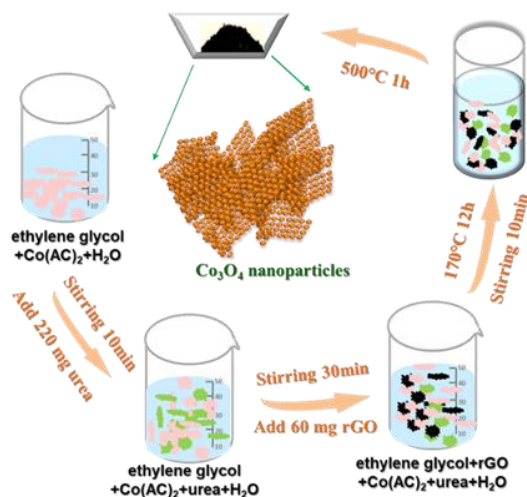


Figure 3.1. Schematic of synthesis process and material structure of Co_3O_4 nanoparticles;

3.2 Cell preparation and electrochemical measurements

3.2.1 Preparation of electrolytes

The normal electrolyte used in our Li- O_2 battery is 0.25 M lithium bis(trifluoromethane)sulfonamide (LiTFSI) in tetra(ethylene) glycol dimethyl ether (TEGDME) referred to as LiTFSI. The other three electrolytes, (i) 0.25 M LiTFSI in TEGDME with 0.05 M LiI referred to as LiTFSI/LiI, (ii) 0.25 M LiTFSI in TEGDME with 0.01 M DBBQ referred to as LiTFSI/DBBQ, (iii) 0.25 M LiTFSI in TEGDME with 0.05 M LiI and 0.25 M LiTFSI referred to as LiI LiTFSI/DBBQ/LiI, were also applied in our experiment.

3.2.2 Preparation of electrodes

Oxygen electrodes based on PCW were prepared by coating the mixture of 85 wt% PCW material and 15 wt% poly(vinylidene fluoride) (PVDF6020, Solvay) binder with N-methylpyrrolidone (NMP, Merck KGaA) solvent on carbon cloth (H23 I2, QUINTECH, diameter ~11 mm). The mass loading of PCW is ~1.5 mg. rGO based electrodes were made in the same way with a weight ratio of 6:4 (rGO:PVDF). The mass loading of rGO is ~0.4 mg.

For MnO_2 @rGO material, it was firstly mixed with PVDF in NMP solvent in a mass ratio of 7:3 (MnO_2 @rGO:PVDF). Then the slurry was coated on carbon cloth (diameter ~11 mm). The mass loading of MnO_2 @rGO is ~0.6 mg. For Co_3O_4 material, oxygen electrodes was prepared by mixing Co_3O_4 , rGO and PVDF in a weight ratio of 5:3:2 in NMP solvent. After thoroughly mixing,

3. Experimental part

the slurry was coated on carbon cloth (diameter ~11 mm). The mass loading of Co_3O_4 and rGO is ~1.4 mg.

After coating, all electrodes were dried at 80 °C overnight in an oven.

3.2.3 Battery preparation

Li- O_2 cells were assembled using a Swagelok® cell construction (Figure 3.2). Li- O_2 battery with Li foil, glass fiber separator (Whatmann® GF/B), cathode and the electrolyte (220 μL) were assembled inside an Ar-filled glove box (<0.1 ppm of both oxygen and H_2O).

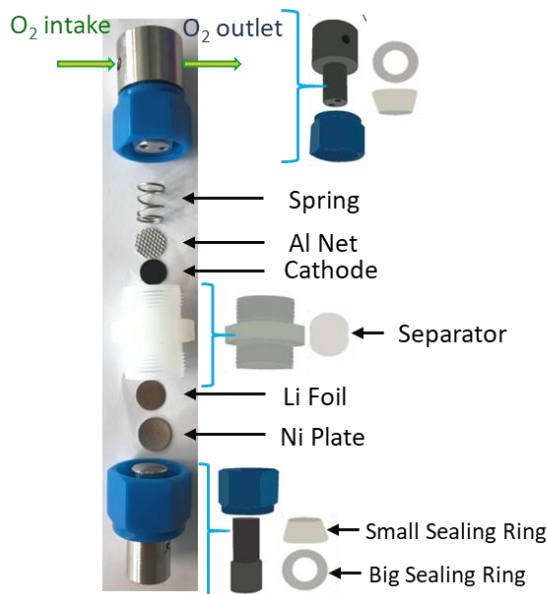


Figure 3.2. Schematic of Lithium-oxygen batteries.

3.2.4 Electrochemical measurements

Oxygen was purged into the cell stack during the electrochemical cell test. Firstly, oxygen (5.0) flowed for 2 h (10 ml/min), then the flow kept a constant rate of 5 ml/min during battery cycling. The pipe used for the oxygen transport is made of polyethylene (PE). Water absorption values for PE pipe at room temperature is ~0.02%. Water absorption is expressed as increase in weight percent of a PE under a humid at a specified temperature ~23°C for 24 hours (increase in weight, % = $100 \times (\text{wet weight} - \text{conditioned weight}) / \text{conditioned weight}$). A VSP (Bio-Logic, France) multichannel potentiostat test system was applied to perform the electrochemical test. CV (cyclic voltammetry) tests and galvanostatic discharge/charge measurements were applied for the

3. Experimental part

electrochemical performance analysis. Galvanostatic charge-discharge tests were carried out in two modes: full discharge/charge between 2.0-4.6/2.3-4.5 V and capacity controlled (500/1000 mAh g⁻¹) discharge/charge. All electrochemical tests were carried out at room temperature. The capacity with unit of mAh g⁻¹ is calculated based on the weight of carbon and catalyst. The capacity with unit of mAh g_{rGO}⁻¹ is calculated based on the weight of rGO.

3.3 Characterizations of the raw materials and the discharged/charged electrodes

3.3.1 Scanning electron microscope

SEM (scanning electron microscope, Zeiss Supra 55) was applied to characterize the morphology of the raw catalyst materials and the pristine/discharged/charged electrodes. The discharged and charged electrodes were removed from the cells inside the glovebox and placed inside an airtight transport.

3.3.2 X-ray diffraction

X-ray diffraction (XRD) patterns of the raw materials and the pristine/discharged/charged electrodes were examined on STOE STADI P with Ag K_α radiation ($\lambda=0.55941 \text{ \AA}$), Mo K_α radiation ($\lambda=0.70932 \text{ \AA}$), and Co K_α radiation ($\lambda=1.78896 \text{ \AA}$) at room temperature in Debye-Scherrer geometry (the capillary diameter: 0.5 mm). XRD with Mo/Ag K_α radiation has higher energy and stronger penetration than Co K_α radiation, which makes it superior to analyze structures of metallic compounds. Hence we apply XRD with Ag/Mo K_α radiation to analyze the structure of raw catalyst materials. XRD with Co K_α radiation has high absorption for lithium compounds, which makes it superior to analyze the structure of discharge products. Rietveld refinement was employed to analyze the diffraction data of the discharge products using the FullProf software package.[89]

3.3.3 Raman spectroscopy

For Raman measurement, a Labram Evolution HR from Horiba was used, which was equipped HeNe-Laser (633 nm, 17 mW) and a CCD detector (Horiba). Besides, a 600 grating was used to split the measurement signal. For the raw material, a $\times 100$ objective was used for the measurements and the data was collected for 30 seconds with 4.25 mW of the laser and five measurements were added to reduce signal noise. A $\times 50$ objective was used for the measurements

3. Experimental part

of the pristine/discharged/charged electrodes. The data was collected for 60 seconds with 4.25 mW of the laser and five measurements were added to reduce signal noise. The discharged and charged electrodes were removed from the cells inside the glovebox and placed inside an airtight container with a quartz window.

3.3.4 Thermal analysis

Thermal Analysis of WC850 and MnO₂@rGO (TG, Netzsch Jupiter 449 C) was carried out in Argon and air atmosphere with a heating rate of 5 °C min⁻¹ to 1000 °C.

3.3.5 X-ray photoelectron spectroscopy

The surface elemental compositions and oxidation state of elements were determined by X-ray photoelectron spectroscopy (XPS), and it was performed in a K-Alpha spectrometer (ThermoFisher Scientific, East Grinstead, UK) using a microfocused, monochromated Al K α X-ray source (400 μ m spot size). An Argon Glove box directly attached to the spectrometer enables the air free introduction of the samples in the load lock. The kinetic energy of the electrons was measured by a 180° hemispherical energy analyzer operated in the constant analyzer energy mode (CAE) at 50 eV pass energy for elemental spectra. The K-Alpha charge compensation system was employed during analysis, using electrons of 8 eV energy, and low-energy argon ions to prevent any localized charge build-up. Data acquisition and processing using the Thermo Advantage software is described elsewhere. The spectra were fitted with one or more Voigt profiles (BE uncertainty: ± 0.2 eV) and Scofield sensitivity factors were applied for quantification. All spectra were referenced to the C 1s graphitic peak at 284.4 eV binding energy controlled by means of the well-known photoelectron peaks of Cu, Ag and Au respectively.

3.3.6 X-ray absorption near edge structure

X-ray absorption near edge structure (XANES) measurements were carried out at PETRA-III beamline P65 at DESY in Hamburg and recorded in quick-XAS (7 min/spectrum) mode in fluorescence geometry using a PIPS diode. The Mn K-edge of MnO₂@rGO was measured at room temperature with a Si (111) crystal monochromator. The energy was calibrated by the absorption edge of Mn foil, which was measured in parallel with other samples. Tstandard materials were MnO, Mn₂O₃, and MnO₂. The XAS spectra were processed with the DEMETER software package.[90]

3. Experimental part

3.3.7 Transmission electron microscopy

To characterize further the morphology and structure of the samples, transmission electron microscopy (TEM) was employed. The sample was dispersed in high purity ethanol and deposited onto a carbon-coated grid gold grid. The TEM analysis was performed on a Titan 80–300 electron microscope (FEI), equipped with a CEOS image spherical aberration corrector, high angle annular dark field (HAADF) for scanning transmission electron microscopy (STEM) detector and a Tridiem Gatan image filter (GIF). The microscope was operated at an accelerating voltage of 300 kV.

4. Results and discussion

4. Results and discussion

4.1 Carbon materials as oxygen electrodes for Li-O₂ batteries

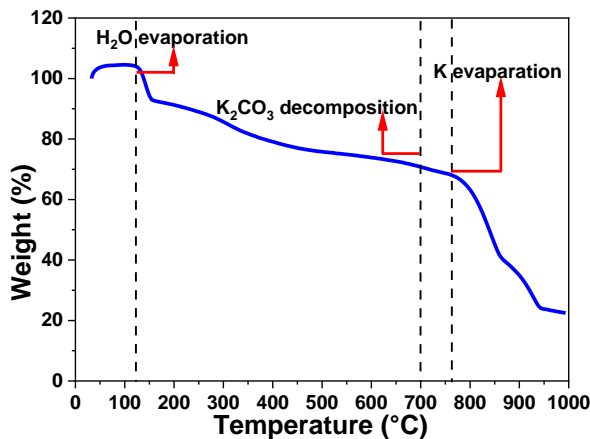


Figure 4.1. Thermogravimetric curve of the HWC and KOH (1:1.5) mixture at 5 K min⁻¹ in Ar.

The obtained PCW sample was analyzed by SEM to investigate the morphology. Natural wood powder (WP) exhibits multilayer (Figure 4.2b). Moreover, wood powder is mainly comprised of cellulose, hemicellulose and lignin, which can donate as excellent source for carbon synthesis.[91] The fabrication scheme of PCW specie is shown in Figure 4.2a, which includes a hydrothermal carbonization process in acidic condition and a high temperature KOH activation process. During hydrothermal treatment, the feedstock undergo the polymerization and carbonization process to self-assemble into nanoparticles (HPW) (Figure 4.2c).[92] KOH activation, which involves several complicated chemical reactions at different temperature stages, is a widely used method to generate porous structure in carbons. The activation includes incipient reactions between carbon and KOH ($2C+6KOH \rightarrow 2K+3H_2+3K_2CO_3$), and further multiple reactions, including the reduction of potassium (K) compound to form metallic K ($K_2CO_3+2C \rightarrow 2K+3CO$, $C+K_2O \rightarrow 2K+CO$), the oxidation of carbon to carbon oxide and carbonate ($CO_2+C \rightarrow 2CO$), and other complex simultaneous reactions between various active intermediates.[93] The weight loss caused by the generating of escapable gas and gaseous metallic K (boiling temperature: 762 °C) in a temperature region of 50-1000 °C is shown in Figure 4.1, demonstrating that the KOH activation terminates at ~ 900 °C and the drastic gas producing active reactions mainly arise from 700 °C to 900 °C. The porous structure of PCW is generated from the removing of inorganic products by acid, which will form micropores and small mesopores on the closed meso/macropore walls.

4. Results and discussion

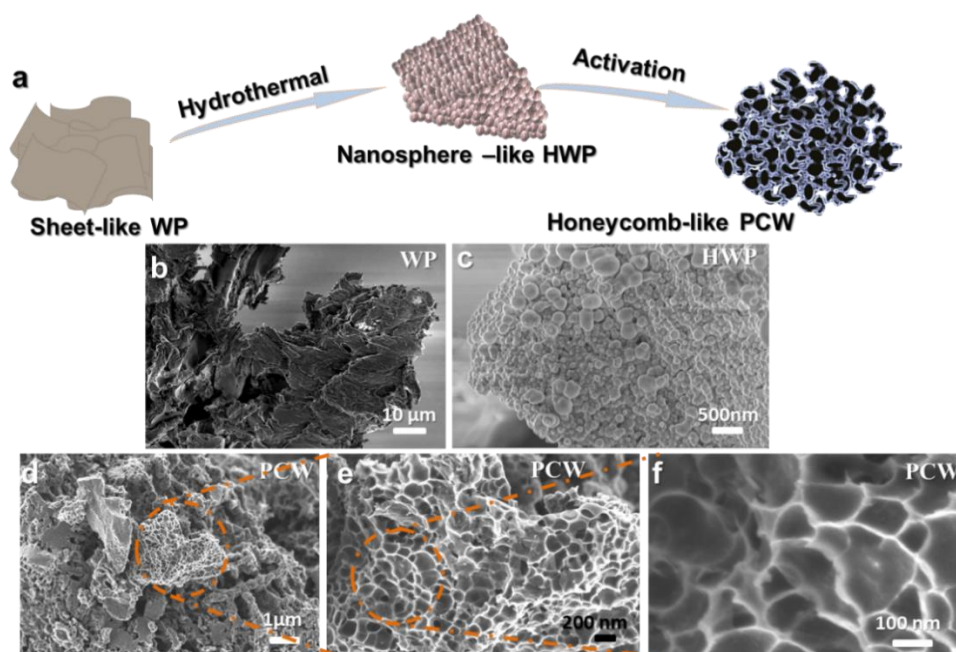


Figure 4.2. (a) Schematic of material structure in synthesis process for the wood-derived carbon; (b) SEM image of the WP with multilayer sheet-like structure; (c) SEM image of HWP, which can form small particles of several hundred nanometers; (d), (e) and (f) SEM and high resolution SEM images of the PCW, which demonstrate a honeycomb-like porous structure.

PCW exhibits a 3D honeycomb-like structure consisting of numerous interconnected macropores (generated from the cross-linking between the carbon walls) with a diameter from tens to hundreds of nanometers (Figure 4.2d and e). High resolution SEM image (Figure 4.2f) further confirms their highly interconnected 3D porous structure with super thin carbon wall.

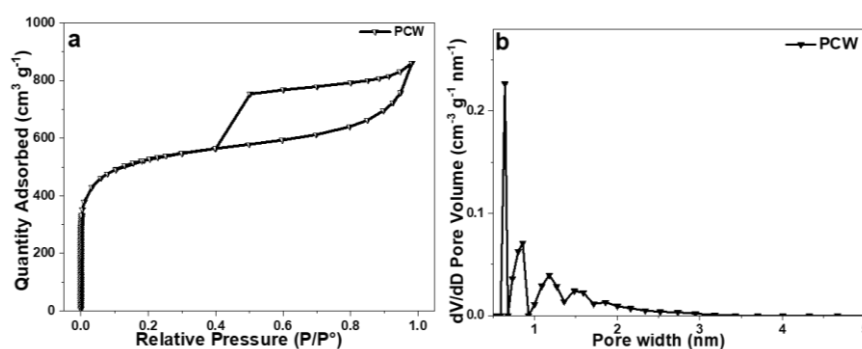


Figure 4.3. (a) Nitrogen adsorption/desorption isotherms of the honeycomb-like PCW samples, and (b) Pore size distribution calculated from the DFT method.

The surface and pore size distribution of PCW was analyzed by the nitrogen adsorption/desorption measurement combining advanced analysis based on density functional theory (DFT, pore distribution analysis). The nitrogen adsorption/desorption isotherms (Figure 4.3a) exhibit type-I

4. Results and discussion

adsorption isotherms with steep uptakes in low relative pressure (below $P/P_0 = 0.05$), capillary condensation step in the middle and high relative pressure range and type-H4 hysteresis. The obvious Type-I adsorption isotherms in low relative pressure and capillary condensation step in the middle and high relative pressure indicate that PCW possesses abundant microporous structure and certain amount of mesopores. The type-H4 hysteresis, which are produced by the sheet-like structure (referring to the super thin carbon walls), demonstrate the presence of pores with uniform shape and size. The specific BET surface area of PCW is $1856 \text{ m}^2 \text{ g}^{-1}$. Figure 4.3b displays the result of the pore size analysis obtained from a hybrid nonlocal DFT model. The PCW sample exhibits scattered hierarchical pore structures with abundant micropores and a few mesopores.

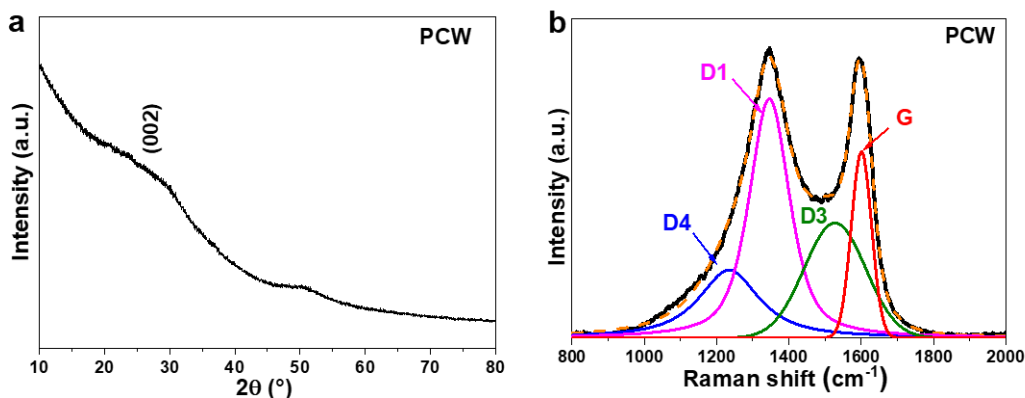


Figure 4.4. (a) XRD ($\lambda=1.78896 \text{ \AA}$) pattern of the PCW; (b) Deconvoluted Raman spectra of PCW.

XRD measurement was carried out to characterize the crystallinity and phase purity of PCW sample. PCW possesses two broad diffraction reflections in XRD patterns (Figure 4.4a), which is the typical characteristics of graphitic carbon.[94],[95] Raman spectroscopy analysis was applied to further investigate the structure of the PCW. PCW exhibits two distinct bands located around 1345 cm^{-1} (D-band) and 1592 cm^{-1} (G-band).[96] A portion of the resulting averaged spectrum ($800\text{-}2000 \text{ cm}^{-1}$) was also deconvoluted into four component bands (labeled as D1, D3, D4 and G) based on actual visual evidence for their presence in the averaged band envelope (Figure 4.4b). The G-band is assigned to the E_{2g} phonon of sp^2 -bonded carbon atoms, which is the characteristic feature of graphitic layers.[97],[98] The D1-band is assigned to the breathing mode of κ -point phonons with A_{1g} symmetry, which corresponds to disordered carbon or defective graphitic structures.[97],[98] The D3 peak shows the existence of fragments or functional groups in the amorphous phase which may also change the C–C and C=C stretching vibrations of the polyene-like structure (D4) [99] The area portion calculated from D3, D1 and G peaks presents the relative degree of amorphous phases, disordered and graphitic, respectively. Area ratio of G-band and D1-

4. Results and discussion

band (I_G/I_D) value could well indicate the graphitization degree of carbon material. I_G/I_D value of raw PCW is 0.40. While the area ratio of D3 band and the total four bands (named as I_{D3}/I_T) reflects the amount of fragments or functional groups in amorphous phases.[99]

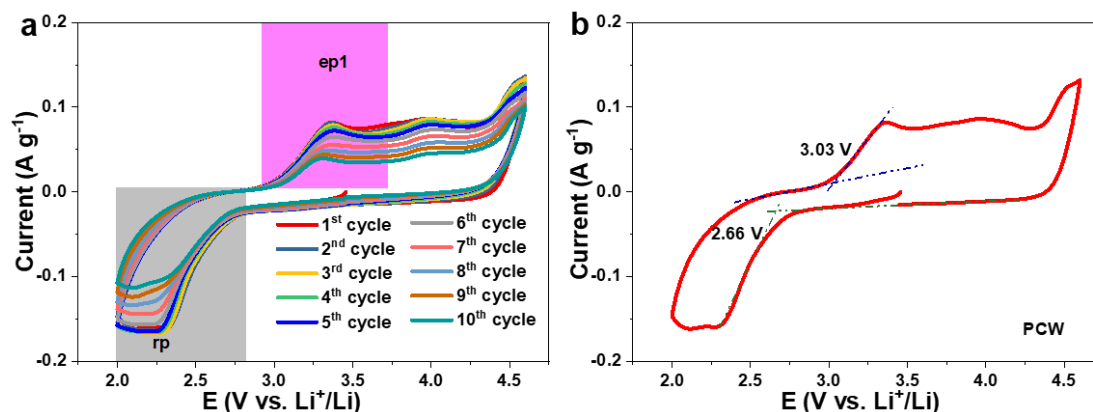


Figure 4.5. (a) Cyclic voltammograms of the beginning 10 cycles for PCW based Li-O₂ battery at a scan rate of 0.1 mV s⁻¹ between 2.0-4.6 V;; (b) The initial CV curve of PCW based Li-O₂ battery with the corresponding onset potential.

The electrochemical activity of PCW material was investigated by cyclic voltammetry (CV) in the voltage of 2.0 - 4.6 V. All the CV curves show one oxygen reduction peak (rp) and one oxygen evolution peaks (ep1) (Figure 4.5a). It can be clearly seen that the currents in ORR and OER process are all very small ($< 0.2 \text{ A g}^{-1}$), which indicates poor electrochemical activity. Moreover, the current in oxygen reduction process and oxygen evolution process decays very faster during cycling, which means poor reversibility. Onset potential is the potential where all the thermodynamic and kinetic barriers become downhill. It is usually considered as an important indication for the catalytic activity in electro-catalysis. For further study the electrochemical activity on reduction and oxidation processes, onset potential was applied. Onset potential is the potential at which current starts to rise (a reaction starts taking place). We determine onset potential by drawing tangents from the rising current and baseline current. The intersection of the tangents and baselines is called onset potential. The onset potential for PCW in ORR process is 2.66 V and in OER process is 3.03 V (Figure 4.5b). The low onset potential in ORR process also indicates that PCW possesses poor catalytic activity in electro-catalysis for Li-O₂ batteries.

Galvanostatic discharge-charge measurements were also carried out to further clarify the electrochemical activity of PCW. The battery was operated in a voltage range of 2.0-4.6 V vs. Li⁺/Li at a current of 50 mA g⁻¹ for 9 full cycles (Figure 4.6). The PCW based battery delivers a maximum discharge capacity of 1216 mAh g⁻¹, and the discharge capacity is only 331 mAh g⁻¹ at

4. Results and discussion

the ninth cycle. Discharge capacity decays to ~37% of initial capacity after 9 cycles. The PCW based Li-O₂ battery presents low discharge capacity and poor capacity retention ability. It can be concluded that the microporous active carbon (PCW) possesses poor electrochemical activity when it was applied as oxygen electrode for Li-O₂ battery.

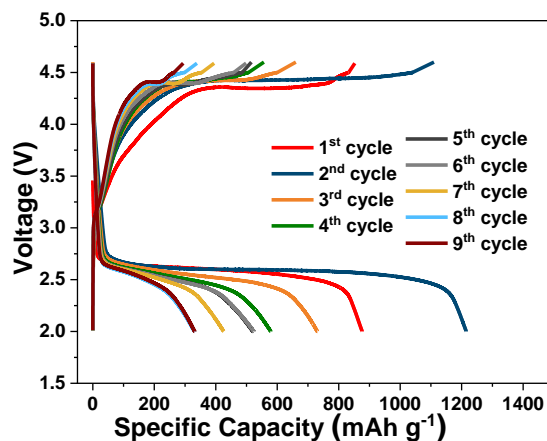


Figure 4.6. Galvanostatic discharge-charge curves of PCW based battery at a current density of 50 mA g⁻¹ between 2.0-4.6 V;

Galvanostatic discharge-charge measurements were also carried out on pure carbon cloth collector to study its influence on total capacity of my Li-O₂ batteries. The battery was operated in a voltage range of 2.0-4.5 V vs. Li⁺/Li at a current of 100 μA for 9 full cycles (Figure 4.7). It delivers a maximum discharge capacity of 0.15 mAh, and the discharge capacity is only 0.06 mAh at the ninth cycle. The mass loading of PCW is ~1.5 mg. For the initial cycle, carbon cloth devotes about 100 mAh g⁻¹ capacity to PCW based battery. For the 9th cycle, the capacity devoting is ~ 40 mAh g⁻¹. These values indicate that carbon cloth contributes not too much capacity to the total capacity of PCW based battery.

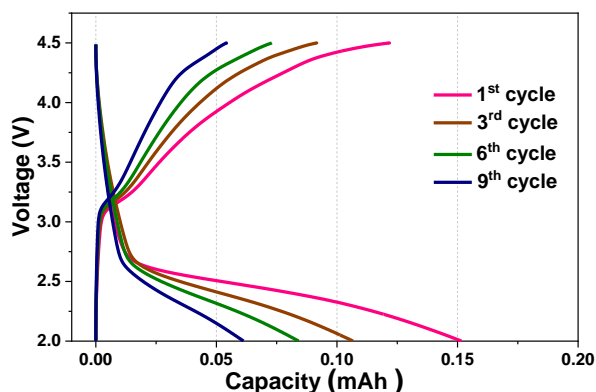


Figure 4.7. Galvanostatic discharge-charge curves of pure carbon cloth based battery at a current density of 100 μA between 2.0-4.5 V;

4. Results and discussion

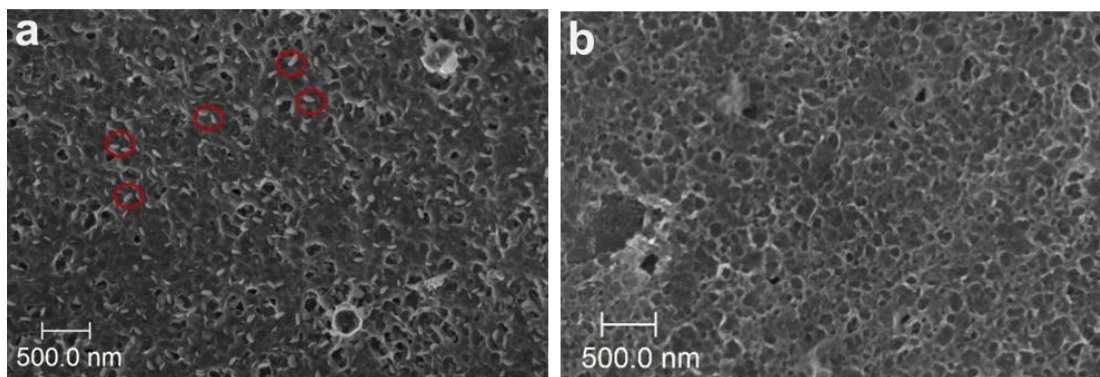


Figure 4.8. SEM images of the discharged (a) and charged (b) PCW electrodes.

The morphology of the discharge products was investigated by SEM. The discharged electrode of PCW exhibits only few rice-shape discharge products on surface (Figure 4.8a), which corresponds to its low discharge capacity. The discharge products disappear after charged to 4.6 V (Figure 4.8b), which demonstrates the decomposition of discharge products in charge process.

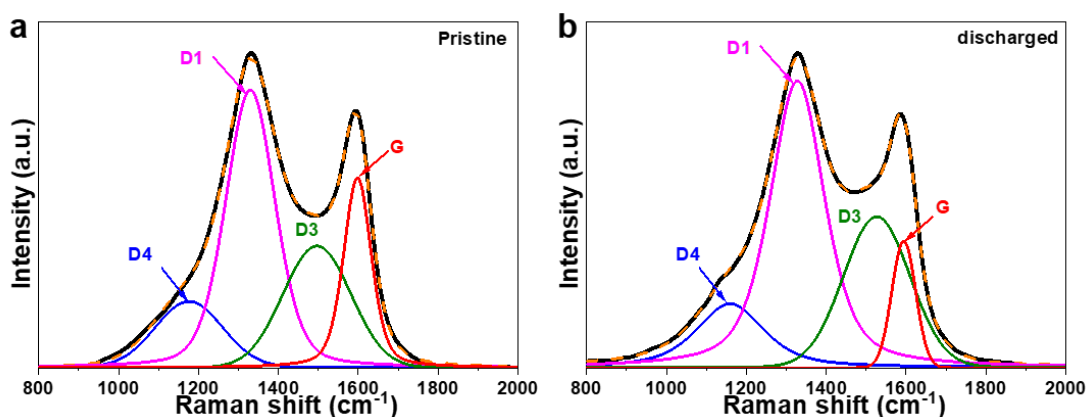


Figure 4.9. Deconvoluted Raman spectrum of the pristine/discharged PCW electrodes.

To further study the PCW structure evolution in ORR process, Raman spectra was applied. The Raman spectra in the range of 800-2000 cm⁻¹ was deconvoluted into four component bands (D1, D3, D4 and G) (Figure 4.9). As we talked above, I_G/I_D value could indicate the graphitization degree of carbon material and I_{D3}/I_T value reflects the amount of fragments or functional groups in amorphous phases. I_G/I_D and I_{D3}/I_T values for pristine PCW electrode are 0.40, 0.24. After the discharge process, I_G/I_D and I_{D3}/I_T values are 0.17 and 0.28. I_{D3}/I_T value of PCW electrode increase obviously from 0.24 to 0.28 after discharge (Table 1), which indicates an obvious increase of fragments or functional groups in the amorphous phase. Moreover, I_G/I_D value decreases very much in the discharge process, which indicates the destroying of carbon structure. The heavy damage of carbon structure may attribute to the high content of O for PCW (8.4 at%), which will

4. Results and discussion

induce more surface function group. The O-containing function group can be easily attacked by LiO_2 species, which will lead to the decrease of graphitization degree.

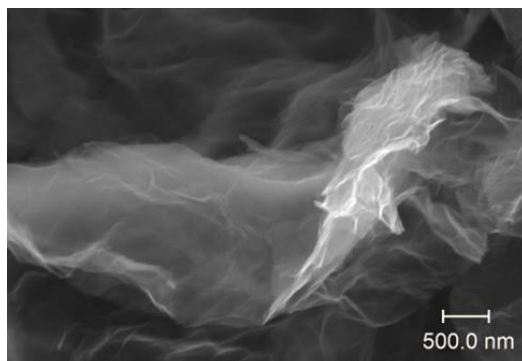


Figure 4.10. SEM image of rGO.

Porous air electrodes play variable roles in the Li- O_2 battery system: (i) it acts as an active catalyst materials for oxygen reduction/oxygen evolution reaction (ORR/OER).[33] (ii) it serves as conductive framework for electron transfer.[35] (iii) it provides as a matrix to deposit discharge products.[36],[37] (iv) it has porous network that supports the diffusion of oxygen.[38],[1],[33] Considering the poor electrochemical activity of PCW as oxygen electrode for Li- O_2 batteries. Here we further applied rGO as oxygen electrode for Li- O_2 batteries due to its good electronic conductivity, low cost, and large surface area. SEM of raw rGO sample (Figure 4.10) clearly shows 3D multilayer structure.

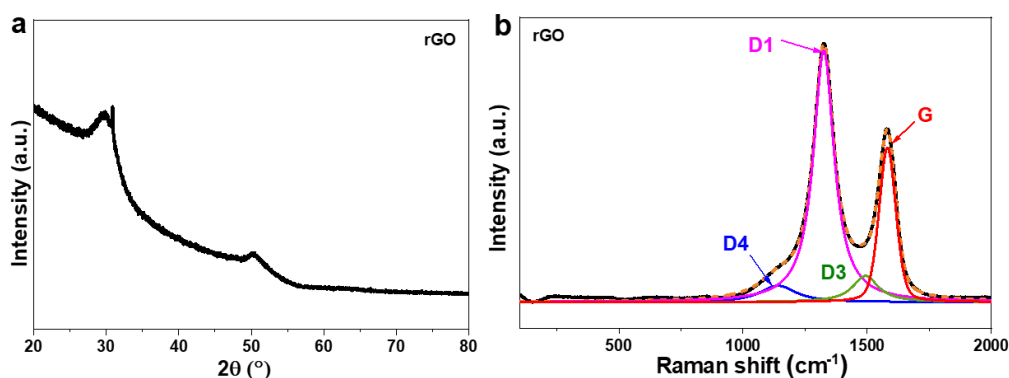


Figure 4.11. XRD ($\lambda=1.78896 \text{ \AA}$) pattern of rGO (a); (b) Deconvoluted Raman spectra of rGO.

XRD measurement was carried out to characterize the crystallinity and phase purity of rGO sample. rGO possesses two broad diffraction reflections (29.7° and 50.2°) in XRD patterns (Figure 4.11a). The d-spacing of the first diffraction corresponds to that of the (002) reflection in graphite and therefore most likely originates from small domains of stacked rGO sheets. The first

4. Results and discussion

diffraction position yields a mean inter graphene spacing of 0.35 nm, which is substantially larger than that of graphite ($c/2 = 0.3354$ nm). Raman spectroscopy analysis was applied to further investigate the structure of the rGO. rGO exhibits two distinct bands located around 1345 cm^{-1} (D-band) and 1592 cm^{-1} (G-band) (Figure 4.11b).[96] I_G/I_D value for rGO is 0.37.

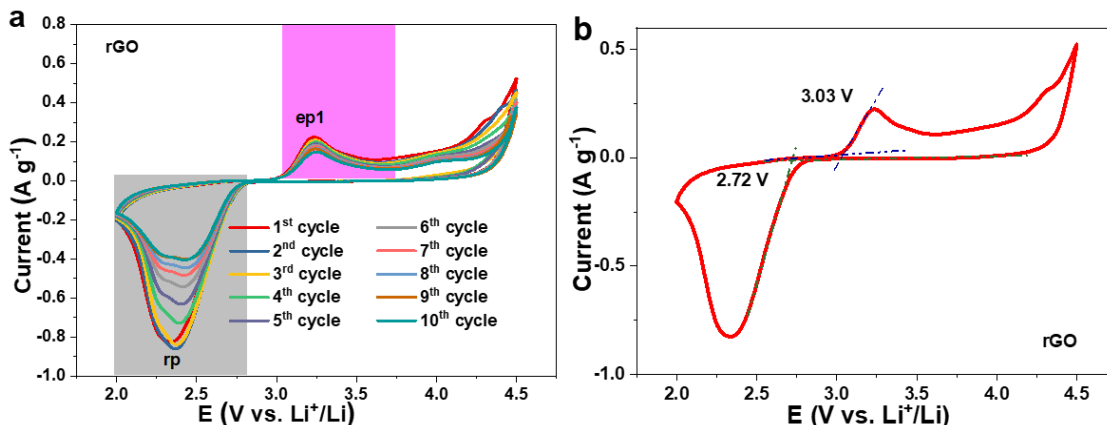


Figure 4.12. (a) CV curves of the beginning 10 cycles for rGO based Li-O₂ battery at a scan rate of 0.1 mV s^{-1} between 2.3-4.5 V; (b) The initial CV curve of rGO based Li-O₂ battery with the corresponding onset potential.

All the CV curves of rGO based Li-O₂ battery shows one oxygen reduction peak (rp) and one oxygen evolution peaks (ep1) (Figure 4.12a). It can be seen that the currents in ORR and OER process are all higher than PCW based Li-O₂ battery, which indicates better electrochemical activity. However, the current in oxygen reduction process still decays very faster during cycling. The onset potential for rGO in ORR process is 2.73 V and in OER process is 3.03 V (Figure 4.12). Compared to PCW, the onset potential of rGO in ORR process increases 0.07 V, which also indicates rGO possesses better catalytic activity in electro-catalysis.

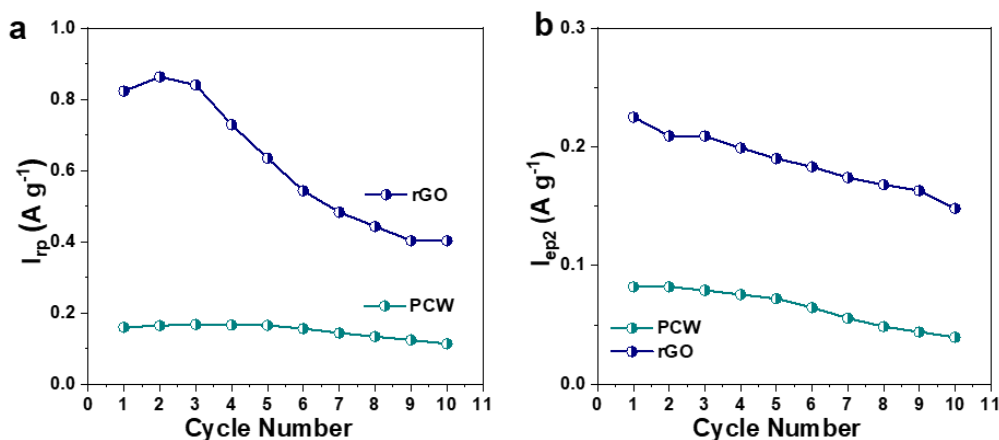


Figure 4.13. (a) The maximum absolute oxygen reduction current value vs. cycle number for PCW and rGO based batteries (b) The maximum absolute oxygen evolution value (peak ep1) vs. cycle number for PCW and rGO based batteries;

4. Results and discussion

In order to further compare the electrochemical activity of PCW and rGO based Li-O₂ batteries, the maximum absolute oxygen reduction/evolution current values vs. cycle number for PCW and rGO based batteries were studied. The maximum absolute oxygen reduction/evolution current value for rGO is much higher than PCW during the 10 cycles as shown in Figure 4.13, which indicates higher electrochemical activity of rGO as oxygen electrode for Li-O₂ battery.

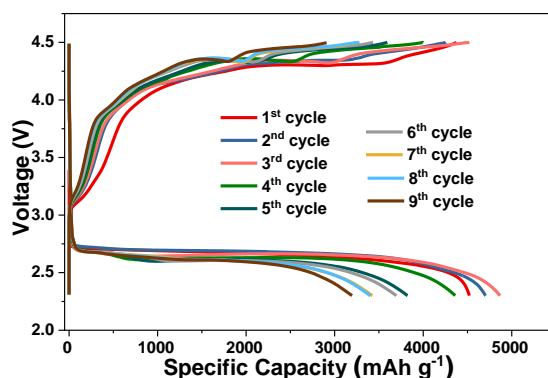


Figure 4.14. Galvanostatic discharge-charge curves of rGO based battery at a current density of 100 mA g⁻¹ between 2.3-4.5 V.

Galvanostatic discharge-charge measurements were also carried out to further clarify the electrochemical activity of rGO. The battery was cycled at a current of 100 mA g⁻¹ between 2.3-4.5 V for 9 full cycles (Figure 4.14). The rGO based battery delivers a maximum discharge capacity of 4866 mAh g⁻¹, and the discharge capacity is 3200 mAh g⁻¹ at the ninth cycle. Compared to PCW based Li-O₂ battery, the rGO based battery presents higher discharge capacity (4866 mAh g⁻¹ vs. 1216 mAh g⁻¹) and better capacity retention ability (66% vs. 37%).

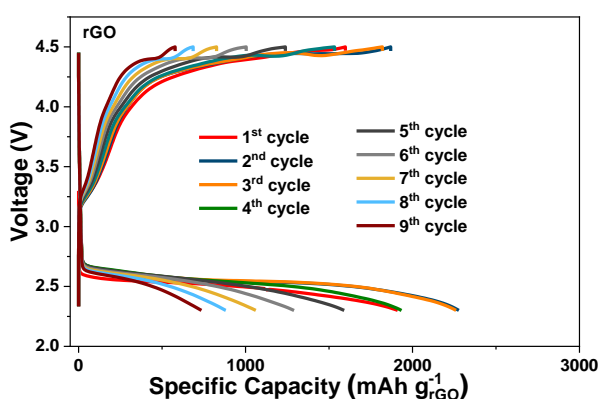


Figure 4.15. Galvanostatic discharge-charge curves of rGO based battery at a current density of 250 mA g⁻¹ between 2.3-4.5 V.

rGO based Li-O₂ battery was cycled at a higher current of 250 mA g⁻¹ (2.3-4.5 V) to explore the rate ability of rGO based Li-O₂ battery. rGO based cell can only deliver an initial discharge

4. Results and discussion

capacity of 1911 mAh g^{-1} at the current density of 250 mA g^{-1} , and the capacity is 736 mAh g^{-1} after nine cycles (38 % of the initial capacity) (Figure 4.15). This result indicates the poor electrochemical activity of rGO in high current density. The mass loading of rGO is $\sim 0.4 \text{ mg}$. I calculated the influence of carbon cloth to the total capacity of rGO based battery regardless the little difference in current density. For the initial cycle, carbon cloth devotes about 375 mAh g^{-1} capacity to rGO based battery. For the 9th cycle, the capacity devoting is $\sim 150 \text{ mAh g}^{-1}$. Compared to the total capacity of rGO based battery, carbon cloth contributes not too much capacity to the total capacity of rGO based battery.

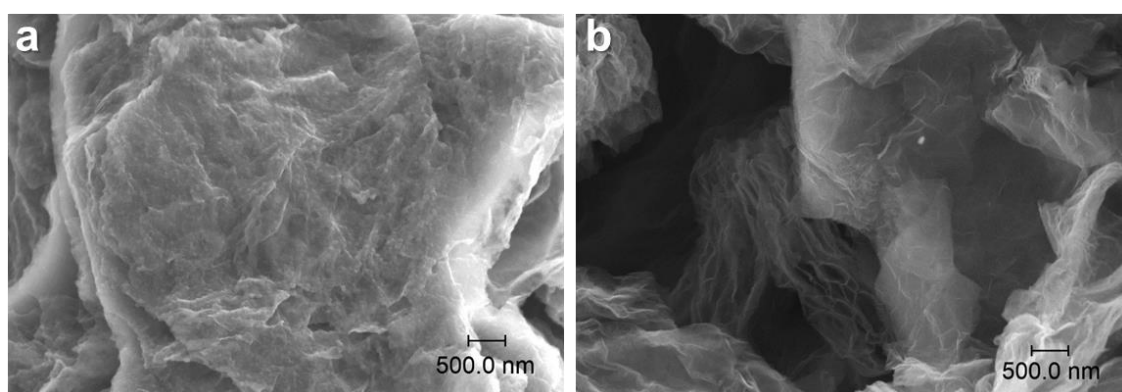


Figure 4.16. SEM images of the discharged (a) and charged (b) rGO electrodes.

SEM was applied to investigate the morphology of the discharge. The discharge products of rGO based battery present as a film, which covers the electrode surface (Figure 4.16a). This film will obstruct the free transportation of electrolyte, oxygen, and electrons during cycling, which will lead to poor capacity retention. The discharge products disappear after charged to 4.5 V (Figure 4.16b), which demonstrates the decomposition of discharge products in charge process.

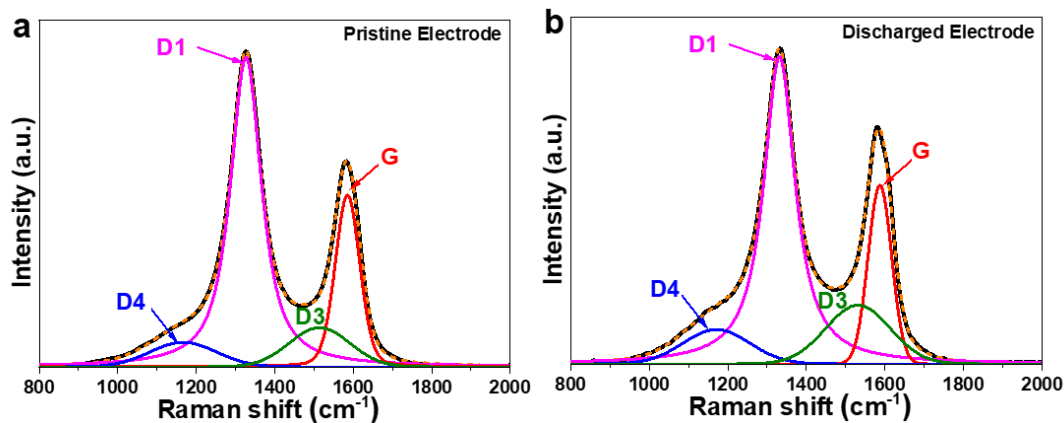


Figure 4.17. Deconvoluted Raman spectrum of the pristine (a) and discharged rGO electrodes (b).

4. Results and discussion

To further study the rGO structure evolution in ORR process, Raman spectra was applied. The Raman spectra in the range of 800-2000 cm^{-1} was deconvoluted into four component bands (D1, D3, D4 and G) (Figure 4.17). I_G/I_D and I_{D3}/I_T values for pristine rGO electrode are 0.35, 0.11. After the discharge process, I_G/I_D and I_{D3}/I_T values are 0.30 and 0.16. I_{D3}/I_T value of rGO electrode also increase obviously like PCW electrode (from 0.11 to 0.16) in the discharge process (Table 1). This means the amount of fragments or functional groups in the amorphous phase also increase obviously. However, I_G/I_D value of rGO electrode decreases much less than PCW electrode (0.05 vs. 0.23) in the discharge process, which indicates less damage of carbon structure. This is beneficial for long term cycling.

Table 1. The comparison of I_G/I_D and I_{D3}/I_T values for PCW and rGO based Li-O₂ battery before and after discharge.

Sample	I_G/I_D pristine	I_{D3}/I_T pristine	I_G/I_D discharged	I_{D3}/I_T discharged
PCW	0.40	0.24	0.17	0.28
rGO	0.35	0.11	0.30	0.16

4.2 Improvements of electrochemical performance by solid catalysts

4.2.1 MnO₂ as solid cathode catalyst for Li-O₂ batteries

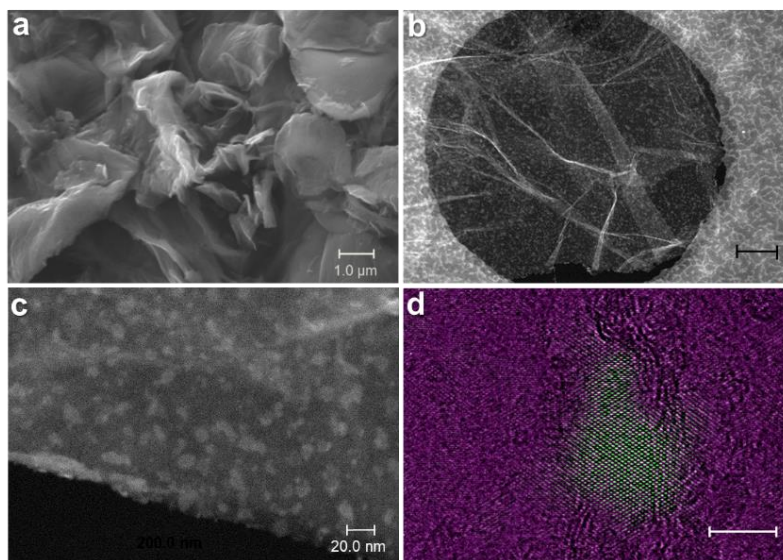


Figure 4.18. SEM images of raw MnO₂@rGO composite (a); (b) and (c) STEM images of MnO₂@rGO; (d) Composed HRTEM image from the inverse FFT of MnO₂@rGO catalyst.

4. Results and discussion

In order to improve the catalytic activity of pure rGO as the cathode for Li-O₂ batteries, MnO₂@rGO composite was synthesized. The obtained MnO₂@rGO sample was analyzed by SEM to investigate the morphology. SEM of the templated rGO sample clearly shows 3D multilayer structure. After MnO₂ deposition, this 3D multilayer structure is preserved (Figure 4.18a), assuring a high surface area to hold the discharge products. To determine the morphology, the distribution and crystal structure of the MnO₂ particles, STEM and high resolution TEM analyses were carried out. The MnO₂ nanoparticles with diameters smaller than 20 nm are uniformly dispersed on the surface of rGO (Figure 4.18b and c). To shed more light on the MnO₂@rGO composite, STEM-EDX elemental mapping (Manganese, Oxygen and Carbon) were carried out and the results are shown in Figure 4.19. The uniform distribution of manganese element again indicates that MnO₂ particles are uniformly dispersed on the surface of the rGO. The HRTEM imaging presented in Figure 4.18d further confirms that nano-sized crystalline MnO₂ particles are grown on rGO. In the synthesis process, rGO provides reactive sites for MnO₂ formation and it will partially consume by the chemical reaction with KMnO₄. Since the rGO template constrains MnO₂ growth rate, the aggregation of MnO₂ nanoparticles is avoided. Further the low KMnO₄ concentration of the solution leads to the low amount of MnO₂ deposited on the rGO surface. All these factors promote the formation of unique structure of the MnO₂@rGO composite, which nano-sized MnO₂ particles (smaller than 20 nm) were uniformly loaded on rGO surface.

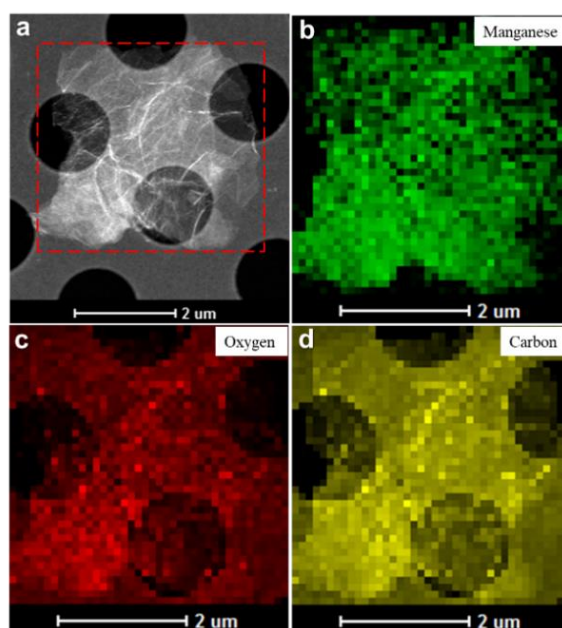


Figure 4.19. STEM and the corresponding elemental mapping images for Manganese, Oxygen and Carbon of the MnO₂@rGO composite.

4. Results and discussion

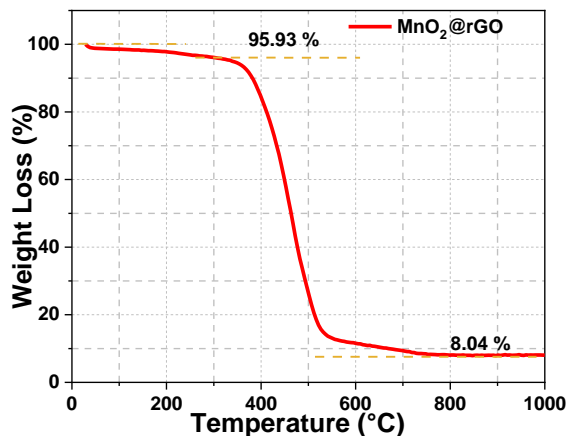


Figure 4.20. TG curve of MnO₂@rGO composite.

TG measurement was used to examine MnO₂ content of the MnO₂@rGO composite (Figure 4.20). A slight weight loss of about 4.03 wt%, which occurs below 300 °C, is ascribed to the removal of adsorbed water and crystalline water. The followed weight loss is caused by the oxidation of rGO into CO₂ and the decomposition of MnO₂ into Mn₂O₃. Based on the residual mass of Mn₂O₃, the mass percentages of MnO₂ in MnO₂@rGO composite was estimated to be 8.85 wt%. [100]

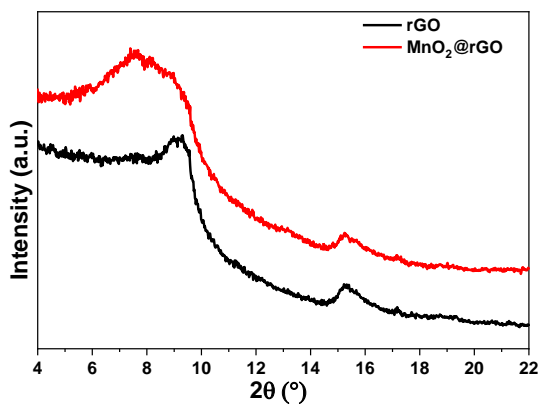


Figure 4.21. (a) XRD ($\lambda=0.559407\text{\AA}$) patterns of rGO and MnO₂@rGO.

XRD measurements were carried out to characterize the crystallinity and phase purity of the sample. Both rGO and MnO₂@rGO samples possess two broad diffraction reflections (9.2° and 15.3°) in XRD patterns (Figure 4.21). The d-spacing of the first diffraction corresponds to that of the (002) reflection in graphite and therefore most likely originates from small domains of stacked rGO sheets. The first diffraction position yields a mean inter graphene spacing of 0.35 nm, which is substantially larger than that of graphite ($c/2 = 0.3354$ nm). The XRD pattern of MnO₂@rGO shows a broad and weak diffraction peak at about 7.6°, which corresponds to the characteristic (101) crystal plane of MnO₂ (JCPDS Number: 39-0375). The weak and broad peak can be ascribed

4. Results and discussion

to the low MnO₂ content of the MnO₂@rGO composite and the small particle size (smaller than 20 nm).

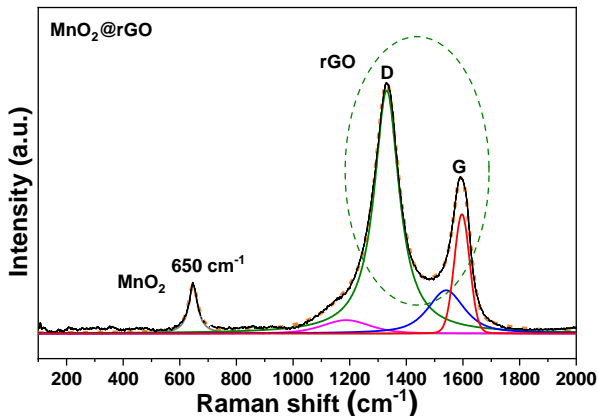


Figure 4.22. Raman spectra of MnO₂@rGO.

Raman spectroscopy analysis was applied to further investigate the structural evolution of the MnO₂@rGO sample (Figure 4.22). Raman spectra of MnO₂@rGO specimen have the typical bands of carbon materials, which are located at 1335 cm⁻¹ (D-band) and 1592 cm⁻¹ (G-band).[96] The two peaks are composed of four bands: D1, D3, D4 and G. As we talked above, the G-band is assigned to the E_{2g} phonon of sp²-bonded carbon atoms, which is the characteristic feature of graphitic layers.[97],[98] The D1-band is assigned to the breathing mode of κ-point phonons with A_{1g} symmetry, which corresponds to disordered carbon or defective graphitic structures.[97],[98] The D3 peak shows the existence of fragments or functional groups in the amorphous phase, which may also change the C–C and C=C stretching vibrations of the polyene-like structure (D4).[37] The area ratio of G band and D1 band (named as I_G/I_D) is generally used as an indicator for the graphitization degree of carbon materials. The I_G/I_D value is 0.30 for MnO₂@rGO. This indicates that MnO₂@rGO possesses lower graphitization degree compared to rGO. In addition to the G-band and D-band, MnO₂@rGO sample also presents a distinct band at around 650 cm⁻¹, which corresponds to the symmetric stretching vibration M–O of [MnO₆] groups.[101]

XPS analysis was applied to determine the oxidation state and elemental composition of the prepared MnO₂@rGO. The high-resolution Mn 3s spectrum shows two peaks with a separation of 5.2 eV due to spin-orbit splitting (Figure 1.1a). This value lies between the spin-orbit splitting for Mn⁴⁺ and Mn³⁺ of 4.6 and 5.5 eV, respectively. This indicates the presence of these both oxidation states. The high-resolution Mn 2p_{3/2} spectrum was further explored to confirm this conclusion (Figure 1.1b). The absence of a shake-up satellite, which is typical for Mn²⁺ at ~ 646 eV, confirms

4. Results and discussion

the absence of Mn^{2+} in the sample. The multiplet fitting approach of Biesinger et al. was applied here and adapted as in the work of Azmi et al.[102],[103] Two multiplet could be observed, which confirms the presence of both oxidation state of Mn^{4+} and Mn^{3+} species with a slightly higher concentration of Mn^{3+} ($\text{Mn}^{3+}:\text{Mn}^{4+} = 3:2$).

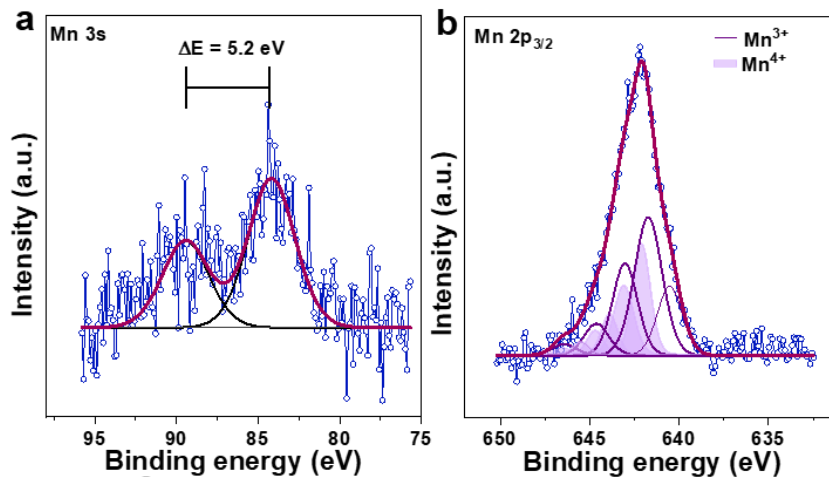


Figure 4.23. (a) and (b) the high-resolution XPS spectrum of the Mn 3s and Mn 2p_{3/2} for MnO₂@rGO;

Since the testing depth for XPS is only a few nanometers in the surface, we employ XANES spectroscopy to obtain more detailed information about the electronic structure of the bulk. Mn K-edge position of the MnO₂@rGO composite overlaps with that of standard MnO₂ from XANES result (Figure 4.24), which indicates that the oxidation state of Mn in the composite is mainly Mn^{4+} . It can be concluded from the surface oxidation state information of XPS and bulk oxidation state of XANES that Mn^{3+} and hence oxygen vacancies are mostly enriched on the MnO₂ particle surface.

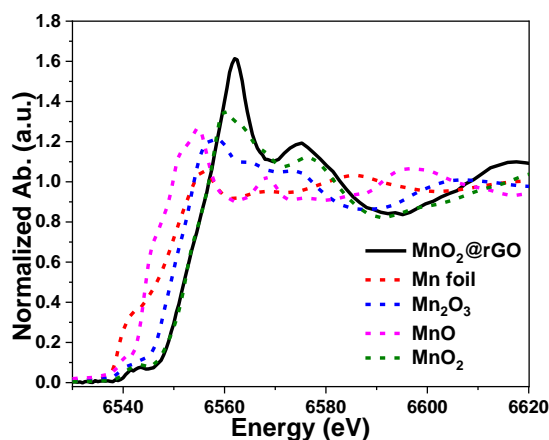


Figure 4.24. Normalized Mn K-edge XANES spectra of the obtained MnO₂@rGO materials together with reference spectra of Mn foil, MnO, Mn₂O₃ and MnO₂.

4. Results and discussion

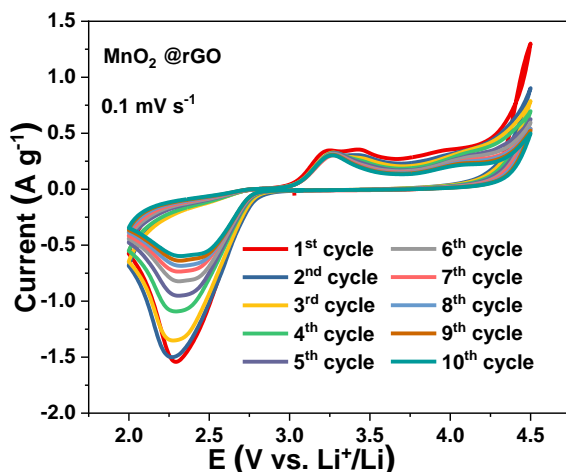


Figure 4.25. CV curves of the beginning 10 cycles for $\text{MnO}_2@\text{rGO}$ based battery at a scan rate of 0.1 mV s^{-1} between 2.0-4.5 V.

The catalytic activity of $\text{MnO}_2@\text{rGO}$ material was investigated by cyclic voltammetry (CV) in the voltage of 2.0 - 4.5 V. The CV curves of $\text{MnO}_2@\text{rGO}$ based Li- O_2 batteries at a scan rate of 0.1 mV s^{-1} are shown in Figure 4.25. It can be clearly concluded that the current for $\text{MnO}_2@\text{rGO}$ based Li- O_2 battery is higher than rGO based Li- O_2 battery. This conclusion further verifies the high efficient catalytic effect caused by the nano-sized MnO_2 loaded on rGO surface.

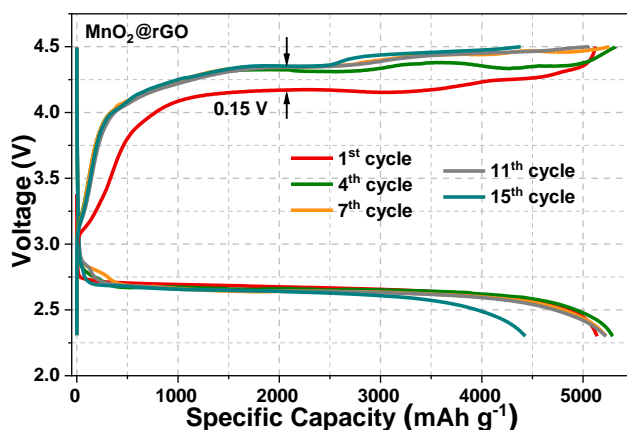


Figure 4.26. Galvanostatic discharge-charge curves of $\text{MnO}_2@\text{rGO}$ based battery at a current density of 100 mA g^{-1} between 2.3-4.5 V;

Galvanostatic discharge-charge measurements were carried out to clarify the catalytic effect of $\text{MnO}_2@\text{rGO}$ composite. $\text{MnO}_2@\text{rGO}$ based batteries were operated in a voltage range of 2.3-4.5 V vs. Li^+/Li at a current of 100 mA g^{-1} for 15 full cycles (Figure 4.26). $\text{MnO}_2@\text{rGO}$ based battery exhibits very good reversibility with almost no capacity decay within the initial 11 cycles. The charging voltage of the $\text{MnO}_2@\text{rGO}$ based battery increases by about 0.15 V from the first to the

4. Results and discussion

fourth cycle. Then it stays stable for the following 11 cycles. Charge voltage of MnO₂@rGO based battery increases 0.15 V since the first to the fourth cycle, then it keeps stable in the following 11 cycles. In contrast, rGO based battery shows poor capacity retention with a continuous decay from the first cycle. The charging voltage of the rGO based battery continues to increase from the first to the fifteenth cycle.

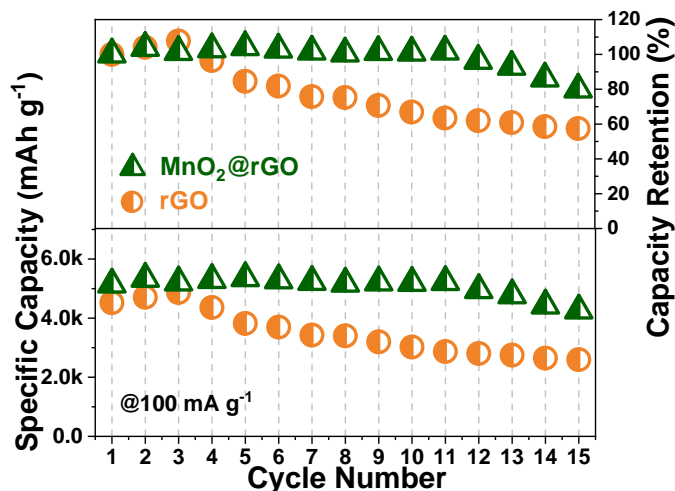


Figure 4.27. Variation of discharge capacity and capacity retention with cycle number for MnO₂@rGO and rGO based batteries.

MnO₂@rGO based battery delivers an initial discharge capacity of 5139 mAh g⁻¹. Even after the fifteenth cycle a discharge capacity of 4262 mAh g⁻¹ is still obtained (Figure 4.27). Discharge capacity decays very less during the 15 cycles, and it can keep 80% of initial capacity after 15 cycles. The mass loading of MnO₂@rGO is ~0.6 mg. I also calculated the influence of carbon cloth to the total capacity of MnO₂@rGO based battery regardless the little difference in current density. For the initial cycle, carbon cloth devotes about 250 mAh g⁻¹ capacity to MnO₂@rGO based battery. For the 9th cycle, the capacity devoting is around 100 mAh g⁻¹. Compared to the total capacity of MnO₂@rGO based battery, carbon cloth also contributes very less capacity to the total capacity of MnO₂@rGO based battery. So my capacity comparison analysis did not consider the influence of carbon cloth. The pure rGO based battery presents a maximum discharge capacity of 4866 mAh g⁻¹ and a discharge capacity of 2597 mAh g⁻¹ (53% capacity retention) after 15 cycles (Figure 4.27). This value is much lower than the capacity retention of the MnO₂@rGO based battery. This demonstrates that the MnO₂ nanoparticles effectively support the OER and hence restrain the accumulation of discharge products at the electrode surface.

The voltage profiles during the first discharge-charge of the rGO and MnO₂@rGO based Li-O₂

4. Results and discussion

batteries are displayed in Figure 4.28. The MnO₂@rGO based Li-O₂ battery shows a 0.2 V lower charge voltage compared to rGO based battery. Hence, the lower charge voltage can be attributed to the catalytic effect of MnO₂ for the OER process.[69],[104] The good catalytic activity of the MnO₂ particles may be attributed to their small particle size and high number of oxygen vacancies at their surface.

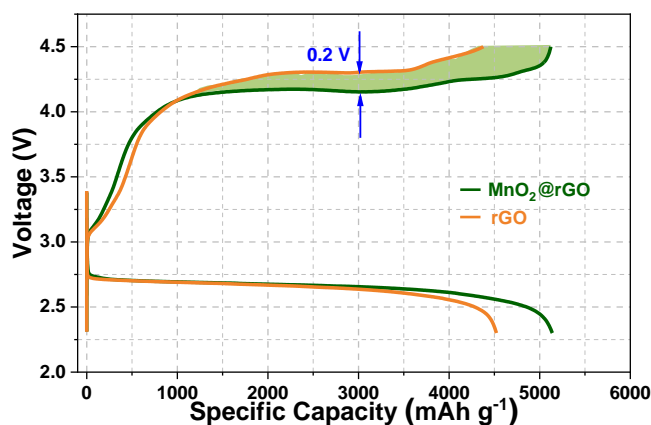


Figure 4.28. Comparison of initial discharge-charge profiles of MnO₂@rGO and rGO based batteries.

In order to study the influence of trace water on the electrochemical performance, the Li-O₂ battery was cycled at a current density of 100 mA g⁻¹ without water in the system. It can be concluded that the lack of trace water leads to a decrease of discharge capacity (Figure 4.29). Meanwhile, the discharge voltage plateau is also slightly decreased. This is because water is a strong Lewis acid and increases the solubility of LiO₂ in the electrolyte solution.³¹ Therefore, the surface mechanism for the formation of discharge products is converted into a solution based mechanism.³¹

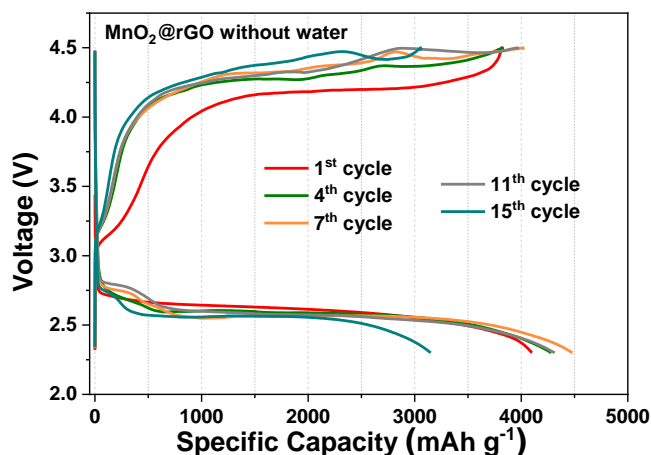


Figure 4.29. Galvanostatic discharge-charge curves of MnO₂@rGO cycled without water at a current density of 100 mA g⁻¹ between 2.3-4.5 V.

4. Results and discussion

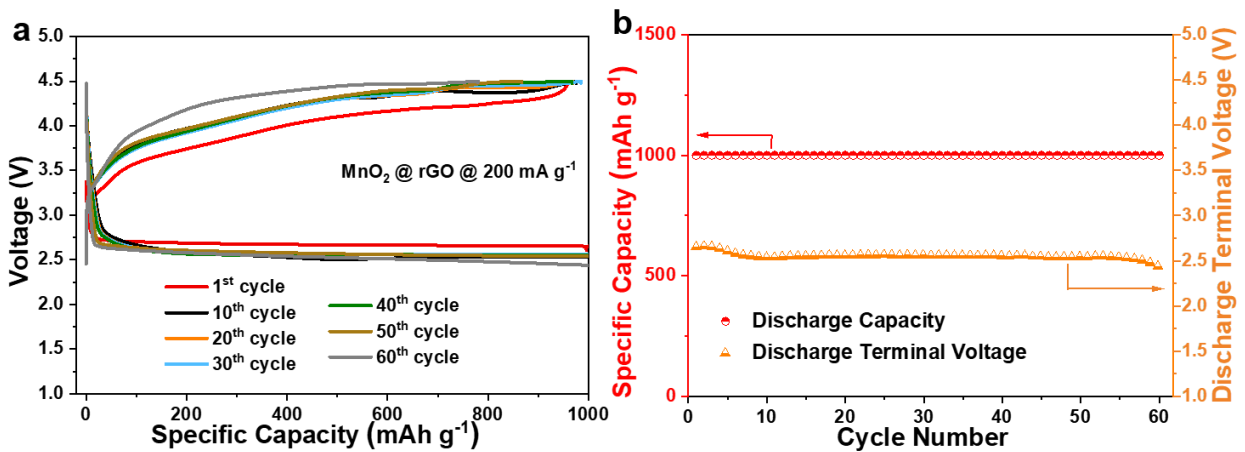


Figure 4.30. (a) Charge and discharge profiles of MnO₂@rGO battery at the 1st, 10th, 20th, 30th, 40th, 50th and 60th cycles with a specific capacity limit of 1000 mAh g⁻¹ at a current density of 200 mA g⁻¹ between 2.3-4.5 V. (b) Discharge/charge capacity and terminal voltage vs. cycle number at a current density of 200 mA g⁻¹.

The cycling stability of the MnO₂@rGO based battery was further explored by galvanostatic cycling at a current density of 200 mA g⁻¹ and a cut-off capacity of 1000 mAh g⁻¹. Batteries based on MnO₂@rGO showed a constant discharge capacity over 60 cycles (Figure 4.30a). During the first seven cycles the discharge end voltage decays slightly from 2.65 V to 2.55 V and then keeps stable at 2.55 V until the 60th cycle (Figure 4.30b).

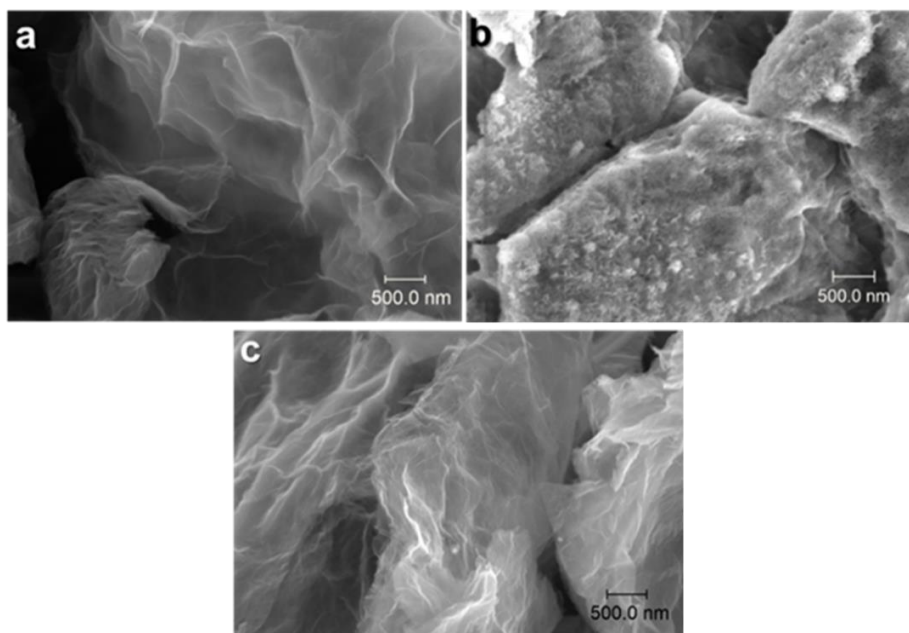


Figure 4.31. SEM images of pristine MnO₂@rGO electrode (a), after full discharge to 2.3 V (b), and after recharge to 4.5 V (c);

The morphologies of the discharge products were determined by SEM. SEM images of the pristine

4. Results and discussion

MnO₂@rGO electrode, after the first discharge to 2.3 V and after recharge to 4.5 V are shown in Figure 4.31. After discharge to 2.3 V, the porous multilayer structure of the MnO₂@rGO electrode is covered with a fine grained mossy deposition product (Figure 4.31b). After recharging to 4.5 V, the discharge products disappear and the original multilayer porous structure of MnO₂@rGO becomes visible again (Figure 4.31c). In contrast, the discharge products on the pure rGO electrode form a smooth film, which covers the electrode surface. This film possibly obstructs the free transportation of electrolyte, oxygen, and electrons, leading to the reduced capacity of pure rGO. Based on these SEM results, we conclude that the mass transport of LiO₂ species is enhanced by MnO₂. This enhancement may be attributed to the weakening of bindings between the intermediate (LiO₂ species) and substrate by MnO₂. [105],[30] Moreover, the large exposed surface of the MnO₂ nano-particles will lead to a higher interfacial current density, which reduces the reaction time to form discharged products. The enhancement of surface transport and the reduction of reaction time synergistically act together and lead to the formation of a fine grained and uniform discharge product. [105],[30]

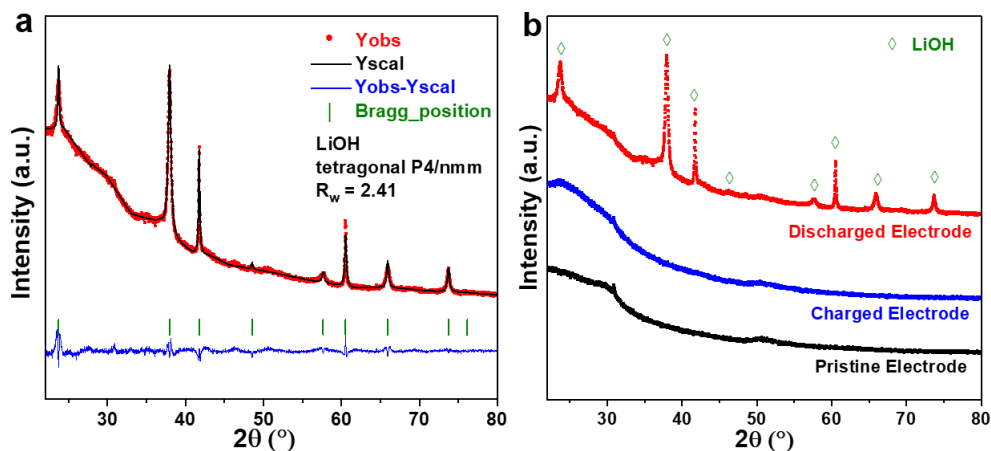


Figure 4.32. Rietveld refinement of the proposed LiOH structure model based on the XRD ($\lambda=1.78896 \text{ \AA}$) of discharged MnO₂@rGO electrode (a), XRD patterns of pristine MnO₂@rGO electrode, after discharge to 2.3 V and recharge to 4.5 V (b).

To identify crystalline discharge products, XRD with Co radiation was applied. The XRD pattern clearly demonstrates that peaks corresponding to LiOH emerge after the discharge process (Figure 4.32b). These peaks completely disappear in the subsequent charge process (Figure 4.32b), which indicates a complete decomposition of LiOH. Furthermore, the phase purity of the discharge products was studied by Rietveld refinement. Figure 4.32a confirms that the main reflections are in good agreement with the tetragonal phase of LiOH (space group: P4/nmm (129)). Satisfactory agreement factors ($R_{wp} = 2.4\%$, $R_p = 1.7\%$) with the cell parameter $a = b = 3.5487(1) \text{ \AA}$, $c =$

4. Results and discussion

4.3511(1) Å, $\alpha = \beta = \gamma = 90^\circ$, and cell volume = 54.795(3) Å³ are determined in this crystal refinement.

To further elucidate the nature of the discharge products, Raman measurements were carried out. The pristine electrode shows only the characteristic bands of rGO and MnO₂. Li-O₂ battery was fully discharged to 2.3 V, and then the MnO₂@rGO electrode after discharge was characterized by Raman. After discharge to 2.3 V the appearance of new bands indicate the formation of discharge products (Figure 4.33a). These bands disappear again after charge (Figure 4.33a), indicating a reversible and almost complete decomposition of the discharge products. Most changes in the Raman spectrum of the discharged electrode occur in the range between 300 to 750 cm⁻¹. Despite some overlap, seven different bands labeled A, B, C, D, E, F and G can be distinguished in the enlarged view of this region (Figure 4.33b). The frequencies of the six bands labeled as B, C, D, E, F and G in Figure 4.33b are located at about 407, 431, 501, 566, 610 and 650 cm⁻¹, which agrees well with the vibrational bands of Li₂MnO₃. [106],[107] Given the rather strong intensity of the Li₂MnO₃ bands if compared to the pristine sample and the small size of the original MnO₂ particles, it seems most likely that MnO₂ transforms into a lithiated manganese oxide during discharge. The Raman spectrum of the charged electrode reveals that this lithiated manganese oxide is transformed back into MnO₂ again during charge. This transition between lithiated and non-lithiated manganese oxide may therefore at least be partially responsible for the catalytic activity of MnO₂ in Li-O₂ batteries by reducing the electron transfer resistance and O₂ desorption energy. [108] The discharged electrode also shows another prominent band (labeled as A) at 320 cm⁻¹ which can be attributed to LiOH vibration from our experiment (Figure 4.33b).

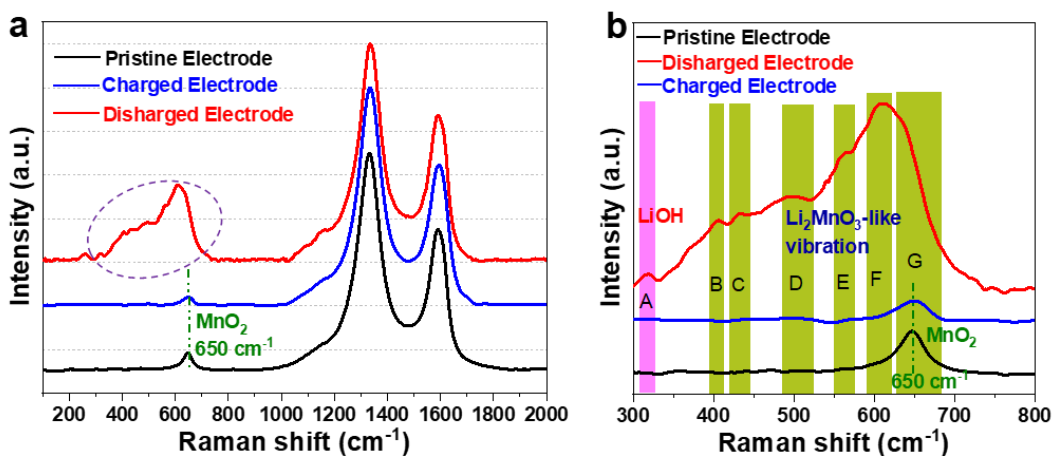


Figure 4.33. Raman spectra of pristine MnO₂@rGO electrode, after discharge to 2.3 V and recharge to 4.5 V (a). (b) Raman spectra in the range of 800-2000 cm⁻¹ for pristine, discharged and charged MnO₂@rGO electrodes.

4. Results and discussion

To study changes of the rGO during the discharge and charge process the Raman spectra in the range between 800-2000 cm^{-1} were deconvoluted into four component bands (D1, D3, D4 and G) (Figure 4.34). As we talked above, Raman spectra originated from rGO exhibits two distinct peaks located at 1335 cm^{-1} (D-bands) and 1592 cm^{-1} (G-bands). I_G/I_D values are 0.30, 0.29 and 0.29 for pristine, discharged and charged $\text{MnO}_2@\text{rGO}$ electrodes, which means the graphitization degree decrease very less in the discharge and charge process. While I_G/I_D values of pristine, discharged and charged rGO electrodes are 0.35, 0.30 and 0.29. Moreover, I_{D3}/I_T values for both rGO and $\text{MnO}_2@\text{rGO}$ electrodes increase after discharge (Figure 4.34d). This indicates an increase of fragments or functional groups in the amorphous phase, which is ascribed to the side reactions during battery cycling with the electrolyte or the rGO itself. It can be seen that I_{D3}/I_T value of rGO electrode increases much more than that of the $\text{MnO}_2@\text{rGO}$ electrode, indicating more side reactions for the rGO electrode. After charge, the I_{D3}/I_T value of $\text{MnO}_2@\text{rGO}$ electrode decreases back to 0.12, which indicates an almost complete removal of side products from electrode surface. In contrast, the I_{D3}/I_T value of rGO electrode after charge (0.14) stays elevated compared to its initial value (0.11). This suggests an incomplete removal of side products in case of the rGO electrode, which will result in a gradual accumulation of side products on the oxygen electrode and early cell death.

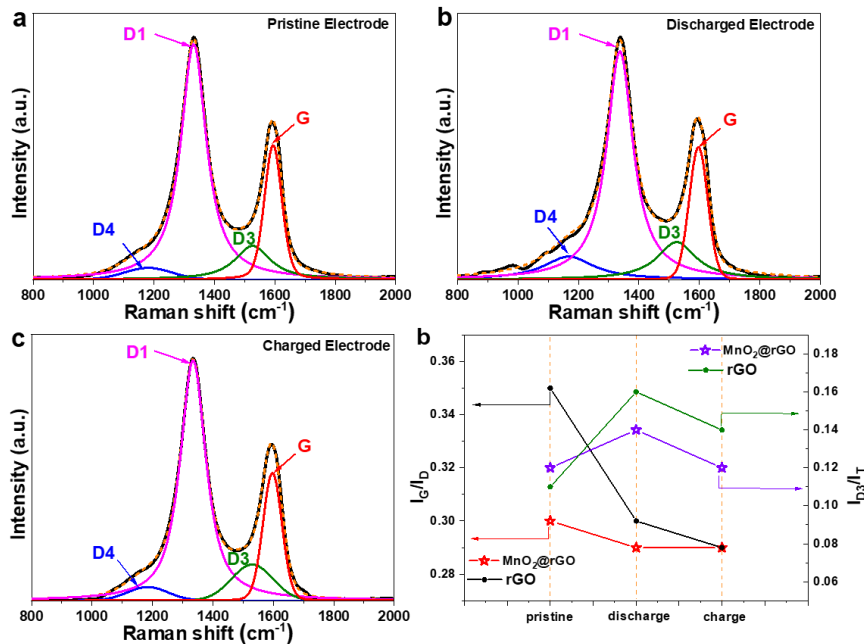


Figure 4.34. Deconvoluted Raman spectrum of the pristine $\text{MnO}_2@\text{rGO}$ electrode (a), after discharge to 2.3 V (b) and recharge to 4.5 V (c). Comparison of I_G/I_D value and I_{D3}/I_T value for the pristine $\text{MnO}_2@\text{rGO}$ electrode, after discharge to 2.3 V and recharge to 4.5 V (d).

4. Results and discussion

4.2.2 Co_3O_4 as solid cathode catalyst for Li- O_2 batteries

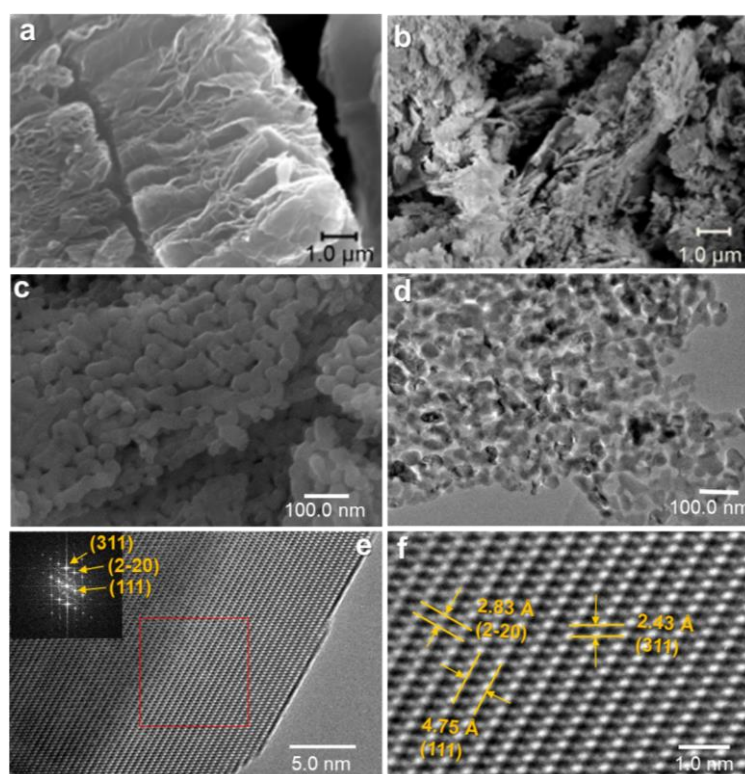


Figure 4.35. SEM images of raw rGO (a) and Co_3O_4 (b); (c) High Resolution SEM image of Co_3O_4 ; (d) TEM image of Co_3O_4 ; (e) and (f) HRTEM images of Co_3O_4 , the insert is the fast-Fourier-transform (FFT) image.

Co_3O_4 nanoparticles were also synthesized and applied as solid cathode catalyst for Li- O_2 battery. In order to investigate the morphology and microstructure of the as-prepared Co_3O_4 material, SEM was applied. The rGO with a 3D nanoplate structure can serve as a template for the synthesis process of Co_3O_4 (Figure 4.35a). The as-prepared Co_3O_4 also exhibits a nanoplate structure with (Figure 4.35b). Moreover, the Co_3O_4 nanoplates are formed of closely aggregated Co_3O_4 particles with a diameter of dozens of nanometers (Figure 4.35c). The detailed morphology and crystal structure of Co_3O_4 was further investigated by (HR)TEM. The TEM image in Figure 4.35d again demonstrates that Co_3O_4 nanoplates are formed of closely aggregated nano-sized Co_3O_4 particles. Moreover, the Co_3O_4 material presents well-crystallized nanostructures (Figure 4.35e and f). In the HRTEM images, d -spacings of 0.475 nm, 0.283 nm and 0.243 nm are observed. The angle between the d -spacing of 0.475 nm and 0.283 nm is 90° , and the angle between the d -spacing of 0.475 nm and 0.243 nm is 30° . These values are in good agreement with the lattice spacing of the (111), (2-20), and (311) crystal planes along the [112] zone axis of face-centered cubic (fcc) Co_3O_4 , which can be further evidenced by the FFT spot patterns.[109]

4. Results and discussion

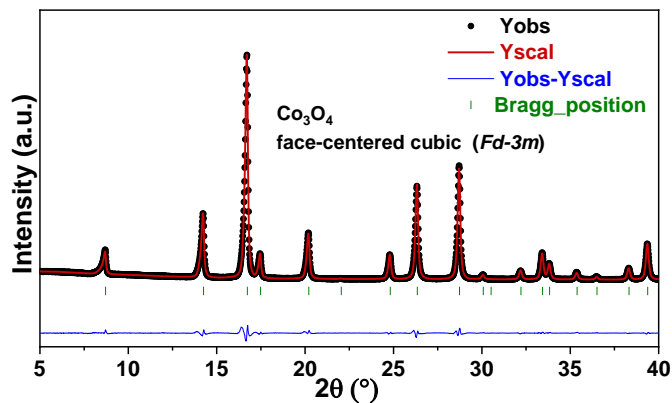


Figure 4.36. Rietveld refinement of the Co_3O_4 structure model and the experimental XRD pattern ($\lambda=0.70932 \text{ \AA}$) for Co_3O_4 .

A more detailed analysis of the crystal structure of the as-prepared Co_3O_4 was carried out by XRD with Mo K alpha radiation ($\lambda=0.70932 \text{ \AA}$, Figure 4.36). All the reflections could be indexed by a face-centered cubic Co_3O_4 structure model with the space group $Fd-3m$. The structure model of Co_3O_4 was refined by the Rietveld method, for a precise determination of lattice parameters. The lattice parameters determined by Rietveld were $a = b = c = 8.0854(1) \text{ \AA}$ and $\alpha = \beta = \gamma = 90^\circ$ (Bragg R-factor=0.85, Rf-factor=0.67).

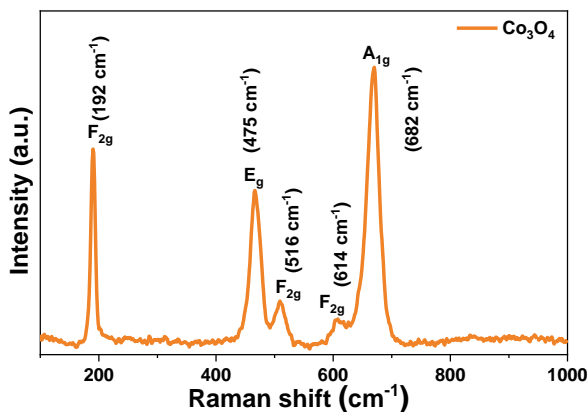


Figure 4.37. Raman spectra of Co_3O_4 .

To analyze the local structure of Co_3O_4 Raman spectroscopy was applied. The Co_3O_4 spinel structure possesses five Raman-active modes: A_{1g} , E_g , and three F_{2g} modes.[110] The Raman spectra of the porous Co_3O_4 shows two peaks at 466 and 670 cm^{-1} , which can be attributed to the E_g and A_{1g} mode of Co_3O_4 (Figure 4.37). The remaining three peaks at 191, 511 and 607 cm^{-1} can be ascribed to the F_{2g} modes of crystalline Co_3O_4 (Figure 4.37). All characteristic peaks are in good agreement with the peak positions known from literatures, except for some small shifts. The

4. Results and discussion

A_{1g} mode is assigned to the symmetric stretching of the Co-O bond at tetrahedral sites referred to as the tetrahedral breathing mode.[111]

The surface oxidation states of Co_3O_4 nanoplates were analyzed by XPS analysis. The XPS spectrum of Co_3O_4 shows signals from cobalt and oxygen, as expected. Figure 4.38 exhibits the high-resolution Co 2p XPS spectrum, which presents a main peak at 779.0 eV accompanied by a multiplet structure similar to the work presented by Biesinger et al.[102] Two different oxidation states can be identified, namely Co^{2+} with a satellite at ~ 786 eV and Co^{3+} with a weak satellite located at ~ 789 eV.[103] This result is in good consistent with the XRD and Raman measurement.

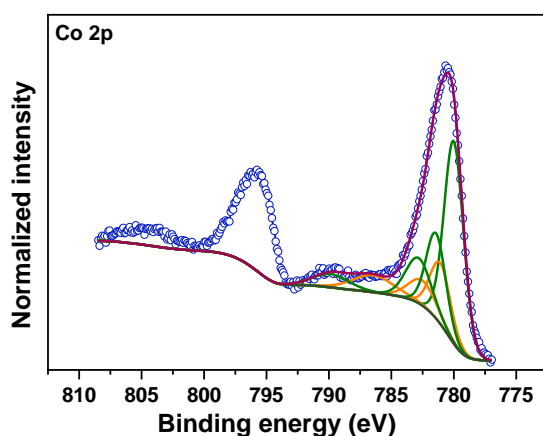


Figure 4.38. High-resolution Co 2p XPS spectrum of Co_3O_4 . Co^{2+} (orange) and Co^{3+} (green) are both present in the material.

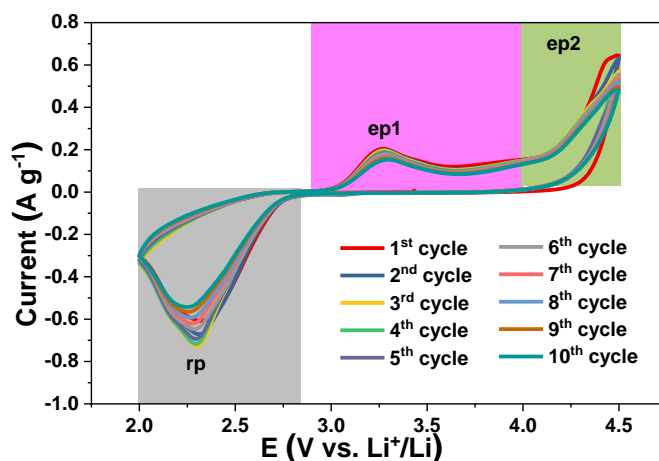


Figure 4.39. Cyclic voltammograms of the initial 10 cycles for $\text{Co}_3\text{O}_4/\text{rGO}$ based Li- O_2 battery at a scan rate of 0.1 mV s^{-1} between 2.0-4.5 V.

The electrochemical performance of the Co_3O_4 catalyst in a Li- O_2 battery was investigated by a series of electrochemical tests. Cyclic voltammograms (CVs) from 4.5 to 2.0 V were measured to explore the electro-catalytic activity of Co_3O_4 (Figure 4.39). All CV curves show one oxygen

4. Results and discussion

reduction peak (rp) and two oxygen evolution peaks (ep1 and ep2). Compared to the pure rGO (in chapter 4.1), $\text{Co}_3\text{O}_4/\text{rGO}$ exhibits a higher ep2 peak current, which indicates a higher OER catalytic activity for Li- O_2 batteries.

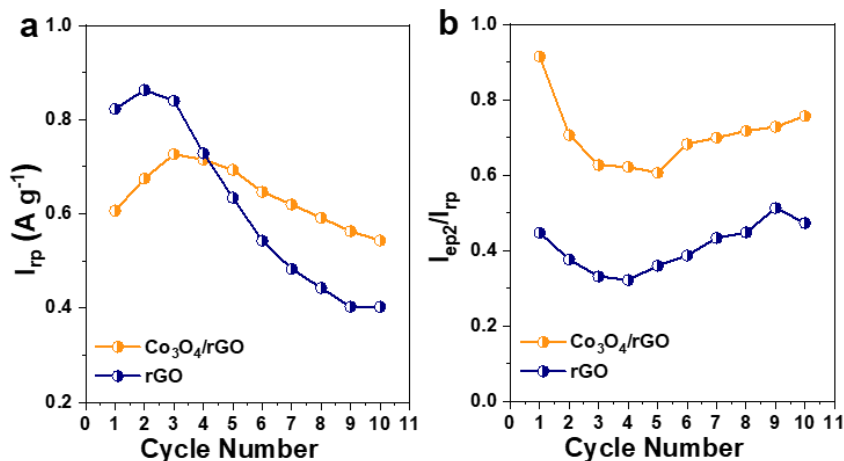


Figure 4.40. (a) Peak current of the ORR vs. cycle number for $\text{Co}_3\text{O}_4/\text{rGO}$ and rGO based batteries, (b) The current ratio of oxygen evolution peak ep2 and oxygen reduction rp (I_{ep2}/I_{rp}) vs. cycle number for $\text{Co}_3\text{O}_4/\text{rGO}$ and rGO based batteries.

The peak current of the ORR for the rGO based battery decays very fast during cycling as shown in Figure 4.40a, and reaches only about 50% of the initial value after 10 cycles. In comparison, the battery catalyzed by Co_3O_4 starts at a lower peak current, but presents a more stable development of the peak current, displaying a slight initial increase and a low attenuation to ~90% after 10 cycles. As a result, reduction peak current of the $\text{Co}_3\text{O}_4/\text{rGO}$ based battery outpaces the one with pure rGO after 5 cycles than rGO based battery. The current ratios of the oxygen evolution (ep2) and the oxygen reduction peak (rp) referred to as I_{ep2}/I_{rp} were investigated to reflect the oxygen evolution ability of batteries catalyzed by $\text{Co}_3\text{O}_4/\text{rGO}$ and rGO (Figure 4.40b). The battery with the Co_3O_4 catalyst exhibits much higher values of I_{ep2}/I_{rp} , corresponding to a higher oxygen evolution ability. Therefore, it can be concluded that the nano-sized Co_3O_4 particles efficiently catalyze the reversible reduction and oxidation reaction.

Galvanostatic discharge-charge measurements were carried out to further study the electro-catalytic activity of Co_3O_4 . The initial discharge-charge curves of $\text{Co}_3\text{O}_4/\text{rGO}$ and rGO at a current density of 250 mA g^{-1} are presented in Figure 4.41. The battery with $\text{Co}_3\text{O}_4/\text{rGO}$ delivers an initial discharge capacity of 2220 mAh g^{-1} ($5920 \text{ mAh g}_{\text{rGO}}^{-1}$), which is higher than the initial discharge capacity of pure rGO based battery (1911 mAh g^{-1}). Moreover, the Li- O_2 battery catalyzed by $\text{Co}_3\text{O}_4/\text{rGO}$ shows 143 mV higher discharge voltage and 220 mV lower charge voltage compared

4. Results and discussion

to pure rGO based battery. These two results further confirm the higher catalytic activity of $\text{Co}_3\text{O}_4/\text{rGO}$ for the reversible discharge-charge of Li-O_2 batteries.

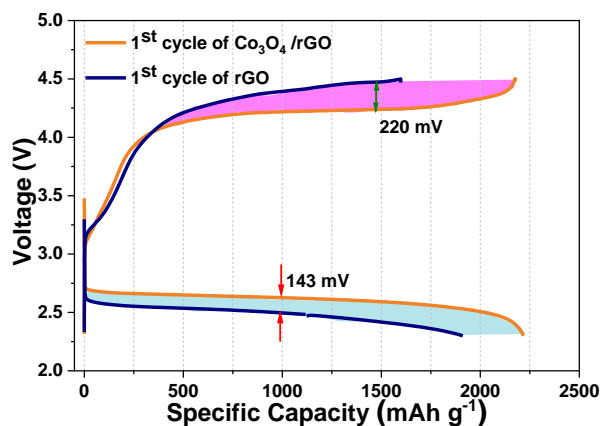


Figure 4.41. Initial discharge-charge curves of $\text{Co}_3\text{O}_4/\text{rGO}$ and rGO based batteries at a current density of 250 mA g^{-1} between 2.3-4.5 V.

To investigate the cycling stability without capacity limitation, Li-O_2 cells were cycled at a current density of 250 mA g^{-1} in the voltage range of 2.3-4.5 V for nine cycles (Figure 4.42). $\text{Co}_3\text{O}_4/\text{rGO}$ based Li-O_2 battery exhibits a maximum discharge capacity of 3625 mAh g^{-1} ($9624 \text{ mAh g}_{\text{rGO}}^{-1}$), and the capacity is still 1933 mAh g^{-1} after nine cycles. In the absence of Co_3O_4 catalysis, the rGO based cell exhibits a fast capacity decay as shown in chapter 4.1.

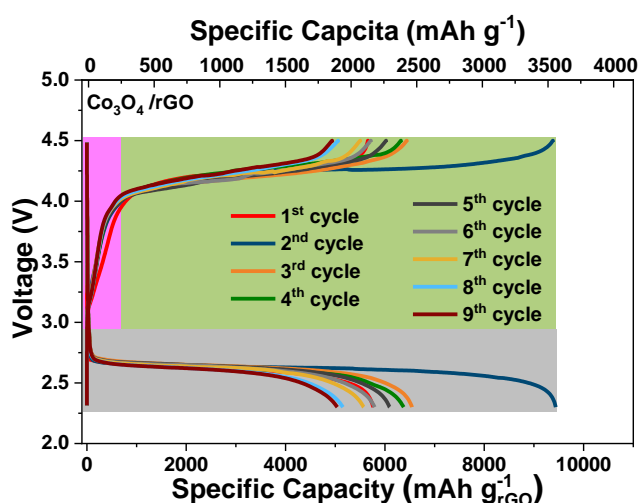


Figure 4.42. Galvanostatic discharge-charge curves of the battery catalyzed by Co_3O_4 at a current density of 250 mA g^{-1} between 2.3-4.5 V.

The variation of the discharge capacity and capacity retention in relation to the cycle number is displayed in Figure 4.43. The battery with $\text{Co}_3\text{O}_4/\text{rGO}$ delivers an initial discharge capacity of

4. Results and discussion

2220 mAh g_{total}⁻¹ and a capacity retention of 87 % (1933 mAh g_{total}⁻¹) after nine cycles. The mass loading of Co₃O₄ and rGO is ~1.4 mg. I calculated the influence of carbon cloth to the total capacity of Co₃O₄/rGO based battery regardless the little difference in current density. For the initial cycle, carbon cloth devotes about 107 mAh g⁻¹ capacity to Co₃O₄/rGO based battery. For the 9th cycle, the capacity devoting is around 43 mAh g⁻¹. Compared to the total capacity of Co₃O₄/rGO based battery, carbon cloth also contributes very less capacity to the total capacity of MnO₂@rGO based battery. So my capacity comparison analysis did not consider the influence of carbon cloth. The rGO based cell had only an initial discharge capacity of 1911 mAh g_{total}⁻¹ and capacity retention is just 38 % (738 mAh g_{total}⁻¹) after nine cycles. In summary, it could be concluded that the Co₃O₄ nanoparticles enhance the catalytic activity compared to pure rGO, reducing the voltage gap, leading to an increase of discharge capacity, and improving capacity retention.

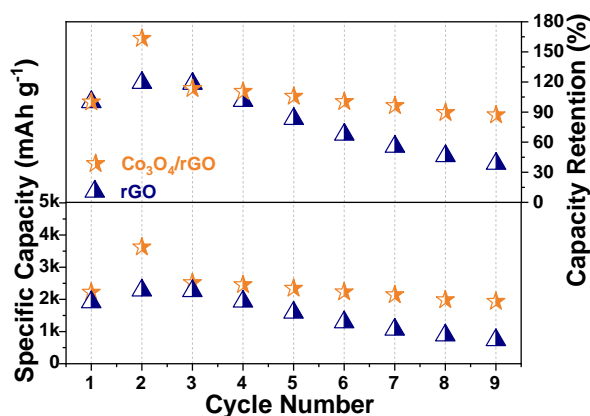


Figure 4.43. Discharge capacity and capacity retention vs. cycle number for Co₃O₄/rGO and rGO based batteries.

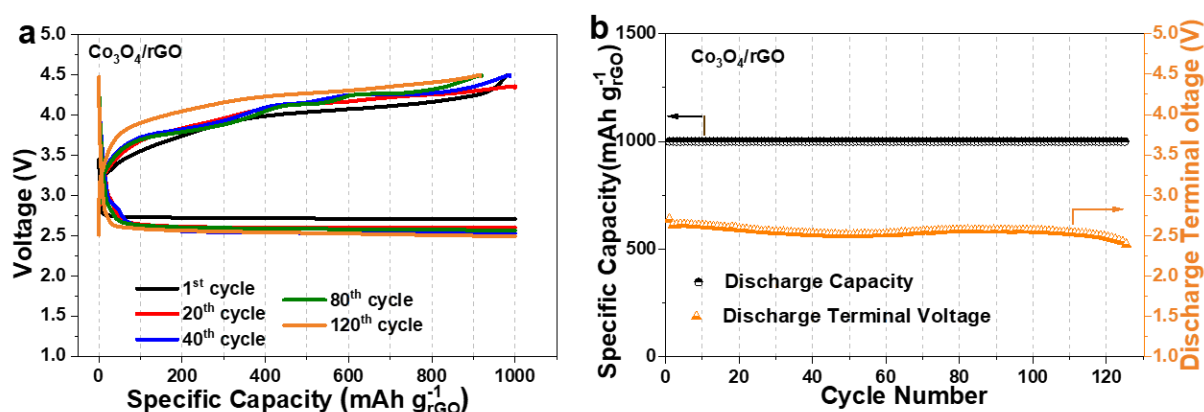


Figure 4.44. Galvanostatic discharge/charge profiles of the battery catalyzed by Co₃O₄/rGO with a cut-off capacity of 1000 mAh g⁻¹ at a current density of 250 mA g⁻¹. (b) Discharge capacity and terminal voltage vs. cycle number at a current density of 250 mA g⁻¹.

4. Results and discussion

Galvanostatic discharge/charge test with a cut-off capacity of 1000 mAh g^{-1} (avoiding deep discharge) at a current density of 250 mAh g^{-1} was applied to investigate the cyclability of $\text{Co}_3\text{O}_4/\text{rGO}$ based battery. The Li-O_2 cell was continuously discharged and charged at 250 mA g^{-1} for 125 cycles, and the selected cycles of discharge and charge profiles are shown in Figure 4.44a. The discharge and charge curves during the initial 80 are almost stable. A slight charge potential increase beyond the 80 cycles can be observed, which could be attributed to the electrolyte instability and the accumulation of discharge products during many cycles.[72] The discharge capacities and discharge terminal voltages in the 125 cycles are almost constant (Figure 4.44b), indicating its good reversibility.

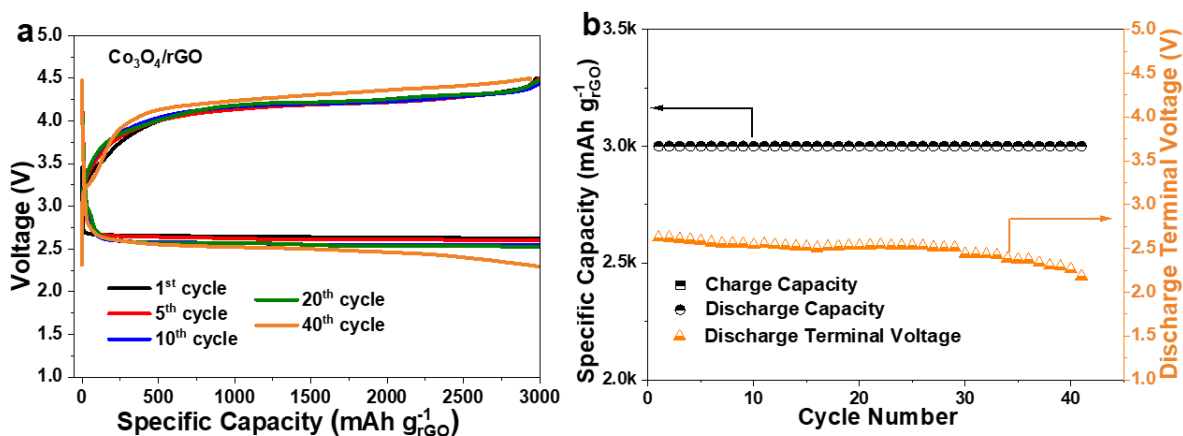


Figure 4.45. Charge and discharge profiles of $\text{Co}_3\text{O}_4/\text{rGO}$ based Li-O_2 battery with a cut-off capacity of 3000 mAh g^{-1} at a current density of 250 mA g^{-1} . (b) Discharge/charge capacity and discharge terminal voltage vs. cycle number.

When discharge/charge are controlled in larger depth (a cut-off specific capacity of 3000 mAh g^{-1}), the battery can stably run for 40 cycles by showing little polarization increase upon cycling (Figure 4.45). These data reveal the good stability of Li-O_2 battery catalyzed by $\text{Co}_3\text{O}_4/\text{rGO}$, which benefits from the high efficient decomposition of discharge products. The good cycleability of Li-O_2 battery catalyzed by $\text{Co}_3\text{O}_4/\text{rGO}$ may be partially benefited from the enhancing of mass transport for LiO_2 species and the establishment of electron transfer between catalyst and discharge products.[108]

Li-O_2 battery cycled with different current densities ($100, 200, 400, 600, 800, 1000$ and 100 mA g^{-1}) in the range of $2.0\text{-}4.5 \text{ V}$ was examined to further investigate the rate performance. Discharge and charge profiles at different densities are exhibited in Figure 4.46a. The cell overpotential increases slightly as the current density increases from 100 to 1000 mA g^{-1} , demonstrating the high catalytic activity of $\text{Co}_3\text{O}_4/\text{rGO}$ hybrid even in fast discharge/charge process. For the first

4. Results and discussion

cycle (current density 100 mA g^{-1}), the discharge and charge plateaus are at 2.69 V and 4.05 V. Once the current density is set back to 100 mA g^{-1} (31^{th} cycle), the discharge and charge plateaus can be found at 2.69 V and 4.05 V again. This behavior indicates that the discharge products do not accumulate on the cathode surface in fast discharge/charge process.

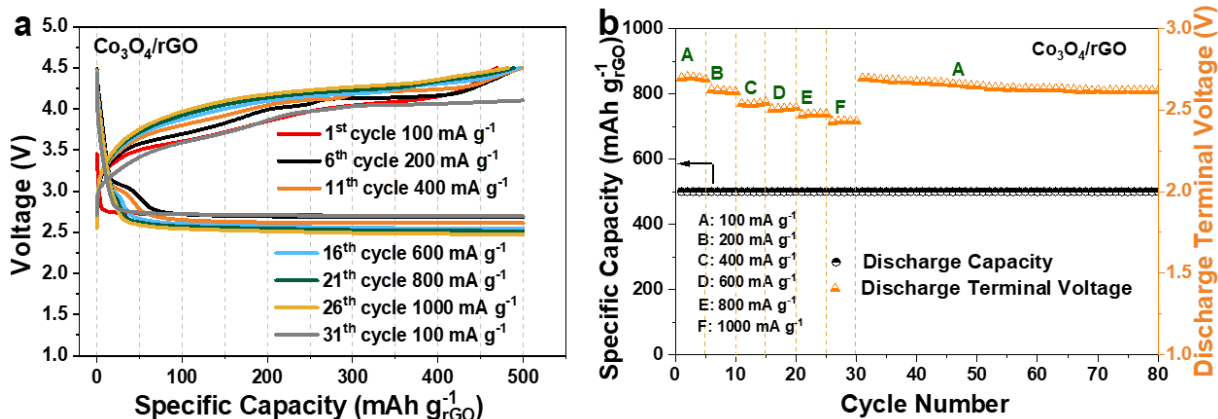


Figure 4.46. Charge and discharge behaviors of $\text{Co}_3\text{O}_4/\text{rGO}$ based battery at the different current densities ($100\text{-}1000 \text{ mA g}^{-1}$). (b) Rate capability of $\text{Co}_3\text{O}_4/\text{rGO}$ based Li-O_2 battery.

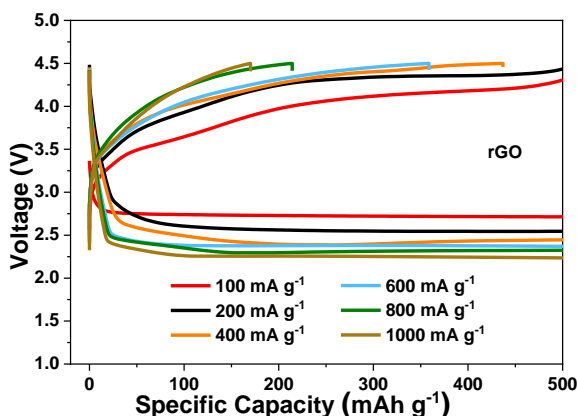


Figure 4.47. Charge and discharge behavior of rGO based battery at the different densities from $100\text{-}1000 \text{ mA g}^{-1}$.

In comparison, the battery based on rGO electrode presents poor rate performance. The rGO based cell shows lower charge capacities ($437, 358, 171$ and 214 mAh g^{-1} at the current densities of $400, 600, 800$ and 1000 mA g^{-1}), lower discharge voltage and higher charge voltage (Figure 4.47), which means most of the discharge products cannot be decomposed in fast OER process. The discharge capacities of the battery catalyzed by Co_3O_4 at different current densities ($100, 200, 400, 600, 800$ and 1000 mA g^{-1}) are constant (Figure 4.46b), indicating good reversibility even in fast discharge/charge process. Moreover, the discharge terminal voltages at current densities of $100, 200, 400, 600, 800$ and 1000 mA g^{-1} are stable at $2.69, 2.62, 2.54, 2.51, 2.48$ and 2.43 V . The

4. Results and discussion

high discharge voltage even in fast discharge process may attribute to the enhanced mass transport of LiO_2 species by Co_3O_4 and the interaction established between the discharge products and electrode by Co_3O_4 . [54], [30]

In order to investigate whether Co_3O_4 particles and rGO are well mixed, SEM and the corresponding EDX was employed. SEM images of the pristine $\text{Co}_3\text{O}_4/\text{rGO}$ electrode and corresponding EDX element mappings for C, O and Co show that Co_3O_4 and rGO are equally distributed (Figure 4.48).

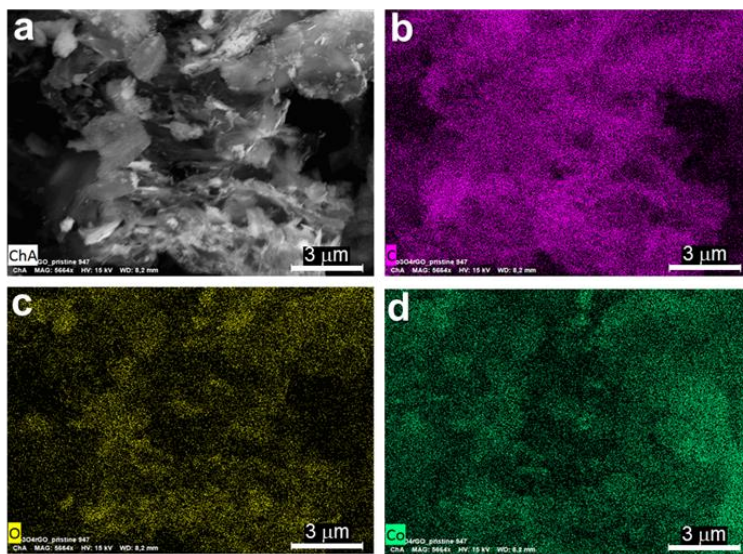


Figure 4.48. SEM image of $\text{Co}_3\text{O}_4/\text{rGO}$ pristine electrode (a); (b, c and d). The individual C, O and Co element mapping images for $\text{Co}_3\text{O}_4/\text{rGO}$ pristine electrode.

SEM measurement was also used to investigate the morphology of the discharge products. Figure 4.49 presents SEM images of a pristine electrode, an electrode after first discharge to 2.3 V and an electrode after recharging to 4.5 V. The discharge products of the $\text{Co}_3\text{O}_4/\text{rGO}$ based battery exhibit toroidal morphologies with sizes of 300-400 nm (Figure 4.49b). However, in the absence of the Co_3O_4 catalyst, the discharge products form a film on the electrode surface as shown in chapter 4.1. This film may explain the poorer cycling performance of the pure rGO sample, since it can more easily block Li^+ and O_2 diffusion pathways. High surface area rGO provide abundant exposed defect sites, which can form strong binding with LiO_2 species. [112] This will inhibit the disproportionation reaction of LiO_2 species ($2\text{LiO}_2 \rightarrow \text{Li}_2\text{O}_2 + \text{O}_2$) in solution and result in the formation of discharge products on electrode surface. In comparison, Co_3O_4 with dangling bonds has low binding energy with LiO_2 species, which can facilitate mass transport of LiO_2 species.

4. Results and discussion

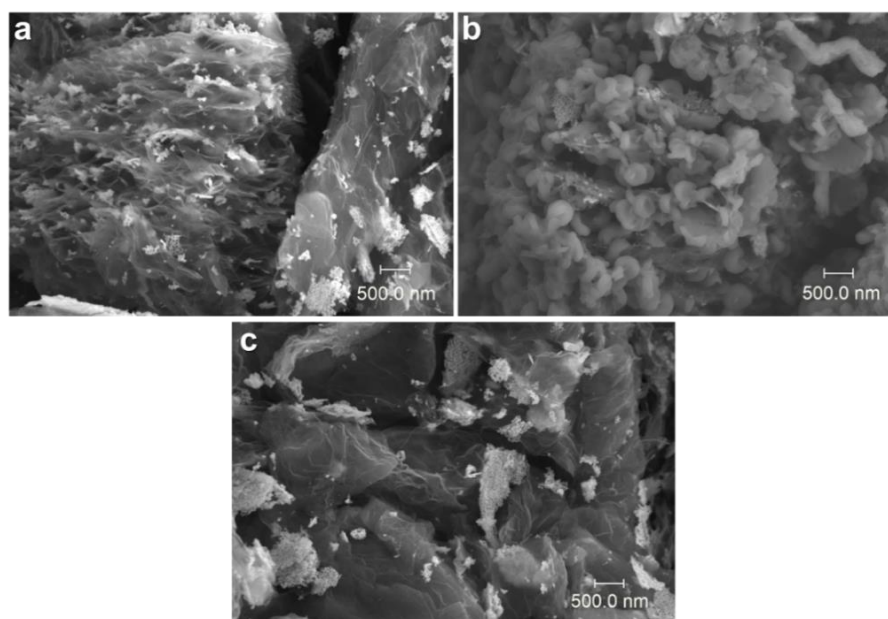


Figure 4.49. SEM images of the pristine (a), discharged (b), and charged $\text{Co}_3\text{O}_4/\text{rGO}$ electrodes (c).

The high mass transport of LiO_2 species can result in the formation of discharge products in the adjacent solution. Moreover, the nano-sized Co_3O_4 can cause higher interfacial current density, which will shorten the reaction time to form discharge products in small size. As a result, the combination of rGO and nano-sized Co_3O_4 lead to the formation of non-aggregated small sized discharge products in solution. The non-aggregated and inadhesive character of the discharge products gives sufficient space for oxygen and Li^+ transport. The transport of oxygen and Li^+ is the biggest challenge at high capacity. Moreover, the small particle size of discharge products facilitates their decomposition in the charge process, which leads to the reduction of overpotential.

SEM image and the individual C, O and Co element mapping images (EDX) of the $\text{Co}_3\text{O}_4/\text{rGO}$ electrode after recharging to 4.5 V show that Co_3O_4 and rGO are still homogeneously distributed after discharge and charge process (Figure 4.49c and Figure 4.50). Comparison of the pristine, discharged and charged electrodes, reveals that the discharge products disappear during the charging process and the original structure of $\text{Co}_3\text{O}_4/\text{rGO}$ is regained. All the SEM results indicate the excellent catalytic activity of $\text{Co}_3\text{O}_4/\text{rGO}$ for ORR/OER process.

Raman spectroscopy analysis was carried out to further investigate the structure evolution during discharge and charge process. The pristine electrode shows only the characteristic bands of rGO and Co_3O_4 (Figure 4.51a). After discharge, distinct new bands appear in the Raman spectra (Figure 4.51a). These bands disappear after recharging to 4.5 V and the original bands of Co_3O_4 and rGO

4. Results and discussion

are retrieved (Figure 4.51a). Comparison of the three spectra indicates that discharge products formed and completely decomposed during the discharge and charge process.

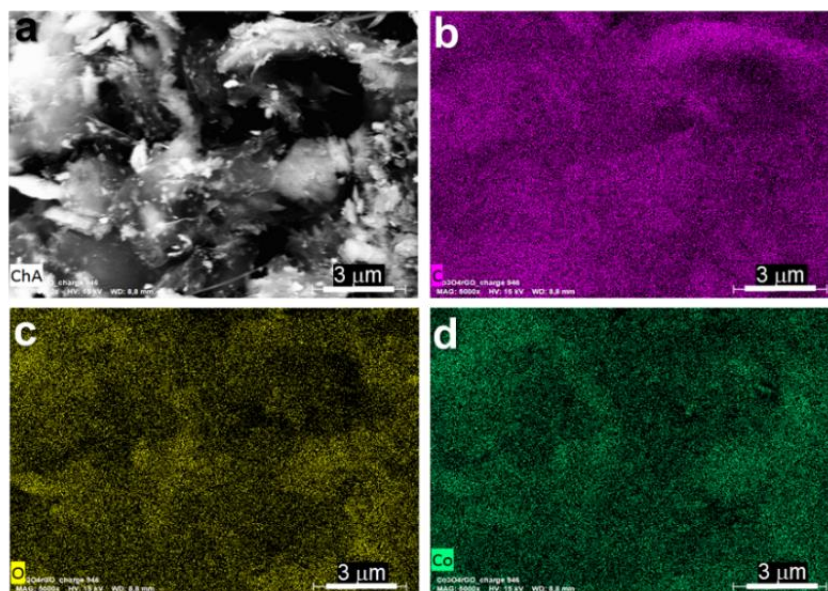


Figure 4.50. SEM image of Co₃O₄/rGO electrode after recharging to 4.5 V (a). The corresponding individual C, O and Co element mapping images (b, c and d).

The Raman spectra in the region of 100 to 1000 cm⁻¹ involve only the vibrations caused by Co₃O₄. As we talked above, Co₃O₄ spinel structure possesses five Raman-active modes: A_{1g}, E_g, and three F_{2g} modes (labeled as V, I, II, III and IV).[110] The Raman spectra of pristine electrode shows five bands at 191, 473, 517, 614 and 677 cm⁻¹. Compared to the raw Co₃O₄ material, four bands (II, III, IV and V) shift 6-7 cm⁻¹ to high frequency except for the bands at 191 cm⁻¹ (I) (Figure 4.51b). I band is assigned to F_{2g} CoO₆ scissoring vibration and III, IV, II and V bands are assigned to 2F_{2g}, E_g, A_{1g} symmetric stretching Co-O vibration mode.[113] The shift for II, III, IV and V bands is assigned to isolated surface caused by rGO.[114] No change is detected for F_{2g} (191 cm⁻¹) owing to the little influence to bond angle for scissoring vibration.[113] Raman peak at around 580 cm⁻¹ (labeled as A) appears and the intensity of another peak at 473 cm⁻¹ increases after discharge (Figure 4.51b). Increase of the peak intensity at 473 cm⁻¹ may be due to the formation of new vibration at this position. The newly emerged Raman peaks at 580 and 473 cm⁻¹ are in good agreement of LiCoO₂ species.[115],[116] It can be concluded that cubic spinel Co₃O₄ partially transforms into layered LiCoO₂ during discharge. For the charged electrode, the layered LiCoO₂ is transformed back into cubic spinel Co₃O₄ again. The transition between lithiated and non-lithiated cobalt oxide, which involves the insertion and extraction of lithium and oxygen, indicates the existence of interactions between discharge products and Co₃O₄. This interaction

4. Results and discussion

may promote the electron transfer between discharge product and Co_3O_4 . [108] The promoting of electron transfer from the discharge products to the catalyst can reduce overpotential and O_2 desorption energy. [108] The discharged electrode also shows a weak peak (labeled as α) at around 330 cm^{-1} consistent with the reported vibration of LiOH species (Figure 4.51b).

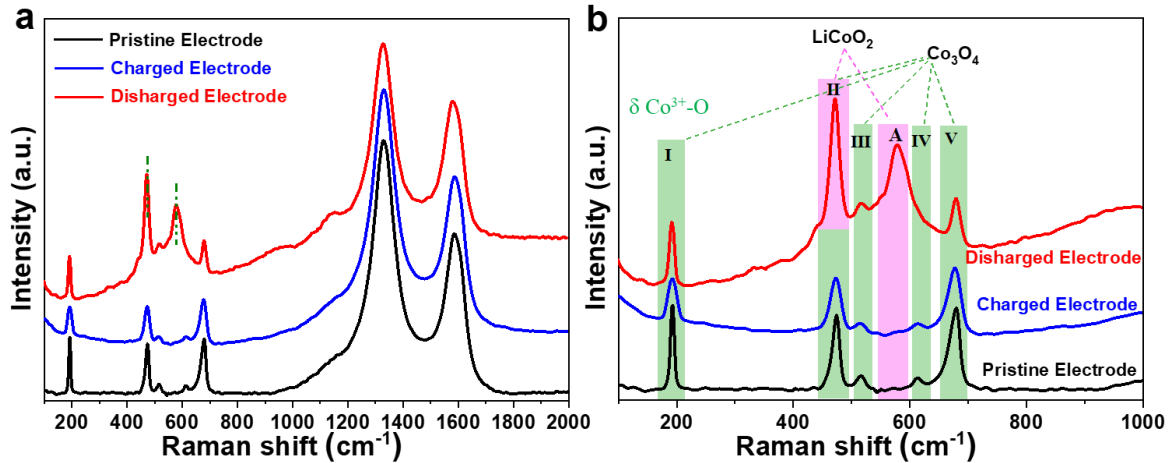


Figure 4.51. Raman spectra in the range of $100\text{-}2000\text{ cm}^{-1}$ (a) and $100\text{-}1000\text{ cm}^{-1}$ (b) for pristine, discharged and charged $\text{Co}_3\text{O}_4/\text{rGO}$ electrodes. Carbon raman spectra of pristine, discharged and charged electrodes of $\text{Co}_3\text{O}_4/\text{rGO}$ after peak-fit processing. Deconvoluted Raman spectrum of the pristine.

$\text{Co}_3\text{O}_4/\text{rGO}$ electrode exhibits two distinct peaks located at around 1335 cm^{-1} and 1592 cm^{-1} (Figure 4.52a), which are the characteristic bands for carbon material. To further study the influence of discharge and charge process to the carbon structure. A portion of the resulting averaged spectrum ($800\text{-}2000\text{ cm}^{-1}$) was also deconvoluted into four component bands (labeled as D1, D3, D4 and G) based on actual visual evidence for their presence in the averaged band envelope (Figure 4.52). [97] As we talked in chapter 4.1, the I_G/I_{D1} values are 0.36, 0.30 and 0.29 for pristine, discharged and charged rGO electrodes. While the I_G/I_{D1} values of pristine, discharged and charged $\text{Co}_3\text{O}_4/\text{rGO}$ electrodes are 0.36, 0.30 and 0.30 (Figure 4.52d). It can be concluded that the graphitization degree change similarly during the discharge process for $\text{Co}_3\text{O}_4/\text{rGO}$ and rGO electrodes. However, the graphitization degree of rGO electrode further decreases during the charge process. For $\text{Co}_3\text{O}_4/\text{rGO}$ electrode, it stays stable during the charge process. I_{D3}/I_T values of rGO electrode increase dramatically after discharge (from 0.11 to 0.16). It possibly causes by the side reactions during battery cycling with the electrolyte or the rGO itself. In comparison, I_{D3}/I_T values of $\text{Co}_3\text{O}_4/\text{rGO}$ electrode increase slightly from 0.11 to 0.13 (Figure 4.52d), which indicates less side reactions. It is noticeable that I_{D3}/I_T value of $\text{Co}_3\text{O}_4/\text{rGO}$ electrode decreases back to 0.11 after charge (Figure 4.52d). This indicates an almost complete removal of side products from electrode surface. In contrast, the I_{D3}/I_T value of rGO electrode after charge (0.14)

4. Results and discussion

stays elevated compared to its initial value (0.11). This suggests an incomplete removal of side products in case of the rGO electrode, which will result in a gradual accumulation of side products on the oxygen electrode and early cell death.

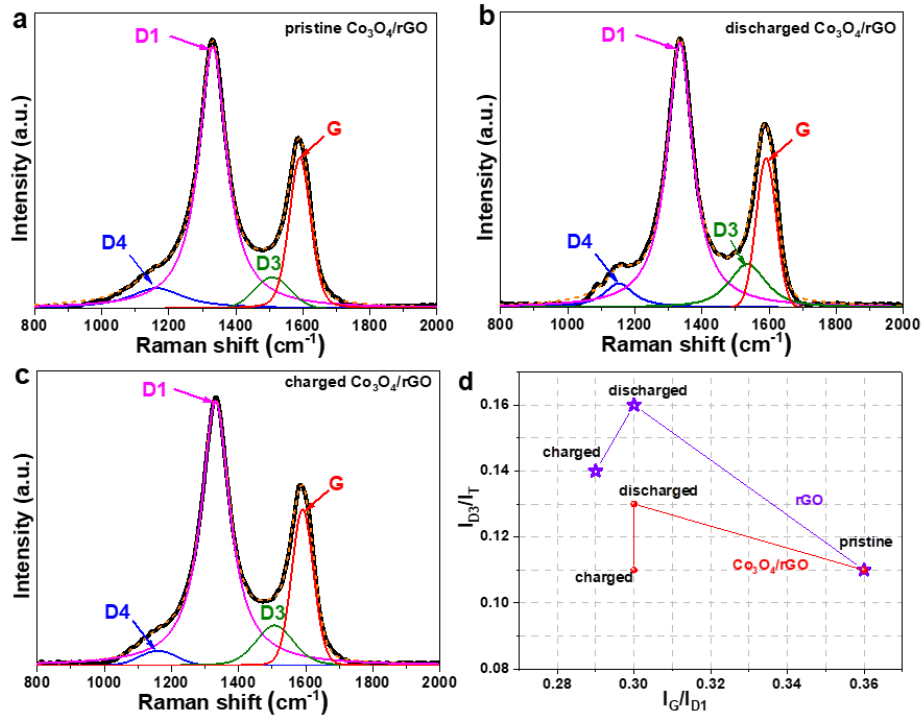


Figure 4.52. Deconvoluted Raman spectrum of the pristine/discharged/charged Co₃O₄/rGO electrodes (a, b and c), (d) I_G/I_{D1} values and I_{D3}/I_T values for the pristine/discharged/charged Co₃O₄/rGO electrodes and the pristine/discharged/charged rGO electrodes.

To demonstrate the composition and crystal structure of the discharge products, XRD using Cobalt K α radiation (1.78896 Å) is utilized. Moreover, Rietveld refinement of the crystallographic parameters is applied to analyze phase components of discharged Co₃O₄/rGO electrode (Figure 4.53a). Four phases (Co₃O₄, LiCoO₂, LiOH and Li₂O₂) are applied in this Rietveld refinement. The existence of Co₃O₄ phase comes from the as-prepared Co₃O₄. All the reflections of Co₃O₄ are in good agreement with the face-centered cubic Co₃O₄ structure model with space group *Fd-3m*. The reflections of LiCoO₂ phase correspond with the layered LiCoO₂ structure model with space group *R-3m*. However, it is very difficult to distinguish between layered phase LiCoO₂ and cubic spinel Co₃O₄ by X-ray diffraction.[117] Hence the phase ratio of these two phase cannot be obtained. Unlike the cubic spinel Co₃O₄ phase and layered LiCoO₂ phase, LiOH and Li₂O₂ phases are the main discharge products formed in the discharge process. All the reflections of LiOH are well indexed with the tetragonal LiOH structure model using the space group *P4/nmm*. The lattice parameters are $a = b = 3.5485(1)$ Å, $c = 4.3489(2)$ Å and $\alpha = \beta = \gamma = 90^\circ$ (Bragg R-factor=5.03,

4. Results and discussion

Rf-factor=3.68). The reflections of Li_2O_2 are well indexed with the hexagonal Li_2O_2 phase (space group: $P63/mmc$). The lattice parameters of the Li_2O_2 phase are $a = b = 3.1399(3) \text{ \AA}$ and $c = 7.6748(3) \text{ \AA}$ and $\alpha = \beta = 90^\circ$ and $\gamma = 120^\circ$ (Bragg R-factor=11.20, Rf-factor=9.48). This Rietveld refinement has satisfying values of $R_{\text{wp}} = 2.44 \%$, $R_p = 3.41 \%$.

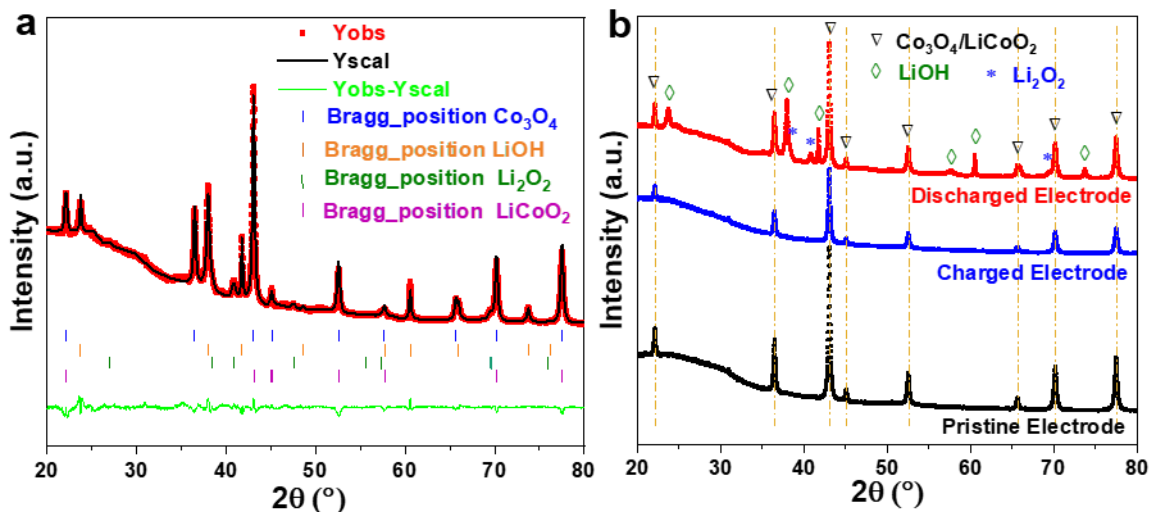


Figure 4.53. Rietveld refinement of structure models of component phases of XRD pattern ($\lambda=1.78896 \text{ \AA}$) for discharged $\text{Co}_3\text{O}_4/\text{rGO}$ electrode (a), XRD patterns of the pristine, the discharged and the charged $\text{Co}_3\text{O}_4/\text{rGO}$ electrodes (b).

XRD patterns of the pristine, discharged, and charged $\text{Co}_3\text{O}_4/\text{rGO}$ electrodes are shown in Figure 4.53b. The pristine $\text{Co}_3\text{O}_4/\text{rGO}$ electrode exhibits the representative reflexes of spinel Co_3O_4 crystalline structure. In addition, there is a broad reflex at around 24° , which is attributed to the rGO content. After discharge, distinct reflexes of LiOH and Li_2O_2 appear in the XRD pattern and the typical reflexes for spinel Co_3O_4 and rGO remain. It is noticeable that the reflexes corresponding to LiOH and Li_2O_2 disappear after recharging to 4.5 V and only the original reflexes belonging to pristine $\text{Co}_3\text{O}_4/\text{rGO}$ electrode are left. In conclusion, LiOH and Li_2O_2 species formed and decomposed reversibly during the discharge and charge process. Moreover, the remaining reflexes of Co_3O_4 demonstrate that the spinel structure of Co_3O_4 is unchanged during the discharge/charge process.

XPS spectroscopy was used to determine the oxidation state evolution in the discharge process. The XPS spectrum of the pristine and discharged $\text{Co}_3\text{O}_4/\text{rGO}$ electrodes confirm a mixed-valent Co containing Co^{3+} and Co^{2+} species in the fresh and discharged $\text{Co}_3\text{O}_4/\text{rGO}$ cathode (Figure 4.54). A quantitative analysis of the Co 2p spectra has to be driven and considered very carefully here because of the very weak and thus noisy signal obtained for the discharged electrode.

4. Results and discussion

Nevertheless, a slight decrease of the Co^{2+} contribution to the total Cobalt concentration can be observed after discharge to 2.3 V (from ~38 % down to ~30 %). The decreased peak intensity of the Co^{2+} could be attributed to the interaction between Li^+ , Co_3O_4 and LiO_2 species.[118] The possible reaction equation is $2e^- + 2\text{Li}^+ + \text{LiO}_2 + \text{Co}_3\text{O}_4 \rightarrow 3\text{LiCoO}_2$.

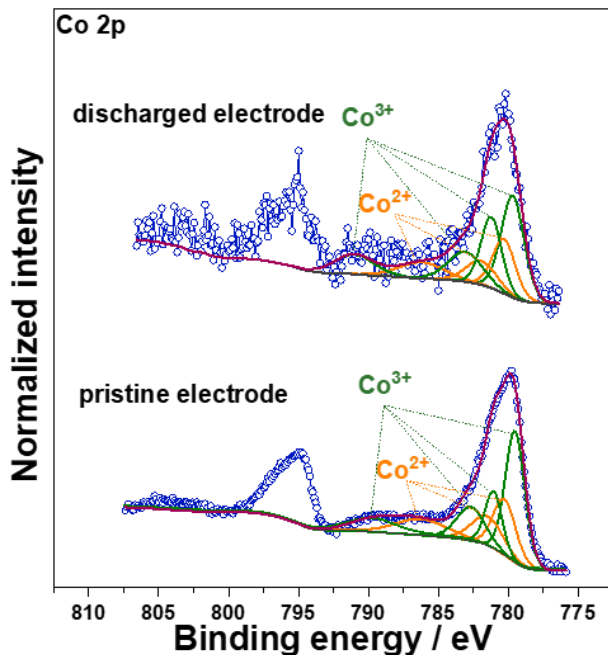


Figure 4.54. High-resolution XPS spectrum of the Co 2p for pristine and discharged $\text{Co}_3\text{O}_4/\text{rGO}$ electrodes.

4.3 Improvements of electrochemical performance by soluble catalysts

Considering the very limited electrochemical activity of pure PCW material. Different soluble catalysts (DBBQ and LiI) was added into electrolyte to improve the electrochemical performance of PCW based Li- O_2 batteries. Galvanostatic charge-discharge tests were carried out to explore the difference in electrochemical performance with four electrolytes (LiTFSI, LiTFSI/LiI, LiTFSI/DBBQ, and LiTFSI/DBBQ/LiI). The initial discharge-charge profiles of PCW based Li- O_2 batteries with LiTFSI, LiTFSI/LiI, LiTFSI/DBBQ, and LiTFSI/DBBQ/LiI electrolyte are exhibited in Figure 4.55a. In the presence of LiI, batteries with or without DBBQ both show much lower charge voltage during charge. While batteries with DBBQ show a slight increase of the discharge plateau, independent from the presence of LiI. Moreover, the capacity of batteries with DBBQ in the electrolyte present a remarkable improvement, which delivers near 3 times higher discharge capacity than that without DBBQ. The increase of the discharge capacity can be

4. Results and discussion

attributed to the formation of discharge products in solution in the presence of DBBQ. Firstly, Li^+ , H_2O and DBBQ complex to form $\text{LiDBBQ}\cdot n\text{H}_2\text{O}$, then the $\text{LiDBBQ}\cdot n\text{H}_2\text{O}$ combines O_2 to produce $\text{LiDBBQO}_2\cdot n\text{H}_2\text{O}$ intermediates.[16],[31] Otherwise, $\text{LiDBBQ}\cdot n\text{H}_2\text{O}$ can diffuse a long distance away from the electrode surface, which expands the reaction area in solution and allows the electrochemical reaction to take place deeper in the electrolyte.

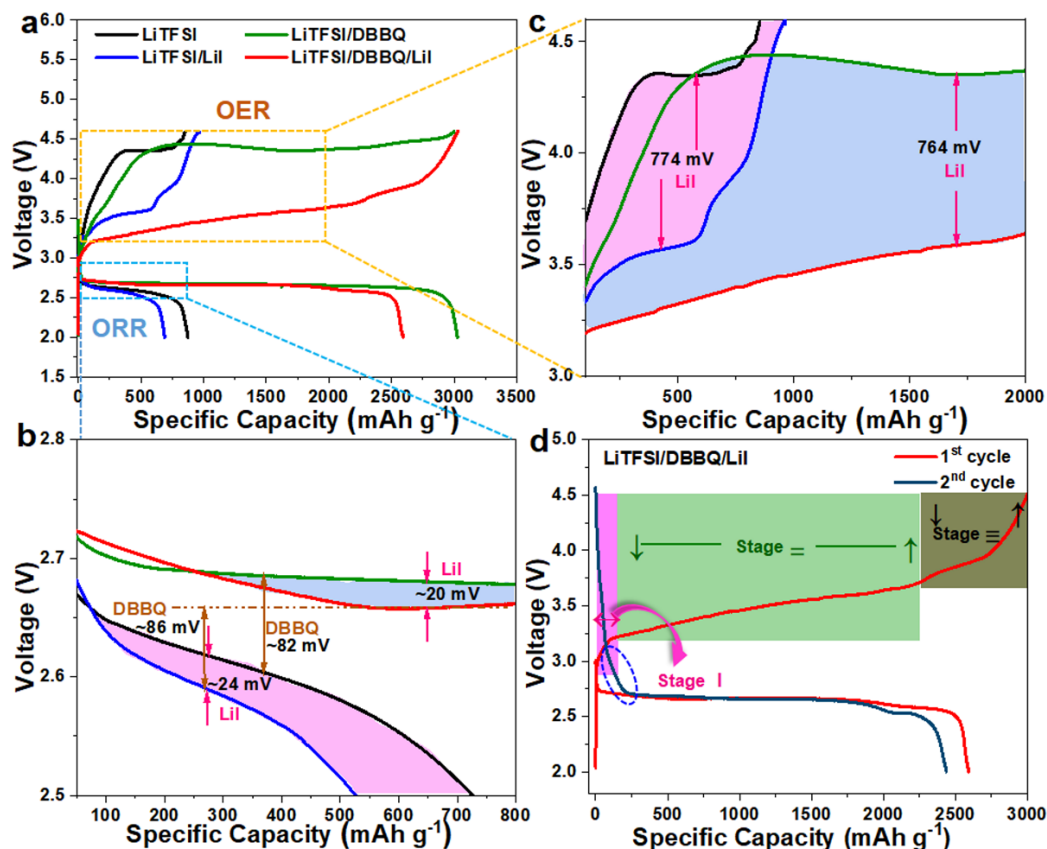


Figure 4.55. Discharge/charge profiles of Li-O₂ batteries with LiTFSI, LiTFSI/LiI, LiTFSI/DBBQ and LiTFSI/DBBQ/LiI electrolyte at the current density of 50 mA g⁻¹ (a); Magnified ORR process in a capacity range of 50-1400 mAh g⁻¹ and a voltage range of 2.5-2.8 V (b); Magnified OER process in a capacity range of 100-2000 mAh g⁻¹ and a voltage range of 3.0-4.6 V (c); The full discharge-charge curves between 2.0-4.6 V with LiTFSI/DBBQ/LiI electrolyte (d).

The ORR process was magnified in the capacity range of 50-1400 mAh g⁻¹ and voltage range of 2.5-2.8 V (Figure 4.55b). It can be seen that the discharge voltage increases about ~66 mV with DBBQ in electrolyte. The increase of the discharge plateau caused by DBBQ can be ascribed to the formation of $\text{LiDBBQO}_2\cdot n\text{H}_2\text{O}$ intermediates which possess a lower free energy than LiO_2 . [57],[78] The OER process was magnified in the capacity range of 100-2000 mAh g⁻¹ and voltage range of 3.0-4.6 V (Figure 4.55c). It can be seen that the charge voltage decreases by about ~774 mV with LiI in the electrolyte. The decrease of the charge voltage caused by the LiI mediator

4. Results and discussion

is ascribed to the oxidation reaction of $3\text{I}^- \rightarrow \text{I}_3^- + 2\text{e}^-$ and $\text{I}_3^- \rightarrow 3/2\text{I}_2 + \text{e}^-$ and chemical reaction of $4\text{LiOH} + 6\text{I}_2 \rightarrow 4\text{LiI}_3 + \text{O}_2 + 2\text{H}_2\text{O}$. Hence, batteries with LiTFSI/DBBQ/LiI electrolyte, which combine the benefits of both catalysts, exhibit lower charge voltage, higher discharge voltage and higher discharge capacity.

Upon charging, the battery with dual redox mediators (DBBQ/LiI) exhibits three voltage plateaus (Figure 4.55d). The first plateau (Stage I) is related to the oxidation of I^- to I_3^- ($3\text{I}^- \rightarrow \text{I}_3^- + 2\text{e}^-$, $E^0 \sim 3.0$ V). The second one (Stage II) with extended capacity is originating from the oxidation of I_3^- to I_2 ($\text{I}_3^- \rightarrow 3/2\text{I}_2 + \text{e}^-$, $E^0 \sim 3.5$ V) and the reaction between LiOH and I_2 ($4\text{LiOH} + 6\text{I}_2 \rightarrow 4\text{LiI}_3 + \text{O}_2 + 2\text{H}_2\text{O}$). [79],[80] The third plateau (Stage III) can be ascribed to the original decomposition of LiOH in the charge process ($4\text{LiOH} \rightarrow 4\text{Li}^+ + \text{O}_2 + 2\text{H}_2\text{O} + 4\text{e}^-$). Based on stoichiometry, the theoretical capacity of the I_3^-/I_2 redox couple should be half of that of the I^-/I_3^- redox couple. [55] However, it can be seen from Fig. 1b that the second plateau is much longer than the first one. The far extended capacity at the high voltage (Stage II) indicates an efficient reaction between I_2 and LiOH, which will result in the generation of I_3^- and O_2 . [87] It is noteworthy that a new plateau appears at around 3.0 V during the second discharge, which can be assigned to the reduction of I_3^- to I^- ($\text{I}_3^- + 2\text{e}^- \rightarrow 3\text{I}^-$). [55] The remaining I_3^- in the electrolyte is generated from the reaction between LiOH and I_2 . The electrodes after full discharge and charge are immersed in 2 mL acetonitrile. It can be seen that the acetonitrile of discharged electrodes are transparent, whereas that of the charged electrodes have a yellow tint (Figure 4.63). The yellow tint can be ascribed to the presence of I_3^- in the electrode. The discoloration after discharge is due to the reduction of I_3^- to I^- in the discharge process. This agrees well with electrochemical results. In comparison, the batteries without LiI in the electrolyte exhibit only one obvious charging plateau.

To analyze the composition and structure of the discharge products XRD measurements were carried out. The XRD pattern of the electrode with LiTFSI/DBBQ/LiI electrolyte after the 1st discharged presents typical reflexes of LiOH (Figure 4.56, JCPDS Number: 01-085-0777), which indicates the formation of LiOH during discharge. Moreover, the typical peaks of LiOH disappear and the original peaks of PCW restore after charge (Figure 4.56), which demonstrates the complete decomposition of LiOH during charge. All three XRD patterns possess two broad diffraction reflections, (002) and (100), originating from PCW. It appears that the (002) diffraction position shift a bit toward low angle after charge, indicating an increase of interlayer distance of PCW. This most likely cause by the side reactions of electrolyte and carbon at high voltage of charge.

4. Results and discussion

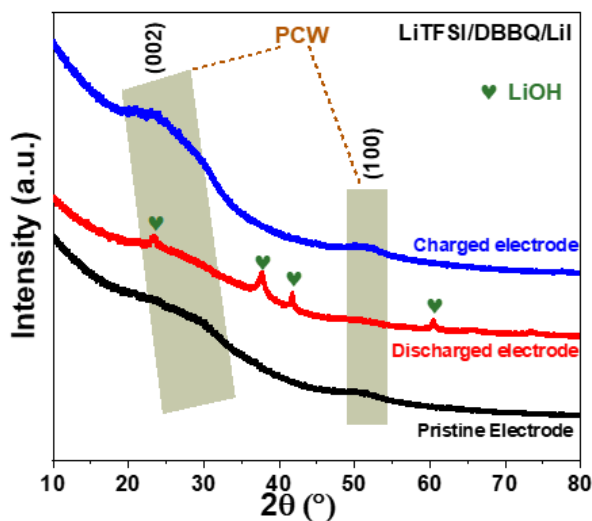


Figure 4.56. XRD patterns of the pristine electrode and discharged/charged electrodes of the first cycle with DBBQ and LiI in electrolyte, which demonstrate the formation and decomposition of LiOH in the discharge and charge process.

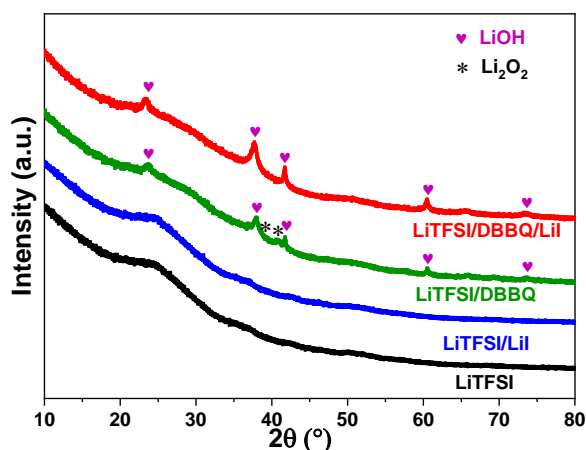


Figure 4.57. XRD patterns of the discharged electrodes with LiTFSI (black), LiTFSI/LiI (blue), LiTFSI/DBBQ (green) and LiTFSI/DBBQ/LiI (red) electrolyte.

XRD patterns of the discharged electrodes with LiTFSI, LiTFSI/LiI, and LiTFSI/DBBQ electrolyte are displayed in Figure 4.57. The diffraction peaks of the discharged electrode with LiTFSI/DBBQ electrolyte can be indexed as LiOH and Li₂O₂ (JCPDS Number: 00-009-0355). However, there is only one kind of discharge products (LiOH) in LiTFSI/DBBQ/LiI electrolyte. This can be ascribed to the reversible deprotonation of H₂O catalyzed by LiI, which can further facilitate the LiOH formation.[80],[119] There are no apparent diffraction peaks for the discharged electrodes with LiTFSI and LiTFSI/LiI electrolyte. This could be attributed to the lower amount of discharge products formed in these two electrolytes, corresponding to their significantly lower electrochemical capacity.

4. Results and discussion

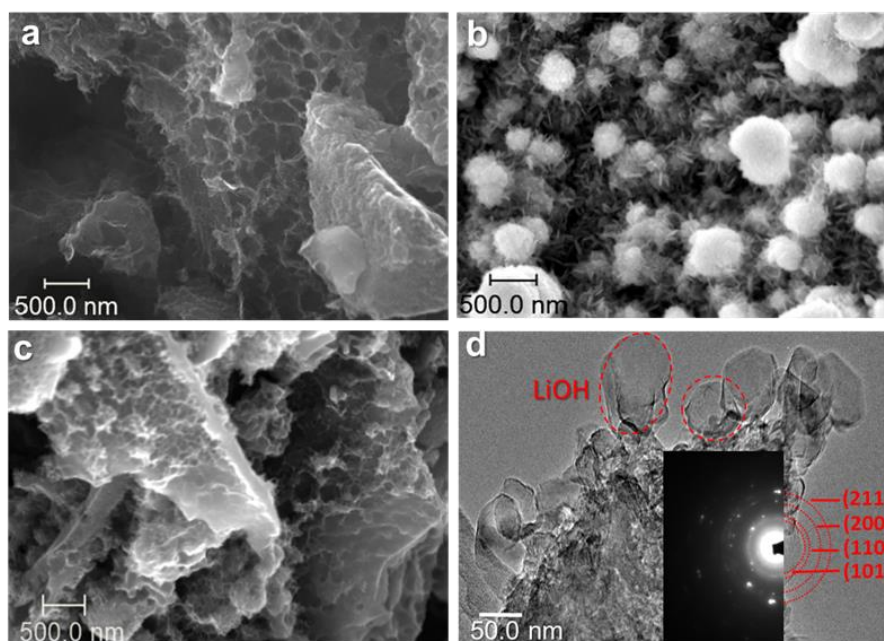


Figure 4.58. SEM images of the pristine electrode (a), discharged electrode with LiTFSI/DBBQ/LiI (b) and charged electrode with LiTFSI/DBBQ/LiI (c); (d) TEM image of the discharged electrode, the inset is SAED pattern of the discharged electrode.

SEM and TEM were applied to characterize the morphologies of discharge products formed during discharge. SEM images of the pristine electrode and electrodes after 1st discharge/charge in LiTFSI/DBBQ/LiI, LiTFSI, LiTFSI/LiI, and LiTFSI/DBBQ electrolytes are presented in Figure 4.58 and Figure 4.59. With DBBQ and LiI in the electrolyte, the electrode is covered with small and thin needle-like particles aggregated into a mossy structure on its surface (Figure 4.58b). When recharged to 4.6 V, the discharge products disappear and the initial structure of the as-prepared PCW regained (Figure 4.58c). SEM images of the pristine/discharged/charged electrodes with LiTFSI/DBBQ/LiI electrolyte clearly show the formation and decomposition of the discharge products during discharge and charge. The discharged electrode with LiTFSI/DBBQ/LiI electrolyte was further examined by TEM (Figure 4.58d), which again demonstrates the formation of small thin platelets during discharge. The discharge products were further confirmed by selected area electron diffraction (SAED) patterns. The corresponding characteristic diffraction spots were shown as inset in Figure 4.58d. Diffraction signals observed correspond to (211), (200), (110), and (101) crystalline planes of LiOH.

However, batteries with LiTFSI electrolyte exhibit only few rice-shape discharge products on the PCW electrode surface (Figure 4.59a), which corresponds well with its low discharge capacity. In the presence of LiI, the morphology of the discharge products changes from rice-shape to sheet-

4. Results and discussion

like morphology (Figure 4.59c). Also for this electrolyte composition only few discharge products can be observed, which agrees with the low capacity of Li-O₂ battery with LiTFSI/LiI electrolyte. With DBBQ in the electrolyte, the electrode surface is extensively covered by thin platelets after discharge (Figure 4.59e), which is in accordance with the enhanced capacity of batteries with LiTFSI/DBBQ. The discharge products all disappear for all three kinds of electrolytes after being recharged to 4.6 V (Figure 4.59), which demonstrates their almost complete decomposition during discharge.

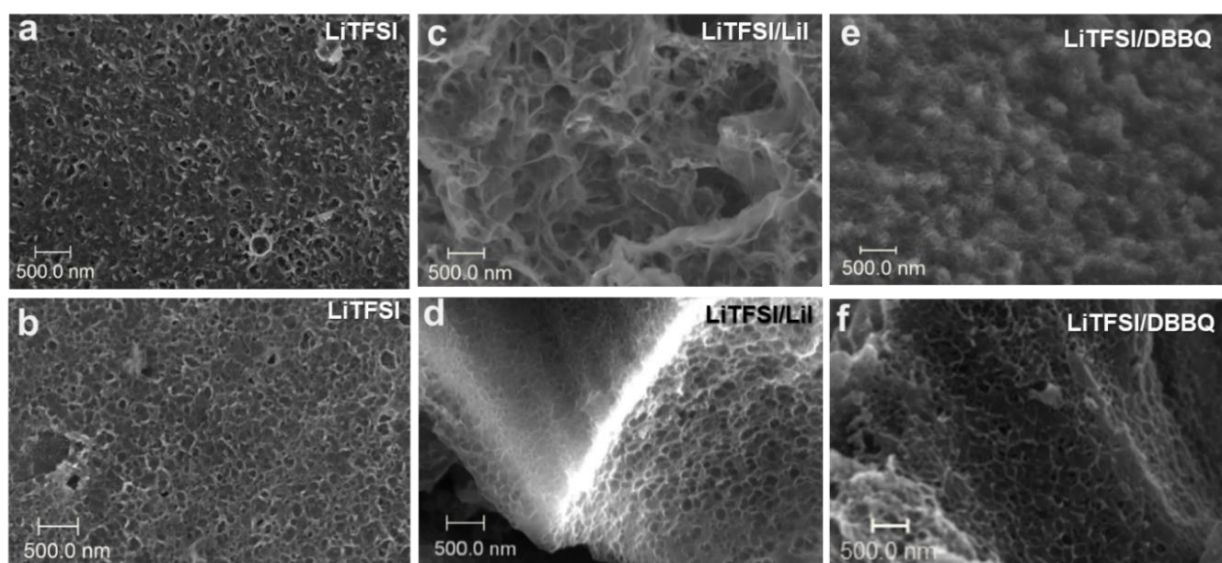


Figure 4.59. SEM images of the discharged electrodes with LiTFSI (a), LiTFSI/LiI (c), and LiTFSI/DBBQ (e); SEM images of the charged electrodes with LiTFSI (b), LiTFSI/LiI (d), and LiTFSI/DBBQ (f).

In order to determine the nature of the discharge products, Raman measurements were carried out. Figure 4.60 shows typical Raman spectra of the discharge products resulting from the four different electrolytes. In the spectra of electrodes without catalysts (DBBQ and LiI) and with LiI, there are no obvious bands from the discharge products. This may be attributed to the low amount of discharge products formed in these two electrolytes and is consistent with the SEM, XRD and electrochemical results. With DBBQ in the electrolyte, two distinct peaks at 323 and 789 cm⁻¹ can be observed, which are associated with the presence of LiOH and Li₂O₂. This means that both Li₂O₂ and LiOH are formed during discharge. This result agrees with the XRD result discussed above. With both DBBQ and LiI in the electrolyte, there is only one distinct peak at 323 cm⁻¹ associated with the presence of LiOH. This indicates the main discharge product is LiOH in this electrolyte, which is also in accordance with the XRD result.

4. Results and discussion

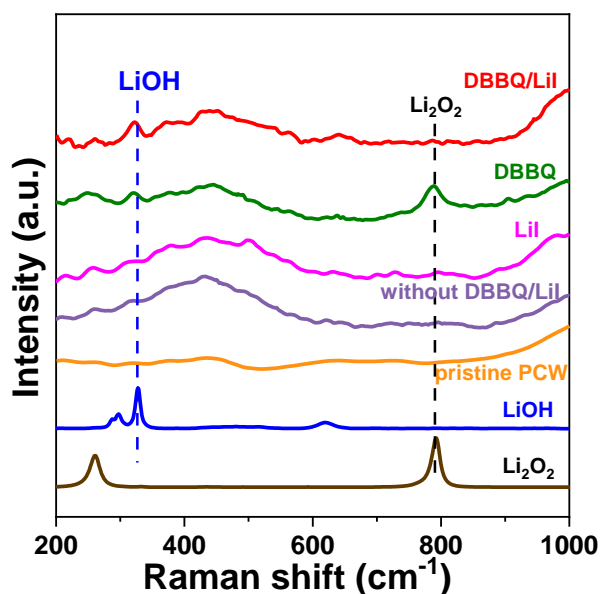


Figure 4.60. Raman spectra of Li₂O₂ reference, LiOH reference, pristine PCW electrode, discharged electrode without DBBQ and LiI, discharged electrode with LiI, discharged electrode with DBBQ, discharged electrode with DBBQ and LiI.

Galvanostatic discharge-charge measurements of several cycles were carried out to determine the cycling performance of the batteries with the different electrolytes. Galvanostatic discharge-charge profiles of the initial 9 cycles, and the variation of discharge capacity and capacity retention vs. cycle number in the four different electrolytes are shown in Figure 4.61.

As we talked in chapter 4.1, an initial discharge capacity of 876 mAh g⁻¹ was obtained for batteries with the LiTFSI electrolyte. The capacity decreased to only 331 mAh g⁻¹ (38% capacity retention) after 9 cycles. This result shows that Li-O₂ battery with LiTFSI exhibits a very low initial discharge capacity and fast capacity fading. With the introduction of the oxidation catalyst LiI, batteries display an initial discharge capacity of 690 mAh g⁻¹ and capacity fading is significantly reduced in the following 9 cycles (87% capacity retention). This result means that the presence of LiI in the electrolyte can significantly reduce the degradation of the discharge capacity. The higher capacity retention originated from LiI is ascribed to the low decomposition voltage of LiOH under participation of LiI.[32] Since E⁰ is about ~3.0 V for I⁻/I₃⁻ redox couple, which is higher than E⁰ for O₂ reduced to LiO₂, the shuttle mechanism did not occur during ORR process. The amount of electrolyte used in one battery is ~220 μL (LiI concentration: 0.05 mol L⁻¹). We hypothesized all I⁻ were oxidized to I₃⁻ during OER process, the capacity devoting of I⁻/I₃⁻ redox couple during the following discharge process is about 0.13 mAh. Considering the mass loading of PCW material is about 1.5 mg, I⁻/I₃⁻ redox couple contributes about 87 mAh g⁻¹ capacity to the total capacity of

4. Results and discussion

PCW based battery. Compared to the total capacity of PCW based battery, LiI contributes very less capacity to the total capacity of PCW based battery. So my capacity comparison analysis did not consider the capacity devoting of LiI. The reduction catalyst DBBQ results in a high capacity of 3025 mAh g^{-1} but poor capacity retention of only 949 mAh g^{-1} (31% capacity retention) after 9 cycles. This result confirms that DBBQ is a good reduction catalyst which enhance the discharge capacity of a Li-O₂ battery. The increase of the discharge capacity can be attributed to the formation of discharge products in solution in the presence of DBBQ. Though the initial discharge capacity is greatly improved in the present of DBBQ, the following discharge capacities decay very fast. In contrast, batteries with dual catalysts (DBBQ and LiI) delivers a maximum capacity of 2592 mAh g^{-1} and the capacity retention is 56% after 9 cycles. It can be concluded that the discharge capacity and cycleability are both enhanced with dual catalysts (DBBQ and LiI) in the electrolyte.

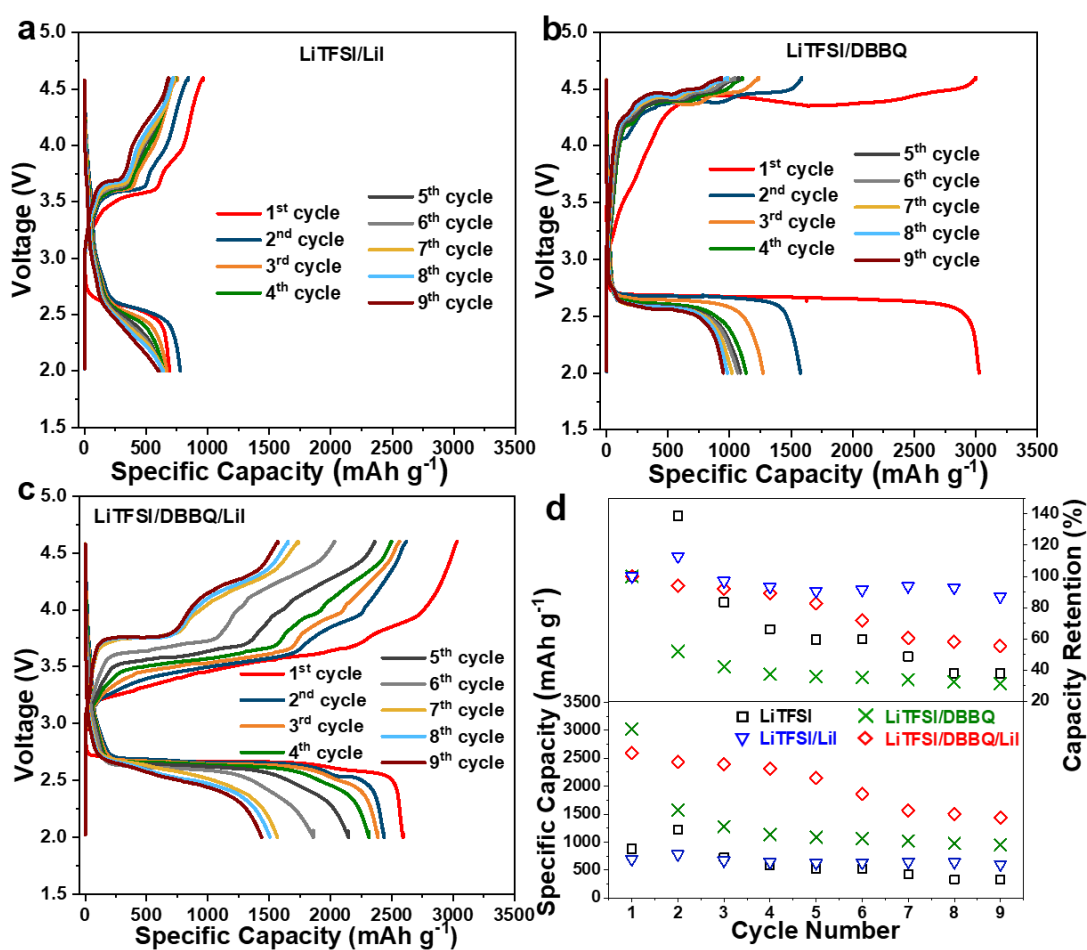


Figure 4.61. Galvanostatic discharge-charge curves of Li-O₂ batteries with LiTFSI/LiI electrolyte (a), LiTFSI/DBBQ electrolyte (b) and LiTFSI/DBBQ/LiI electrolyte (c) at the current density of 50 mA g^{-1} between 2.0-4.6 V; (d) Discharge capacity and capacity retention with LiTFSI, LiTFSI/LiI, LiTFSI/DBBQ and LiTFSI/DBBQ/LiI electrolyte vs. cycle number.

4. Results and discussion

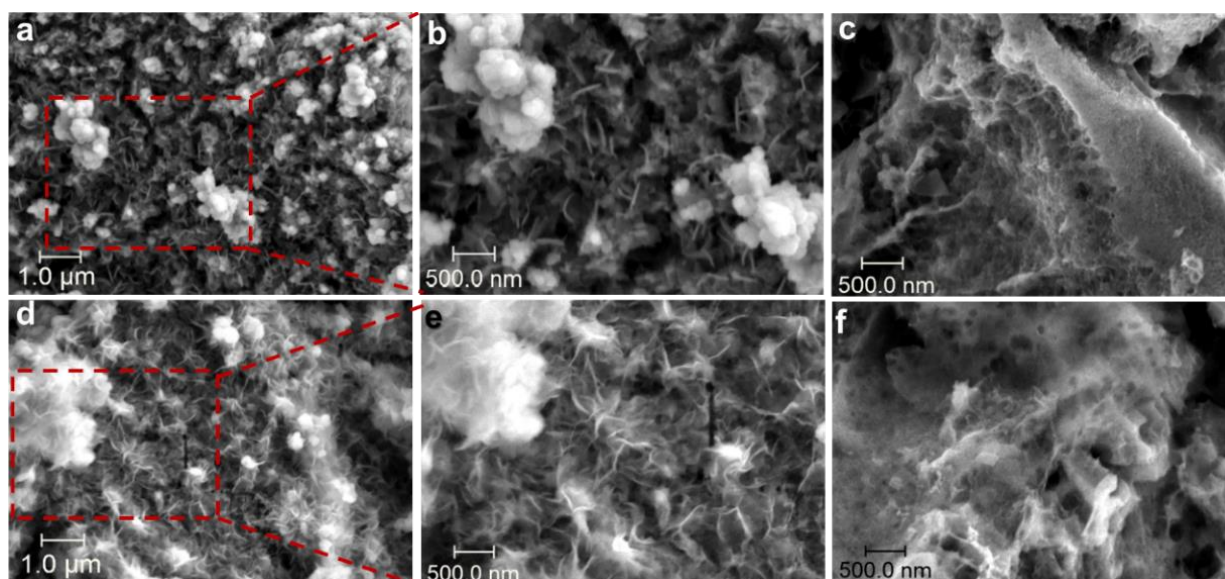


Figure 4.62. SEM images of the discharged electrodes of the fourth cycle (a) and (b), SEM image of the charged electrode of the fourth cycle (d). SEM images of the discharged electrode of the seventh cycle (c) and (e), SEM image of the charged electrode for the seventh cycle (f).

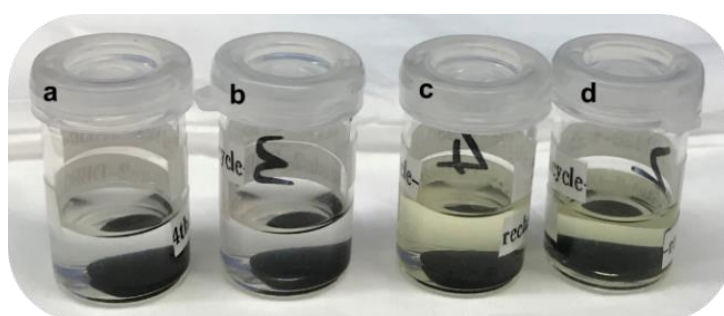


Figure 4.63. Electrodes after the fourth full discharge to 2.0 V (a), the fourth full charge to 4.6 V (b), the seventh discharge to 2.0 V (c), the seventh charge to 4.6 V soaked in 2 mL acetonitrile separately.

SEM images of the discharged/charged electrodes of the fourth and seventh cycles are further examined to explore the morphology change and the decomposition level of the discharge products during long term cycling. The discharged products of the fourth cycle exhibit larger platelets morphology compared with the first cycle discharge products (Figure 4.62a and b). Moreover, the discharge products continuously grow into a layer covering the electrode surface after the seventh cycle (Figure 4.62d and e). This could be explained by the presence of small amounts of undecomposed products acting as nucleation sites for the growth of new crystals during subsequent discharge. The discharge product with big size is harder to decompose during charge. Moreover, the gradual increase of platelets size with cycling will form a passivation film on electrode surface, which will gradually block the oxygen and electrolyte pathways and inhibit charge transfer. This results agree with the gradual fading of the capacity and the increase of the

4. Results and discussion

voltage gap. After four cycles, the charged electrode still presents the structure of raw PCW material (Figure 4.62c). However, the charged electrode of the seventh cycle is covered with a layer of undecomposed film (Figure 4.62f), which indicates the gradual accumulation of undecomposed discharge products on the electrode surface. Hence, the gradual accumulation of undecomposed discharge products on electrode surface must be considered as the primary reason for the capacity fading and increase of the voltage gap.

To further analyze the composition and structure of the discharge products after long term cycling, XRD measurements were carried out for the discharged electrodes of the fourth and seventh cycles. XRD patterns of the discharged electrodes for the fourth and seventh cycle still present typical reflexes of LiOH (JCPDS Number: 01-085-0777) (Figure 4.64). This indicates that the primary discharge products of the fourth and seventh cycle with LiTFSI/DBBQ/LiI electrolyte are still LiOH. It appears that the diffractions of the 4th and 7th cycle are broader than of the 1st cycle, which may probably cause by the decrease of the amounts or the long range ordering of LiOH.

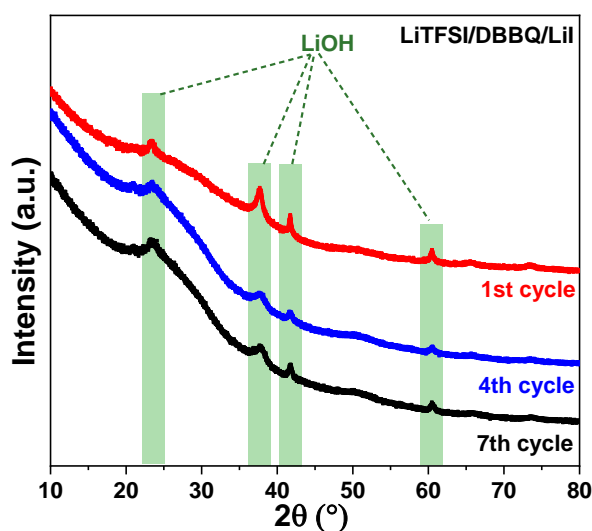


Figure 4.64. (a) XRD patterns of the pristine electrode and discharged/charged electrodes of the first cycle with LiTFSI/DBBQ/LiI electrolyte, which demonstrate the formation and decomposition of LiOH in the discharge and charge process; (b) XRD patterns of the discharged electrodes of the first, fourth and seventh cycles.

To study changes of the carbon structure during the ORR and OER process with the electrolyte containing DBBQ and LiI, Raman spectra of the electrodes in the range of 800-2000 cm^{-1} were deconvoluted into the four component bands (D1, D3, D4 and G) of graphitic carbon materials (Figure 4.65). The I_G/I_{D1} values are 0.40, 0.38 and 0.38 for the pristine, 1st discharged and 1st charged PCW electrodes, respectively (Figure 4.65f). The graphitization degree of the PCW did not decrease very much in the initial discharge and charge process. In contrast, I_G/I_D values of the

4. Results and discussion

PCW electrode discharged without soluble catalysts decreases very much in the discharge process (from 0.40 to 0.17). The heavy damage of graphite structure may attribute to the high content of O for PCW (8.4 at%), which will induce more surface function group. The O-containing function group can be easily attacked by LiO_2 species, which will lead to the decrease of graphitization degree. While DBBQ can promote the formation of discharge products in solution, which reduces the reactions between LiO_2 species and electrode surface. This can protect the oxygen electrode, which is beneficial for long term cycling.

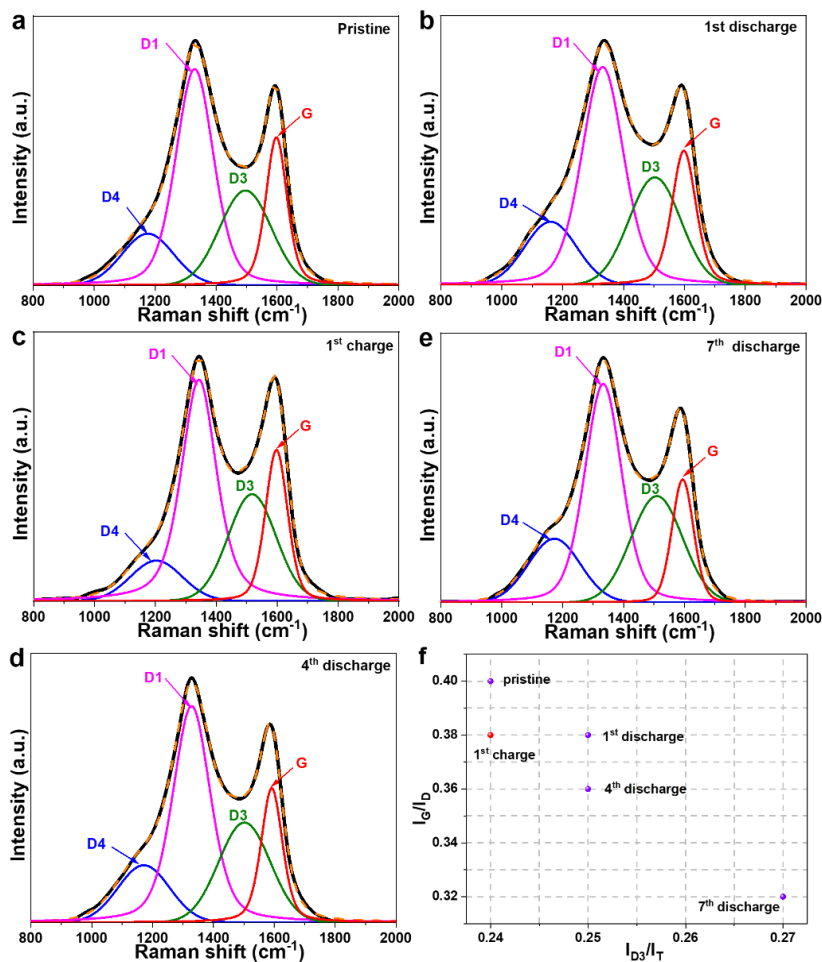


Figure 4.65. Deconvoluted Raman spectrum of the pristine/1st discharged/1st charged/4th discharged/7th discharged PCW electrodes (a, b, c, d and e) in the 800 to 2000 cm^{-1} region. (f) Comparison of I_G/I_{D1} value and I_{D3}/I_T value for the pristine/1st discharged/1st charged/4th discharged/7th discharged electrodes.

The graphitization degree after extended cycling was further studied. The I_G/I_{D1} ratio for the discharged electrodes after the 4th and 7th cycle is 0.36 and 0.32, respectively (Figure 4.65f), which indicates a further decrease of the graphitization degree of PCW electrode during cycling. The I_{D3}/I_T values of the pristine electrode and the discharged electrodes after the 1st, 4th and 7th cycle are 0.24, 0.25, 0.25 and 0.27 (Figure 4.65f), which indicates a slightly increase of fragments or

4. Results and discussion

functional groups in the amorphous phase during the initial four cycles and an obvious increase for the 7th cycle. The increase of fragments or functional groups in the amorphous phase is ascribed to the side reactions during battery cycling with the electrolyte or the PCW itself. In comparison, PCW electrode discharged without catalysts exhibits an obvious increase of I_{D3}/I_T value (from 0.24 to 0.28). This can be attributed to the formation of discharge products in solution in the presence of DBBQ. After the charge process, I_{D3}/I_T value decreases back to 0.24, indicates an almost complete removal of side products from electrode surface.

Figure 4.66 shows the cyclability of the optimized battery with the LiTFSI/DBBQ/LiI electrolyte, when the specific capacity is limited to 500 mAh g^{-1} and the battery is cycled at a current density of 100 mA g^{-1} . The potential during charge stays below 3.55 V during the initial cycle. During extended cycling the charge terminal voltage gradually increases to 4.38 V within 36 cycles. The initial discharge terminal voltage is 2.72 V and reduces to 2.52V after 36 cycles. The primary causation of the increase of charge potential and the decrease of discharge potential is the microporous structure of the PCW material, which can be easily blocked by discharge products, [37],[1] The blocking of micropores can affect the transport of LiI to electrochemical reaction sites of the cathode, which will result in the accumulation of discharge products on electrode surface little by little.

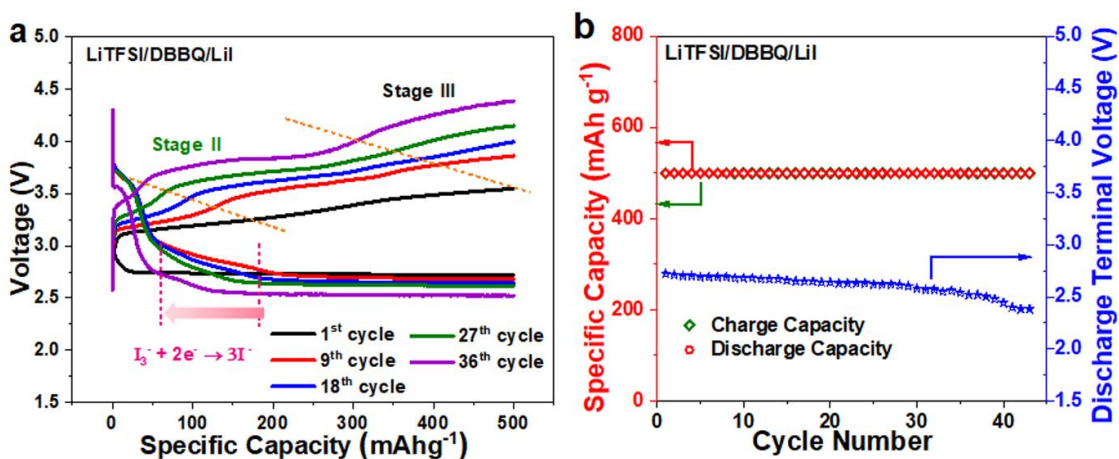


Figure 4.66. (a) Charge and discharge profiles of Li-O₂ battery with LiTFSI/DBBQ/LiI electrolyte with a cut-off capacity of 500 mAh g^{-1} at a current density of 100 mA g^{-1} . (b) Discharge/charge capacity and discharge terminal voltage vs. cycle number with LiTFSI/DBBQ/LiI electrolyte.

It can be seen from Figure 4.66a that the plateaus corresponding to the I_3^-/I^- couple become shorter and shorter from the 1st to the 36th cycle. This is most likely due to the gradual accumulation of undecomposed products on the electrode surface, which reduces the amount of I^- that can arrive

4. Summary

at the electrochemical active reaction sites by blocking diffusion pathways, and the loss of iodine by side reactions. At the same time the plateau ascribed to $4\text{LiOH} \rightarrow 4\text{Li}^+ + \text{O}_2 + 2\text{H}_2\text{O} + 4\text{e}^-$ becomes longer and longer, which indicates the direct decomposition of LiOH becomes more and more dominating. Similarly, the blocking of micropores can also block the DBBQ diffusion pathway to the electrode surface, which will result in the decrease of discharge voltage. As a result, batteries with LiTFSI/DBBQ/LiI electrolyte can only exhibit a cyclability of 43 cycles with a cut-off capacity of 500 mAh g^{-1} . The discharge terminal voltage reaches about 2.38 V after 43 cycles (Figure 4.66b). It can be concluded from the above results that the structure of cathode materials greatly affects the electrochemical performance of soluble redox mediators. Hence, exploring suitable cathode materials for soluble mediators which allow free diffusion through the interior/exterior parts of the oxygen electrode is significant to enhance catalytic performance.[120]

5. Summary

Carbon materials are the most widely explored cathode materials for Li-O₂ batteries. A series of factors, such as graphitization degree, pore size, pore volume and functional groups, greatly influence their electrochemical activity. In this thesis, we synthesized microporous honeycomb-like carbon from by-products through simple hydrothermal treatment and high temperature KOH activation process. The obtained PCW carbon was applied as oxygen electrodes for Li-O₂ batteries. Li-O₂ batteries with PCW exhibit low discharge capacity and poor capacity retention ability. The maximum discharge capacity is 1216 mAh g^{-1} and the capacity is only 331 mAh g^{-1} after nine cycles (current density: 50 mA g^{-1}). This indicates that PCW possesses poor electrochemical activity. The poor electrochemical activity can be ascribed to its small pore size and plentiful O-containing surface groups (O, 8.4 at%). The micropores of PCW are too small for the deposition of discharge products and easy to be blocked. The plentiful O-containing surface groups can aggravate side reactions between discharge products and carbon. Raman is a common and efficient method to characterize the structure evolution of carbon during the ORR/OER process. The graphitization degree of PCW dramatically decreased after discharge, which is harmful for long term cycling. The dramatically decrease of graphitization degree can be ascribed to the existing of plentiful O-containing functional groups, which can be easily attacked by LiO₂ species. Moreover, there is an increase of fragments or functional groups in the amorphous phase after discharge, which is ascribed to the side reactions during battery cycling. 3D rGO nanosheets with meso/macro-pores were also applied to investigate its electrochemical activity in Li-O₂ batteries.

5. Summary

The rGO based battery delivers a maximum discharge capacity of 4866 mAh g⁻¹, and the discharge capacity is 3200 mAh g⁻¹ at the ninth cycle (current density: 100 mA g⁻¹). When increase the current density to 250 mA g⁻¹, rGO based cell can only deliver an initial discharge capacity of 1911 mAh g⁻¹ and the capacity is 1111 mAh g⁻¹ after nine cycles. Though rGO based batteries exhibit much higher capacity and capacity retention ability than PCW based batteries, the capacity retention ability is still very low. Compared to PCW, rGO exhibits less decrease of graphitization degree during discharge process. This can be ascribed to its lower O content (1.7 at%). However, there is still an obvious increase of fragments or functional groups in the amorphous phase after discharge. The discharge products of rGO based batteries form a passivation film, which covered on the electrode surface. This passivation film obstructs the free transportation of electrolyte, oxygen, and electrons during cycling, which will reduce the deep discharge capacity, rate ability and cycleability.

In order to enhance the capacity and cycleability, solid cathode catalysts (MnO₂ and Co₃O₄) were applied to improve the catalytic activity. MnO₂@rGO used in this work is synthesized from a simple neutral solution reaction between KMnO₄ and rGO. MnO₂ content in MnO₂@rGO composite is 8.85 wt%. These MnO₂ particles grow uniformly on rGO surface with the particle size smaller than 20 nm. The oxidation state of Mn in MnO₂ nanoparticles contain Mn⁴⁺ and Mn³⁺, where Mn³⁺ is plentiful preferably on the surface. When MnO₂@rGO was applied as oxygen electrodes for Li-O₂ batteries, it delivers an initial discharge capacity of 5139 mAh g⁻¹ (rGO, 4866 mAh g⁻¹), and the discharge capacity remains 4262 mAh g⁻¹ (rGO, 2597 mAh g⁻¹) after fifteen full discharge-charge cycles at a current density of 100 mA g⁻¹. Though MnO₂ content is very low, the discharge capacity of MnO₂@rGO based batteries decays very less (80% capacity retention) during the 15 cycles. Moreover, the charge voltage is reduced by 0.2 V compared to pure rGO based battery. Different from the formation of film for rGO, the discharge products of MnO₂@rGO based battery is a fine grained mossy deposition. This is beneficial for the transportation of electrolyte and oxygen during cycling. Compared to pure rGO, MnO₂@rGO exhibits less increase of fragments or functional groups in the amorphous phase after discharge, which indicates less side reactions during battery cycling. The enhanced electrochemical performance of MnO₂@rGO based batteries can be ascribed to the following reasons. Firstly, the high rGO content assures a good electron conductivity, which facilitates electron transfer. Secondly, the 3D porous graphene frameworks made of multiple layers provides a matrix with high surface area for the deposition of discharge products. Thirdly, the porous structure also

5. Summary

promises good transport properties for ionic and oxygen diffusion inside the electrode. Fourthly, the nano-sized MnO_2 (smaller than 20 nm) improves the catalytic activity of the surface which leads to higher interfacial current densities and shorter reaction times. Further, the surface transport of LiO_2 species is enhanced by MnO_2 . Both aspects contribute to the formation of a thin film of uniformly distributed discharged products of small particle size, which can be easily decomposed during charge. Further, we found evidence for the reversible transition of manganese oxide into lithiated manganese oxide during discharge, which forms interaction between discharge products and catalysts. This transition, which involves the incorporation of lithium and oxygen, seems to play an important role for the catalytic activity of MnO_2 and hence the reduction of the electron transfer resistance of the OER.

Co_3O_4 nanoparticles were synthesized from simple hydrothermal and high-temperature calcination process. The as-prepared Co_3O_4 has a face-centered cubic (fcc) spinel Co_3O_4 crystalline structure. When Co_3O_4 is applied as cathode catalysts for Li- O_2 battery, it delivers a maximum discharge capacity of 3625 mAh g^{-1} ($9426 \text{ mAh g}_{\text{rGO}}^{-1}$). The discharge capacity is still 1933 mAh g^{-1} ($5027 \text{ mAh g}_{\text{rGO}}^{-1}$) after 9 cycles (current density: 250 mA g^{-1}). Moreover, the battery catalyzed by $\text{Co}_3\text{O}_4/\text{rGO}$ presents unique cycling stability of 125 cycles with a constant cut-off capacity of $1000 \text{ mAh g}_{\text{rGO}}^{-1}$ (250 mA g^{-1}) and super rate capability when current densities increased from 100 to 1000 mA g^{-1} . The enhanced electrochemical performance can be ascribed to the synergetic effect between the Co_3O_4 nanoparticles and the rGO. The rGO framework with a multilayer porous structure provides an excellent electrical conductivity, promotes oxygen and ion diffusion, and provide large pore volume for the deposition of discharge products. Co_3O_4 nanoparticles can enhance the surface transport of LiO_2 species to promote the formation of non-aggregated and inadhesive toroids with small size (300-400 nm) in solution, which provides free pathways for the transportation of electrolyte, oxygen and electron. During discharge, batteries with Co_3O_4 catalysts exhibit less increase of fragments or functional groups in the amorphous phase, indicating less side reactions. Additionally, Co_3O_4 transform between lithiated (layered LiCoO_2) and non-lithiated (cubic spinel Co_3O_4) states during ORR and OER process, indicating the existence of interactions between discharge products and Co_3O_4 . This interaction seems to play an important role for the catalytic activity of Co_3O_4 .

It can be concluded that both solid catalysts (MnO_2 and Co_3O_4) share a common way to improve the electrochemical performance: enhancing the mass transport of LiO_2 species and undergoing

5. Summary

lithiated and non-lithiated reaction during discharge and charge process to promote the electron transfer from discharge products to catalysts.

Though the applied solid catalysts made a great improvement for the electrochemical performance of Li-O₂ batteries, the catalytically active region was limited to the immobile area next to the interface between the catalysts and the discharge products (solid-solid interface). In this thesis, we applied LiI (OER catalyst) and DBBQ (ORR catalyst) in the electrolyte for Li-O₂ batteries and investigated their influence. The battery without LiI and DBBQ exhibits low discharge capacity and poor capacity retention. With the addition of LiI, the battery shows a significantly enhanced capacity retention but still possesses a rather low discharge capacity. This improvement can be ascribed to the decreased decomposition voltage of LiOH catalyzed by LiI. LiI can reduce the decomposition voltage of LiOH through the oxidation reaction of $3\text{I}^- \rightarrow \text{I}_3^- + 2\text{e}^-$ and $\text{I}_3^- \rightarrow 3/2\text{I}_2 + \text{e}^-$ and chemical reaction of $4\text{LiOH} + 6\text{I}_2 \rightarrow 4\text{LiI}_3 + \text{O}_2 + 2\text{H}_2\text{O}$. [79] In the presence of DBBQ, the discharge capacity of the battery is remarkably increased, which is due to the solution phase formation of discharge products, which overcome the limitation of surface growth. Furthermore, the formation of intermediate (LiDBBQO₂-nH₂O), which possesses a lower free energy than LiO₂, can lead to a slight increase of the discharge plateau. However, the capacity retention ability with only DBBQ in the electrolyte is still poor. The battery with the dual mediators (LiI and DBBQ) combines the advantages of these two catalysts, showing a high discharge capacity, good capacity retention, and low voltage gap. The application of both soluble ORR and OER mediators can promote the growth and decomposition of discharge products in the adjacent solution of the electrode, which overcomes the limitation caused by the scarce catalytic active region (solid-solid interface). The graphitization degree of PCW with dual soluble catalysts decreased very less during discharge process. Moreover, there is few increase of fragments or functional groups in the amorphous phase with dual soluble catalysts. This can be attributed to the formation of discharge products in solution in the presence of DBBQ.

Two kinds of carbon materials with different morphology, pore size and functional groups content are investigated as cathode for Li-O₂ batteries in this work. However, the detailed influence of each parameter on the electrochemical activity did not explored. The next step should study more details about the influence of those facts and find the law. We found in this work that MnO₂ and Co₃O₄ as solid catalysts for Li-O₂ batteries will forming a bridging between the discharge products and catalysts. In the next step, we need to apply more kinds of solid catalysts to investigate whether

5. Summary

this is common for all solid catalysts. It is also valuable to study the structure evolution of discharge products and cathode materials during discharge and charge process by in-situ Raman. In this thesis, we found that dual soluble catalysts will greatly improve the electrochemical performance of Li-O₂ battery. However, we did not explore the influence of cathode structure on electrochemical performance. In the next step, we should find the optimized structure of cathode material to optimize the catalysis effect of soluble catalysts.

6. Reference

6. Reference

- [1] Z. Guo, D. Zhou, X. Dong, Z. Qiu, Y. Wang, Y. Xia, Ordered hierarchical mesoporous/macroporous carbon: A high-performance catalyst for rechargeable Li-O₂ batteries, *Adv. Mater.* 25 (2013) 5668–5672. doi:10.1002/adma.201302459.
- [2] J. Zhang, Y. Zhao, X. Zhao, Z. Liu, W. Chen, Porous perovskite LaNiO₃ nanocubes as cathode catalysts for Li-O₂ batteries with low charge potential, *Sci. Rep.* 4 (2014) 6005. doi:10.1038/srep06005.
- [3] J. Lu, Y.J. Lee, X. Luo, K.C. Lau, M. Asadi, H.H. Wang, S. Brombosz, J. Wen, D. Zhai, Z. Chen, D.J. Miller, Y.S. Jeong, J.B. Park, Z.Z. Fang, B. Kumar, A. Salehi-Khojin, Y.K. Sun, L.A. Curtiss, K. Amine, A lithium-oxygen battery based on lithium superoxide, *Nature.* 529 (2016) 377–382. doi:10.1038/nature16484.
- [4] K. Liao, T. Zhang, Y. Wang, F. Li, Z. Jian, H. Yu, H. Zhou, Nanoporous Ru as a Carbon- and Binder-Free Cathode for Li-O₂ Batteries, *ChemSusChem.* 8 (2015) 1429–1434. doi:10.1002/cssc.201403371.
- [5] N.B. Aetukuri, B.D. McCloskey, J.M. García, L.E. Krupp, V. Viswanathan, A.C. Luntz, Solvating additives drive solution-mediated electrochemistry and enhance toroid growth in non-aqueous Li-O₂ batteries, *Nature Chemistry.* 7 (2015) 50–56. doi:10.1038/nchem.2132.
- [6] S.D. Park, J.M. Vohs, R.J. Gorte, Direct oxidation of hydrocarbons in a solid-oxide fuel cell, *Nature.* 404 (2000) 265–267.
- [7] F. Yang, M. Shtein, S.R. Forrest, Controlled growth of a molecular bulk heterojunction photovoltaic cell, *Nat. Mat.* 4 (2005) 37–41. doi:10.1038/nmat1285.
- [8] J. Hu, Z. Kang, F. Li, X. Huang, Graphene with three-dimensional architecture for high performance supercapacitor, *Carbon.* 67 (2013) 221–229. doi:10.1016/j.carbon.2013.09.085.
- [9] L. Zhao, Y.-S. Hu, H. Li, Z. Wang, L. Chen, Porous Li₄Ti₅O₁₂ Coated with N-Doped Carbon from Ionic Liquids for Li-Ion Batteries, *Adv. Mater.* 23 (2011) 1385–1388. doi:10.1002/adma.201003294.
- [10] Y.S. Su, A. Manthiram, Lithium-sulphur batteries with a microporous carbon paper as a bifunctional interlayer, *Nat. Commun.* 3 (2012) 1166. doi:10.1038/ncomms2163.

6. Reference

- [11] Y. Cao, Z. Wei, J. He, J. Zang, Q. Zhang, M. Zheng, Q. Dong, α -MnO₂ nanorods grown in situ on graphene as catalysts for Li-O₂ batteries with excellent electrochemical performance, *Energy Environ. Sci.* 5 (2012) 9765–9768. doi:10.1039/c2ee23475k.
- [12] Q.C. Liu, J.J. Xu, Z.W. Chang, D. Xu, Y. Bin Yin, X.Y. Yang, T. Liu, Y.S. Jiang, J.M. Yan, X.B. Zhang, Growth of Ru-Modified Co₃O₄ Nanosheets on Carbon Textiles toward Flexible and Efficient Cathodes for Flexible Li-O₂ Batteries, *Part. Part. Syst. Charact.* 33 (2016) 500–505. doi:10.1002/ppsc.201500193.
- [13] Q. Liu, Y. Jiang, J. Xu, D. Xu, Z. Chang, Y. Yin, W. Liu, X. Zhang, Hierarchical Co₃O₄ porous nanowires as an efficient bifunctional cathode catalyst for long life Li-O₂ batteries, *Nano Res.* 8 (2015) 576–583. doi:10.1007/s12274-014-0689-3.
- [14] J. Shui, Y. Lin, J.W. Connell, J. Xu, X. Fan, L. Dai, Nitrogen-Doped Holey Graphene for High-Performance Rechargeable Li-O₂ Batteries, *ACS Energy Lett.* 1 (2016) 260–265. doi:10.1021/acseenergylett.6b00128.
- [15] C.T. Zhao, C. Yu, S.H. Liu, J. Yang, X.M. Fan, H.W. Huang, J. Qiu, 3D Porous N-Doped Graphene Frameworks Made of Interconnected Nanocages for Ultrahigh-Rate and Long-Life Li-O₂ Batteries, *Adv. Funct. Mater.* 25 (2015) 6913–6920. doi:10.1002/adfm.201503077.
- [16] X. Gao, Y. Chen, L. Johnson, P.G. Bruce, Promoting solution phase discharge in Li-O₂ batteries containing weakly solvating electrolyte solutions, *Nat. Mat.* 15 (2016) 882–888. doi:10.1038/nmat4629.
- [17] D. Zhai, H.H. Wang, J. Yang, K.C. Lau, K. Li, K. Amine, L.A. Curtiss, Disproportionation in Li-O₂ batteries based on a large surface area carbon cathode, *J. Am. Chem. Soc.* 135 (2013) 15364–15372. doi:10.1021/ja403199d.
- [18] D. Zhai, K.C. Lau, H.-H. Wang, J. Wen, D.J. Miller, J. Lu, F. Kang, B. Li, W. Yang, J. Gao, E. Indacochea, L.A. Curtiss, K. Amine, Interfacial Effects on Lithium Superoxide Disproportionation in Li-O₂ Batteries, *Nano Lett.* 15 (2015) 1041–1046. doi:10.1021/nl503943z.
- [19] Y. Qin, J. Lu, P. Du, Z. Chen, Y. Ren, T. Wu, J.T. Miller, J. Wen, D.J. Miller, Z. Zhang, K. Amine, In situ fabrication of porous-carbon-supported α -MnO₂ nanorods at room temperature: application for rechargeable Li-O₂ batteries, *Energy Environ. Sci.* 6 (2013)

6. Reference

- 519–531. doi:10.1039/c2ee23621d.
- [20] S. Cai, M. Zheng, X. Lin, M. Lei, R. Yuan, Q. Dong, A Synergistic Catalytic Mechanism for Oxygen Evolution Reaction in Aprotic Li-O₂ Battery, *ACS Catal.* 8 (2018) 7983–7990. doi:10.1021/acscatal.8b02236.
- [21] L. Wang, J. Pan, Y. Zhang, X. Cheng, L. Liu, H. Peng, A Li-Air Battery with Ultralong Cycle Life in Ambient Air, *Adv. Mater.* 30 (2018) 1704378. doi:10.1002/adma.201704378.
- [22] N.B. Aetukuri, B.D. McCloskey, J.M. García, L.E. Krupp, V. Viswanathan, A.C. Luntz, Solvating additives drive solution-mediated electrochemistry and enhance toroid growth in non-aqueous Li-O₂ batteries, *Nat. Chem.* 7 (2015) 50–56. doi:10.1038/nchem.2132.
- [23] H. Huang, S. Luo, C. Liu, Q. Wang, Z. Wang, Y. Zhang, A. Hao, Y. Liu, J. Li, Y. Zhai, Y. Dai, Ag-decorated highly mesoporous Co₃O₄ nanosheets on nickel foam as an efficient free-standing cathode for Li-O₂ batteries, *J. Alloys Compd.* 726 (2017) 939–946. doi:10.1016/j.jallcom.2017.07.276.
- [24] Z. Guo, C. Li, J. Liu, Y. Wang, Y. Xia, A Long-Life Lithium-Air Battery in Ambient Air with a Polymer Electrolyte Containing a Redox Mediator, *Angew. Chem. Int. Ed.* 56 (2017) 7505–7509. doi:10.1002/anie.201701290.
- [25] M. Ara, T. Meng, G.-A. Nazri, S.O. Salley, K.Y. Simon Ng, Ternary Imidazolium-Pyrrolidinium-Based Ionic Liquid Electrolytes for Rechargeable Li-O₂ Batteries, *J. Electrochem. Soc.* 161 (2014) A1969–A1975. doi:10.1149/2.0031414jes.
- [26] B.G. Kim, J.-S. Kim, J. Min, Y.-H. Lee, J.H. Choi, M.C. Jang, S.A. Freunberger, J.W. Choi, A Moisture- and Oxygen-Impermeable Separator for Aprotic Li-O₂ Batteries, *Adv. Funct. Mater.* 26 (2016) 1747–1756. doi:10.1002/adfm.201504437.
- [27] W.J. Kwak, H.G. Jung, D. Aurbach, Y.K. Sun, Optimized Bicompartement Two Solution Cells for Effective and Stable Operation of Li-O₂ Batteries, *Adv. Energy Mater.* 7 (2017) 1701232. doi:10.1002/aenm.201701232.
- [28] M. Asadi, B. Sayahpour, P. Abbasi, A.T. Ngo, K. Karis, J.R. Jokisaari, C. Liu, B. Narayanan, M. Gerard, P. Yasaei, X. Hu, A. Mukherjee, K.C. Lau, R.S. Assary, F. Khalili-Araghi, R.F. Klie, L.A. Curtiss, A. Salehi-Khojin, A lithium-oxygen battery with a long cycle life in an air-like atmosphere, *Nature.* 555 (2018) 502–506. doi:10.1038/nature25984.
- [29] Z. Guo, X. Dong, Y. Wang, Y. Xia, A lithium air battery with a lithiated Al-carbon anode,

6. Reference

- Chem. Commun.* 51 (2015) 676–678. doi:10.1039/c4cc07315k.
- [30] X. Han, F. Cheng, C. Chen, Y. Hu, J. Chen, Uniform MnO₂ nanostructures supported on hierarchically porous carbon as efficient electrocatalysts for rechargeable Li-O₂ batteries, *Nano Res.* 8 (2014) 156–164. doi:10.1007/s12274-014-0604-y.
- [31] L. Johnson, C. Li, Z. Liu, Y. Chen, S.A. Freunberger, P.C. Ashok, B.B. Praveen, K. Dholakia, J.M. Tarascon, P.G. Bruce, The role of LiO₂ solubility in O₂ reduction in aprotic solvents and its consequences for Li-O₂ batteries, *Nat. Chem.* 6 (2014) 1091–1099. doi:10.1038/nchem.2101.
- [32] H.D. Lim, H. Song, J. Kim, H. Gwon, Y. Bae, K.Y. Park, J. Hong, H. Kim, T. Kim, Y.H. Kim, X. Lepr̄o, R. Ovalle-Robles, R.H. Baughman, K. Kang, Superior rechargeability and efficiency of lithium-oxygen batteries: Hierarchical air electrode architecture combined with a soluble catalyst, *Angew. Chem. Int. Ed.* 53 (2014) 3926–3931. doi:10.1002/anie.201400711.
- [33] T. Liu, M. Leskes, W. Yu, A.J. Moore, L. Zhou, P.M. Bayley, G. Kim, C.P. Grey, Cycling Li-O₂ batteries via LiOH formation and decomposition, *Science.* 350 (2015) 530–533. doi:10.1126/science.aac7730.
- [34] Z. Jian, P. Liu, F. Li, P. He, X. Guo, M. Chen, H. Zhou, Core-Shell-Structured CNT@RuO₂ Composite as a High-Performance Cathode Catalyst for Rechargeable Li-O₂ Batteries, *Angew. Chem. Int. Ed.* 53 (2014) 442–446. doi:10.1002/anie.201307976.
- [35] G. Zhao, R. Mo, B. Wang, L. Zhang, K. Sun, Enhanced Cyclability of Li-O₂ Batteries Based on TiO₂ Supported Cathodes with No Carbon or Binder, *Chem. Mater.* 26 (2014) 2551–2556.
- [36] J.-J. Xu, Z.-L. Wang, D. Xu, F.-Z. Meng, X.-B. Zhang, 3D ordered macroporous LaFeO₃ as efficient electrocatalyst for Li-O₂ batteries with enhanced rate capability and cyclic performance, *Energy Environ. Sci.* 7 (2014) 2213. doi:10.1039/c3ee42934b.
- [37] N. Ding, S.W. Chien, T.S.A. Hor, R. Lum, Y. Zong, Z. Liu, Influence of carbon pore size on the discharge capacity of Li-O₂ batteries, *J. Mater. Chem. A.* 2 (2014) 12433–12441. doi:10.1039/c4ta01745e.
- [38] S.H. Oh, R. Black, E. Pomerantseva, J.H. Lee, L.F. Nazar, Synthesis of a metallic mesoporous pyrochlore as a catalyst for lithium-O₂ batteries, *Nat. Chem.* 4 (2012) 1004–

6. Reference

1010. doi:10.1038/nchem.1499.
- [39] N.L.À.O. Batteries, Vertically Aligned N-Doped Coral-like Carbon Fiber Arrays as Efficient Air Electrodes for High-Performance, *ACS Nano*. 8 (2014) 3015–3022. doi:10.1021/nn500327pp.
- [40] G. Wu, N.H. MacK, W. Gao, S. Ma, R. Zhong, J. Han, J.K. Baldwin, P. Zelenay, Nitrogen-doped graphene-rich catalysts derived from heteroatom polymers for oxygen reduction in nonaqueous lithium-O₂ battery cathodes, *ACS Nano*. 6 (2012) 9764–9776. doi:10.1021/nn303275d.
- [41] J. Shui, F. Du, C. Xue, Q. Li, L. Dai, Vertically Aligned N-Doped Coral-like Carbon Fiber Arrays as Efficient Air Electrodes for High-Performance Nonaqueous Li-O₂ Batteries, *ACS Nano*. 8 (2014) 3015–3022. doi:10.1021/nn500327p.
- [42] H.D. Lim, K.Y. Park, H. Song, E.Y. Jang, H. Gwon, J. Kim, Y.H. Kim, M.D. Lima, R.O. Robles, X. Leprõ, R.H. Baughman, K. Kang, Enhanced power and rechargeability of a Li-O₂ battery based on a hierarchical-fibril CNT electrode, *Advanced Materials*. 25 (2013) 1348–1352. doi:10.1002/adma.201204018.
- [43] J. Xiao, D. Mei, X. Li, W. Xu, D. Wang, G.L. Graff, W.D. Bennett, Z. Nie, L.V. Saraf, I.A. Aksay, J. Liu, J.-G. Zhang, Hierarchically porous graphene as a lithium-air battery electrode, *Nano Lett.* 11 (2011) 5071–5078. doi:10.1021/nl203332e.
- [44] X. Han, Y. Hu, J. Yang, F. Cheng, J. Chen, Porous perovskite CaMnO₃ as an electrocatalyst for rechargeable Li-O₂ batteries, *Chem. Commun.* 50 (2014) 1497–1499. doi:10.1039/C3CC48207C.
- [45] D. Wu, Z. Guo, X. Yin, Q. Pang, B. Tu, L. Zhang, Y.-G. Wang, Q. Li, Metal-Organic Frameworks as Cathode Materials for Li-O₂ Batteries, *Adv. Mater.* 26 (2014) 3258–3262. doi:10.1002/adma.201305492.
- [46] C. Xu, B.M. Gallant, P.U. Wunderlich, T. Lohmann, J.R. Greer, Three-Dimensional Au Microlattices as Positive Electrodes for Li-O₂ Batteries, *ACS Nano*. 9 (2015) 5876–5883. doi:10.1021/acsnano.5b00443.
- [47] F. Li, D.M. Tang, Y. Chen, D. Golberg, H. Kitaura, T. Zhang, A. Yamada, H. Zhou, Ru/ITO: A carbon-free cathode for nonaqueous Li-O₂ battery, *Nano Lett.* 13 (2013) 4702–4707. doi:10.1021/nl402213h.

6. Reference

- [48] Y.C. Lu, Z. Xu, H. a. Gasteiger, S. Chen, K. Hamad-Schifferli, Y. Shao-Horn, Platinum-gold nanoparticles: A highly active bifunctional electrocatalyst for rechargeable lithium-air batteries, *J. Am. Chem. Soc.* 132 (2010) 12170–12171. doi:10.1021/ja1036572.
- [49] C. Cao, Y. Yan, H. Zhang, J. Xie, S. Zhang, B. Pan, G. Cao, X. Zhao, Controlled Growth of Li₂O₂ by Cocatalysis of Mobile Pd and Co₃O₄ Nanowire Arrays for High-Performance Li-O₂ Batteries, *ACS Appl. Mater. Interfaces.* 8 (2016) 31653–31660. doi:10.1021/acsami.6b10716.
- [50] Q. Yu, Q. Yu, W. Sun, H. Wu, Z. Wang, D. Rooney, K. Sun, Novel Ni@Co₃O₄ Web-like Nanofiber Arrays as Highly Effective Cathodes for Rechargeable Li-O₂ Batteries, *Electrochim. Acta.* 220 (2016) 654–663. doi:10.1016/j.electacta.2016.10.131.
- [51] X. Hu, Z. Zhu, F. Cheng, Z. Tao, J. Chen, Micro-nano structured Ni-MOFs as high-performance cathode catalyst for rechargeable Li-O₂ batteries, *Nanoscale.* 7 (2015) 11833–11840. doi:10.1039/c5nr02487k.
- [52] C. V Amanchukwu, M. Gauthier, T.P. Batcho, C. Symister, Y. Shao-horn, J.M.D. Arcy, P.T. Hammond, Evaluation and Stability of PEDOT Polymer Electrodes for Li-O₂ Batteries, *J. Phys. Chem. Lett.* 7 (2016) 3770–3775. doi:10.1021/acs.jpcclett.6b01986.
- [53] E. Environ, A tubular polypyrrole based air electrode with improved O₂ diffusivity for Li-O₂ batteries, *Energy Environ. Sci.* 5 (2012) 7893–7897. doi:10.1039/c2ee21638h.
- [54] X. Gao, Y. Chen, L. Johnson, P.G. Bruce, Promoting solution phase discharge in Li-O₂ batteries containing weakly solvating electrolyte solutions, *Nat. Mat.* 15 (2016) 882–888. doi:10.1038/nmat4629.
- [55] A. Nakanishi, M.L. Thomas, H.M. Kwon, Y. Kobayashi, R. Tatara, K. Ueno, K. Dokko, M. Watanabe, Electrolyte Composition in Li-O₂ Batteries with LiI Redox Mediators: Solvation Effects on Redox Potentials and Implications for Redox Shuttling, *J. Phys. Chem. C.* 122 (2018) 1522–1534. doi:10.1021/acs.jpcc.7b11859.
- [56] J. Cao, S. Liu, J. Xie, S. Zhang, G. Cao, X. Zhao, Tips-Bundled Pt/Co₃O₄ Nanowires with Directed Peripheral Growth of Li₂O₂ as Efficient Binder/Carbon-Free Catalytic Cathode for Lithium-Oxygen Battery, *ACS Catal.* 5 (2015) 241–245. doi:10.1021/cs501392p.
- [57] X. Gao, Y. Chen, L.R. Johnson, Z.P. Jovanov, P.G. Bruce, A rechargeable lithium-oxygen battery with dual mediators stabilizing the carbon cathode, *Nat. Energy.* 2 (2017) 17118.

6. Reference

- doi:10.1038/nenergy.2017.118.
- [58] Y. Ren, S. Zhang, H. Li, X. Wei, Y. Xing, Mesoporous Pd/Co₃O₄ nanosheets nanoarrays as an efficient binder/carbon free cathode for rechargeable Li-O₂ batteries, *Appl. Surf. Sci.* 420 (2017) 222–232. doi:10.1016/j.apsusc.2017.04.076.
- [59] Y. guo Huang, J. Chen, X. hui Zhang, Y. hui Zan, X. ming Wu, Z. qiang He, H. qiang Wang, Q. yu Li, Three-dimensional Co₃O₄/CNTs/CFP composite as binder-free cathode for rechargeable Li-O₂ batteries, *Chem. Eng. J.* 296 (2016) 28–34. doi:10.1016/j.cej.2016.03.081.
- [60] G. Zhao, J. Lv, Z. Xu, L. Zhang, K. Sun, Carbon and binder free rechargeable Li-O₂ battery cathode with Pt/Co₃O₄ flake arrays as catalyst, *J. of Power Sources.* 248 (2014) 1270–1274. doi:10.1016/j.jpowsour.2013.10.041.
- [61] T. Gu, D.A. Agyeman, S. Shin, X. Jin, J.M. Lee, a MnO₂ Nanowire-Anchored Highly Oxidized Cluster as a Catalyst for Li-O₂ Batteries : Superior Electrocatalytic Activity and High Functionality, *Angew. Chem. Int. Ed.* 57 (2018) 15984–15989. doi:10.1002/anie.201809205.
- [62] S.A. Cho, Y.J. Jang, H.D. Lim, J.E. Lee, Y.H. Jang, T.T.H. Nguyen, F.M. Mota, D.P. Fenning, K. Kang, Y. Shao-Horn, D.H. Kim, Hierarchical Porous Carbonized Co₃O₄ Inverse Opals via Combined Block Copolymer and Colloid Templating as Bifunctional Electrocatalysts in Li-O₂ Battery, *Adv. Energy Mater.* 7 (2017) 1–10. doi:10.1002/aenm.201700391.
- [63] Z. Li, S. Ganapathy, Y. Xu, Q. Zhu, W. Chen, I. Kochetkov, C. George, L.F. Nazar, M. Wagemaker, Fe₂O₃ Nanoparticle Seed Catalysts Enhance Cyclability on Deep (Dis)charge in Aprotic Li₂O₂ Batteries, *Adv. Energy Mater.* 8 (2018) 1703513. doi:10.1002/aenm.201703513.
- [64] W. Kwak, H. Kim, Y. Sun, H. Jung, D. Aurbach, A Comparative Evaluation of Redox Mediators for Li-O₂ Batteries, *J. Electrochem. Soc.* 165 (2018) 2274–2293. doi:10.1149/2.0901810jes.
- [65] F. Li, Y. Chen, D.M. Tang, Z. Jian, C. Liu, D. Golberg, A. Yamada, H. Zhou, Performance-improved Li-O₂ battery with Ru nanoparticles supported on binder-free multi-walled carbon nanotube paper as cathode, *Energy Environ. Sci.* 7 (2014) 1648–1652. doi:10.1039/

6. Reference

- c3ee44043e.
- [66] J. Liu, R. Younesi, T. Gustafsson, K. Edström, J. Zhu, Pt/ α -MnO₂ nanotube: A highly active electrocatalyst for Li-O₂ battery, *Nano Energy*. 10 (2014) 19–27. doi:10.1016/j.nanoen.2014.08.022.
- [67] Y. Lei, J. Lu, X. Luo, T. Wu, P. Du, X. Zhang, Y. Ren, J. Wen, D.J. Miller, J.T. Miller, Y.-K. Sun, J.W. Elam, K. Amine, Synthesis of Porous Carbon Supported Palladium Nanoparticle Catalysts by Atomic Layer Deposition: Application for Rechargeable Lithium-O₂ Battery, *Nano Lett.* 13 (2013) 4182–4189. doi:10.1021/nl401833p.
- [68] Y.-C. Lu, H. a. Gasteiger, Y. Shao-Horn, Catalytic Activity Trends of Oxygen Reduction Reaction for Nonaqueous Li-Air Batteries, *J. Am. Chem. Soc.* 133 (2011) 19048–19051. doi:10.1021/ja208608s.
- [69] Q. Li, P. Xu, B. Zhang, H. Tsai, J. Wang, H.-L. Wang, G. Wu, One-step synthesis of Mn₃O₄/reduced graphene oxide nanocomposites for oxygen reduction in nonaqueous Li-O₂ batteries, *Chem. Commun.* 49 (2013) 10838. doi:10.1039/c3cc46441e.
- [70] F. Li, R. Ohnishi, Y. Yamada, J. Kubota, K. Domen, A. Yamada, H. Zhou, Carbon supported TiN nanoparticles: An efficient bifunctional catalyst for non-aqueous Li-O₂ batteries, *Chem. Commun.* 49 (2013) 1175–1177. doi:10.1039/c2cc37042e.
- [71] A. Fiedler, A.P. Vogt, L. Pfaffmann, V. Trouillet, J.T. Breukelgen, R. Köppe, C. Barner-Kowollik, H. Ehrenberg, F. Scheiba, Lithium-air battery cathode modification via an unconventional thermal method employing borax, *RSC Adv.* 6 (2016) 66307–66310. doi:10.1039/c6ra05685g.
- [72] F. Li, S. Wu, D. Li, T. Zhang, P. He, A. Yamada, H. Zhou, The water catalysis at oxygen cathodes of lithium-oxygen cells, *Nat. Commun.* 6 (2015) 7843. doi:10.1038/ncomms8843.
- [73] N.B. Aetukuri, B.D. McCloskey, J.M. García, L.E. Krupp, V. Viswanathan, A.C. Luntz, Solvating additives drive solution-mediated electrochemistry and enhance toroid growth in non-aqueous Li-O₂ batteries, *Nat. Chem.* 7 (2015) 50–56. doi:10.1038/nchem.2132.
- [74] L. Yang, J.T. Frith, J.R. Owen, A new method to prevent degradation of lithium – oxygen batteries : reduction of superoxide by viologen, *Chem. Commun.* 51 (2015) 1705–1708. doi:10.1039/C4CC09208B.
- [75] X. Shen, S. Zhang, Y. Wu, Y. Chen, Promoting Li-O₂ Batteries With Redox Mediators,

6. Reference

- ChemSusChem*. 12 (2019) 104–114. doi:10.1002/cssc.201802007.
- [76] T. Liu, M. Leskes, W. Yu, A.J. Moore, L. Zhou, P.M. Bayley, G. Kim, C.P. Grey, Cycling Li-O₂ batteries via LiOH formation and decomposition, *Science*. 350 (2015) 530–533. doi:10.1126/science.aac7730.
- [77] S. Meini, M. Piana, N. Tsiouvaras, A. Garsuch, H.A. Gasteiger, The Effect of Water on the Discharge Capacity of a Non-Catalyzed Carbon Cathode for Li-O₂ Batteries, *Electrochem. and Solid State Lett.* 15 (2012) A45–A48. doi:10.1149/2.005204esl.
- [78] T. Liu, J.T. Frith, G. Kim, R.N. Kerber, N. Dubouis, Y. Shao, Z. Liu, P.C.M.M. Magusin, M.T.L. Casford, N. Garcia-Araez, C.P. Grey, The Effect of Water on Quinone Redox Mediators in Nonaqueous Li-O₂ Batteries, *J. Am. Chem. Soc.* 140 (2018) 1428–1437. doi:10.1021/jacs.7b11007.
- [79] Y.G. Zhu, Q. Liu, Y. Rong, H. Chen, J. Yang, C. Jia, L.J. Yu, A. Karton, Y. Ren, X. Xu, S. Adams, Q. Wang, Proton enhanced dynamic battery chemistry for aprotic lithium-oxygen batteries, *Nat. Commun.* 8 (2017) 14308. doi:10.1038/ncomms14308.
- [80] M. Tułodziecki, G.M. Leverick, C. V. Amanchukwu, Y. Katayama, D.G. Kwabi, F. Bardé, P.T. Hammond, Y. Shao-Horn, The role of iodide in the formation of lithium hydroxide in lithium-oxygen batteries, *Energy Environ. Sci.* 10 (2017) 1828–1842. doi:10.1039/c7ee00954b.
- [81] C.M. Burke, R. Black, I.R. Kochetkov, V. Giordani, D. Addison, L.F. Nazar, B.D. McCloskey, Implications of 4e Oxygen Reduction via Iodide Redox Mediation in Li-O₂ Batteries, *ACS Energy Lett.* 1 (2016) 747–756. doi:10.1021/acsenergylett.6b00328.
- [82] Y. Qiao, S. Wu, Y. Sun, S. Guo, J. Yi, P. He, H. Zhou, Unraveling the Complex Role of Iodide Additives in Li-O₂ Batteries, *ACS Energy Lett.* 2 (2017) 1869–1878. doi:10.1021/acsenergylett.7b00462.
- [83] H. Yang, Q. Wang, R. Zhang, B.D. Trimm, M.S. Whittingham, The electrochemical behaviour of TTF in Li-O₂ batteries using a TEGDME-based electrolyte, *Chem. Commun.* 52 (2016) 7580–7583. doi:10.1039/c6cc01120a.
- [84] Y. Chen, S. a. Freunberger, Z. Peng, O. Fontaine, P.G. Bruce, Charging a Li-O₂ battery using a redox mediator, *Nat. Chem.* 5 (2013) 489–494. doi:10.1038/nchem.1646.
- [85] J. Han, G. Huang, Y. Ito, X. Guo, T. Fujita, P. Liu, A. Hirata, M. Chen, Full Performance

6. Reference

- Nanoporous Graphene Based Li-O₂ Batteries through Solution Phase Oxygen Reduction and Redox-Additive Mediated Li₂O₂ Oxidation, *Adv. Energy Mater.* 7 (2017) 1601933. doi:10.1002/aenm.201601933.
- [86] W. Kwak, S.H. Ha, D.H. Kim, K.H. Shin, Y. Sun, Y.J. Lee, Synergistic Integration of Soluble Catalysts with Carbon-Free Electrodes for Li-O₂ Batteries, *ACS Catal.* 7 (2017) 8192–8199. doi:10.1021/acscatal.7b02359.
- [87] Y.G. Zhu, C. Jia, J. Yang, F. Pan, Q. Huang, Q. Wang, Dual redox catalysts for oxygen reduction and evolution reactions: Towards a redox flow Li-O₂ battery, *Chem. Commun.* 51 (2015) 9451–9454. doi:10.1039/c5cc01616a.
- [88] T. Liu, Z. Liu, G. Kim, J.T. Frith, N. Garcia-Araez, C.P. Grey, Understanding LiOH Chemistry in a Ruthenium-Catalyzed Li-O₂ Battery, *Angew. Chem. Int. Ed.* 56 (2017) 16057–16062. doi:10.1002/anie.201709886.
- [89] R. Tellgren, Neutron Powder Diffraction in Sweden., *Phys. B.* 26 A (1985) 55–69.
- [90] B. Ravel, M. Newville, ATHENA, ARTEMIS, HEPHAESTUS: Data analysis for X-ray absorption spectroscopy using IFEFFIT, *J. Synchrotron Rad.* 12 (2005) 537–541. doi:10.1107/S0909049505012719.
- [91] M.C. Liu, L. Bin Kong, P. Zhang, Y.C. Luo, L. Kang, Porous wood carbon monolith for high-performance supercapacitors, *Electrochim. Acta.* 60 (2012) 443–448. doi:10.1016/j.electacta.2011.11.100.
- [92] W. Tian, Q. Gao, Y. Tan, K. Yang, L. Zhu, C. Yang, H. Zhang, Bio-inspired beehive-like hierarchical nanoporous carbon derived from bamboo-based industrial by-product as a high performance supercapacitor electrode material, *J. Mater. Chem. A.* 3 (2015) 5656–5664. doi:10.1039/c4ta06620k.
- [93] J. Wang, S. Kaskel, KOH activation of carbon-based materials for energy storage, *J. Mater. Chem.* 22 (2012) 23710. doi:10.1039/c2jm34066f.
- [94] J. Hou, C. Cao, F. Idrees, X. Ma, Hierarchical porous nitrogen-doped carbon nanosheets derived from silk for ultrahigh-capacity battery anodes and supercapacitors, *ACS Nano.* 9 (2015) 2556–2564. doi:10.1021/nm506394r.
- [95] L. Zhu, Q. Gao, Y. Tan, W. Tian, J. Xu, K. Yang, C. Yang, Nitrogen and oxygen co-doped microporous carbons derived from the leaves of *Euonymus japonicas* as high performance

6. Reference

- supercapacitor electrode material, *Micropor. Mesopor. Mater.* 210 (2015) 1–9. doi:10.1016/j.micromeso.2015.02.014.
- [96] W. Tian, Q. Gao, Y. Tan, Y. Zhang, J. Xu, Z. Li, K. Yang, L. Zhu, Z. Liu, Three-dimensional functionalized graphenes with systematical control over the interconnected pores and surface functional groups for high energy performance supercapacitors, *Carbon*. 85 (2015) 351–362. doi:10.1016/j.carbon.2015.01.001.
- [97] M.S. Dresselhaus, G. Dresselhaus, R. Saito, A. Jorio, Raman spectroscopy of carbon nanotubes, *Phys. Rep.* 409 (2005) 47–49. doi:10.1016/j.physrep.2004.10.006.
- [98] A.C. Ferrari, Raman spectroscopy of graphene and graphite: Disorder, electron-phonon coupling, doping and nonadiabatic effects, *Solid State Commun.* 143 (2007) 47–57. doi:10.1016/j.ssc.2007.03.052.
- [99] A. Sadezky, H. Muckenhuber, H. Grothe, R. Niessner, U. Pöschl, Raman microspectroscopy of soot and related carbonaceous materials: Spectral analysis and structural information, *Carbon*. 43 (2005) 1731–1742. doi:10.1016/j.carbon.2005.02.018.
- [100] G. Xin, Y. Wang, J. Zhang, S. Jia, J. Zang, Y. Wang, A self-supporting graphene/MnO₂ composite for high-performance supercapacitors, *Int. J. Hydrogen Energy*. 40 (2015) 10176–10184. doi:10.1016/j.ijhydene.2015.06.060.
- [101] Y. Wang, H. Guan, S. Du, Y. Wang, A facile hydrothermal synthesis of MnO₂ nanorod reduced graphene oxide nanocomposites possessing excellent microwave absorption properties, *RSC Adv.* 5 (2015) 88979–88988. doi:10.1039/C5RA15165A.
- [102] M.C. Biesinger, B.P. Payne, A.P. Grosvenor, L.W.M. Lau, A.R. Gerson, R. St. C. Smart, Resolving surface chemical states in XPS analysis of first row transition metals, oxides and hydroxides: Cr, Mn, Fe, Co and Ni, *Appl. Surf. Sci.* 257 (2011) 2717–2730. doi:10.1016/j.apsusc.2010.10.051.
- [103] R. Azmi, S. Ulrich, Surface analytical approaches to reliably characterize lithium ion battery electrodes, *Surf Interface Anal.* 50 (2017) 43–51. doi:10.1002/sia.6330.
- [104] F. Wang, Z. Wen, C. Shen, X. Wu, J. Liu, Synthesis of α -MnO₂ nanowires modified by Co₃O₄ nanoparticles as a high-performance catalyst for rechargeable Li-O₂ batteries, *Phys. Chem. Chem. Phys.* 18 (2016) 926–931. doi:10.1039/C5CP06815K.
- [105] R. Black, J.H. Lee, B. Adams, C. a. Mims, L.F. Nazar, The role of catalysts and peroxide

6. Reference

- oxidation in lithium-oxygen batteries, *Angew. Chem. Int. Ed.* 52 (2013) 392–396. doi:10.1002/anie.201205354.
- [106] Q. Wu, V.A. Maroni, D.J. Gosztola, D.J. Miller, D.W. Dees, W. Lu, A Raman-Based Investigation of the Fate of Li_2MnO_3 in Lithium- and Manganese-Rich Cathode Materials for Lithium Ion Batteries, *J. Electrochem. Soc.* 162 (2015) A1255–A1264. doi:10.1149/2.0631507jes.
- [107] C. V Ramana, M. Massot, C.M. Julien, XPS and Raman spectroscopic characterization of LiMn_2O_4 spinels, *Surf. Interface Anal.* 37 (2020) 412–416. doi:10.1002/sia.2022.
- [108] J. Zhu, X. Ren, J. Liu, W. Zhang, Z. Wen, Unraveling the Catalytic Mechanism of Co_3O_4 for the Oxygen Evolution Reaction in a Li- O_2 Battery, *ACS Catal.* 5 (2015) 73–81. doi:10.1021/cs5014442.
- [109] Y. Tan, Q. Gao, C. Yang, K. Yang, W. Tian, L. Zhu, One-dimensional porous nanofibers of Co_3O_4 on the carbon matrix from human hair with superior lithium ion storage performance, *Sci. Rep.* 5 (2015) 12382. doi:10.1038/srep12382.
- [110] V.G. Hadjiev, M.N. Iliev, I. V. Vergilov, The Raman spectra of Co_3O_4 , *J. Phys. C: Solid State Phys.* 21 (1988) L199–L201. doi:10.1088/0022-3719/21/7/007.
- [111] S. Deng, N. Chen, D. Deng, Y. Li, X. Xing, Y. Wang, Meso- and macroporous coral-like Co_3O_4 for VOCs gas sensor, *Ceram. Int.* 41 (2015) 11004–11012. doi:10.1016/j.ceramint.2015.05.045.
- [112] D.G. Kwabi, T.P. Batcho, S. Feng, L. Giordano, C. V. Thompson, Y. Shao-Horn, The effect of water on discharge product growth and chemistry in Li- O_2 batteries, *Phys. Chem. Chem. Phys.* 18 (2016) 24944–24953. doi:10.1039/c6cp03695c.
- [113] C. Yan, G. Chen, X. Zhou, J. Sun, C. Lv, Template-Based Engineering of Carbon-Doped Co_3O_4 Hollow Nanofibers as Anode Materials for Lithium-Ion Batteries, *Adv. Funct. Mater.* 26 (2016) 1428–1436. doi:10.1002/adfm.201504695.
- [114] B.M. Weckhuysen, I.E. Wachs, C.A. Roberts, In-situ characterization of heterogeneous catalysts themed issue spectroscopy, *Chem. Soc. Rev.* 39 (2010) 5002–5017. doi:10.1039/c0cs00145g.
- [115] T. Nishi, H. Nakai, A. Kita, Visualization of the State-of-Charge Distribution in a LiCoO_2 Cathode by In Situ Raman Imaging, *J. Electrochem. Soc.* 160 (2013) 1785–1788.

6. Reference

- doi:10.1149/2.061310jes.
- [116] J. Inamoto, T. Fukutsuka, K. Miyazaki, T. Abe, Investigation of the Surface State of LiCoO₂ Thin-Film Electrodes Using a Redox Reaction of Ferrocene, *J. Electrochem. Soc.* 164 (2017) 555–559. doi:10.1149/2.0321704jes.
- [117] W. Hua, B. Schwarz, M. Knapp, A. Senyshyn, A. Missiul, X. Mu, S. Wang, C. Kübel, J.R. Binder, S. Indris, H. Ehrenberg, (De)Lithiation Mechanism of Hierarchically Layered LiNi_{1/3}Co_{1/3}Mn_{1/3}O₂ Cathodes during High-Voltage Cycling, *J. Electrochem. Soc.* 166 (2018) A5025–A5032. doi:10.1149/2.0051903jes.
- [118] S. Zhang, G. Wang, J. Jin, L. Zhang, Z. Wen, J. Yang, Self-catalyzed decomposition of discharge products on the oxygen vacancy sites of MoO₃ nanosheets for low-overpotential Li-O₂ batteries, *Nano Energy*. 36 (2017) 186–196. doi:10.1016/j.nanoen.2017.04.038.
- [119] A.E. Torres, P.B. Balbuena, Exploring the LiOH Formation Reaction Mechanism in Lithium-Air Batteries, *Chem. Mater.* 30 (2018) 708–717. doi:10.1021/acs.chemmater.7b04018.
- [120] Z. Zhang, J. Bao, C. He, Y. Chen, J. Wei, Z. Zhou, Hierarchical carbon-nitrogen architectures with both mesopores and macrochannels as excellent cathodes for rechargeable Li-O₂ batteries, *Adv. Funct. Mater.* 24 (2014) 6826–6833. doi:10.1002/adfm.201401581.

7. Appendix

7. Appendix

7.1 List of Abbreviations

AN	Acetonitril
LiTFSI	Lithium Bis(trifluoromethanesulfonyl)imide
TEGDME	Tetraethylene glycol dimethyl ether
DBBQ	2,5-di-tert-butyl- 1,4-benzoquinone
PVDF	Polyvinylidenfluorid
NMP	N-Methyl-2-pyrrolidon
SEM	Scanning Electron Microscope
XRD	X-ray diffraction
TG	Thermal Analysis
XPS	X-ray photoelectron spectroscopy
BET	Brunauer–Emmett–Teller
DFT	Density Functional Theory
PYR14TFSI	1-butyl-1-methylpyrrolidinium bis(trifluoromethanesulfonyl)imide
BMIMTFSI	1-butyl-3-methylimidazolium bis(trifluoromethylsulfonyl)imide
ORR	Oxygen reduction reaction
OER	Oxygen evolution reaction
DN	High-donor-number
CV	Cyclic Voltammetry
TEM	Transmission electron microscope
ITO	indium tin oxide
rGO	reduced graphene oxides
Li-O ₂ battery	Lithium-oxygen battery
LiI	Lithium iodide
ICSD	Inorganic Crystal Structure Database
SEAD	Selected area (electron) diffraction
CNT	Carbon nanotube
Ru@MWCNTP	Ru nanoparticles doped multi-walled carbon nanotube paper

7. Appendix

HR(TEM)	High resolution transmission electron microscope
N-rGO	Nitrogen doped reduced graphene oxides
RM	Redox mediator
GPE	Gel polymer electrolyte
MOFs	Metal organic frameworks
3D	Three Dimension
NMR	Nuclear Magnetic Resonance
SEI	Solid electrolyte interface
MnO _x	Manganese oxides
MMCSAs	Mesoporous/Macroporous carbons
CNF	Carbon Nanofiber
NPGAs	Nitrogen doped graphene aerogels
HPC	Hierarchically porous carbon
Va-NCCF	Vertically aligned coral like carbon nanofiber
PE	Porous polyethylene
PU	Poly- urethane
GF	Glass fiber
ALD	Atomic layer deposition
FE-SEM	Multi- functional Field-Emission Scanning Electron Microscope
PEI	Poly(ethylenimine)
PEI-AQ	Immobilized Poly(ethylenimine)
TTF	Tetrathiafulvalene

7. Appendix

7.2 Posters

1. **L. Zhu**, F. Scheiba*, and H. Ehrenberg. Interlinked Carbon Nanospheres Prepared from Green Chemistry Method for High Performance Lithium Ion Batteries. LIBD. (2017).
2. **L. Zhu**, F. Scheiba*, and H. Ehrenberg. Co₃O₄/rGO Composites as Efficient Catalysts for Rechargeable Li-O₂ Batteries. 2018 Conference on Chemistry of Energy Materials. (2018)

7.3 Publications

1. **L. Zhu**, F. Scheiba, V. Trouillet, M. Georgian, Q. Fu, A. Sarapulova, F. Sigel, W. Hua and H. Ehrenberg, MnO₂ and Reduced Graphene Oxide as Bifunctional Electrocatalysts for Li-O₂ Batteries. *ACS Appl. Energy Mater.* **2019**, 2, 7121-7131.
2. Q. Fu, A. Sarapulova, V. Trouillet, **L. Zhu**, F. Fauth, S. Mangold, E. Welter, S. Indris, M. Knapp, S. Dsoke, N. Bramnik, and H. Ehrenberg. In Operando Synchrotron Diffraction and in Operando X-ray Absorption Spectroscopy Investigations of Orthorhombic V₂O₅ Nanowires as Cathode Materials for Mg-Ion Batteries. *J. Am. Chem. Soc.* **2019**, 141, 2305-2315.
3. G. Tian, Z. Zhao, A. Sarapulova, C. Das, **L. Zhu**, S. Liu, Dsoke, and etc. (2019). Understanding the Li-Ion Storage Mechanism in a Carbon Compositing Zinc Sulfide Electrode. *J. Mater. Chem. A* (2019), DOI: 10.1039/c9ta01382b
4. K. Yang, Q. Gao, Y. Tan, W. Tian, W. Qian, **L. Zhu**, and C. Yang. Biomass-Derived Porous Carbon with Micropores and Small Mesopores for High-Performance Lithium-Sulfur Batteries. *Chem. Eur. J.* **2016**, 22, 3239-3244.
5. W. Qian, Q. Gao, K. Yang, W. Tian, Y. Tan, C. Yang, H. Zhang, Z. Li, **L. Zhu**. 3D Hierarchically Interconnected Porous Graphene Containing Sulfur for Stable High Rate Li-S Batteries. *Energy Technol.* **2016**, 4, 625-632.

8. Acknowledgements

8. Acknowledgements

At this moment, the writing of my thesis is nearly the end. Now I am nervous and expectant. Looking back the past, many memories come to my mind. During the PhD period, there is happiness time from success and also frustrated time from failure. For sure, I am lucky enough to do the research job as I wanted. Many things and people deserve to be remembered during this period. I would like to thank all the people who helped me during my PhD period.

First of all, I would like to thank my parents and older sister. They give me all their love since I came to this world. They encouraged me when I came across frustration. They are the first teacher of me, teaching me to be brave, confident and loving.

I would like to thank my country and the CSC program. They gave me an opportunity to continue my research abroad. They gave me trust during my PhD time in Germany.

My sincere thank goes to my supervisor Prof. Dr. Helmut Ehrenberg. He gave me a chance to study in IAM-ESS and continues supporting during my PhD period. His prudent scientific attitude and vast knowledge reserve inspire me all through my research.

I would particularly like to thank Dr. Frieder Scheiba, who is my direct mentor. He supported me a lot and gave me expert guidance during my research. He is a good teacher for me at work and also good friend in life.

I am also willing to thank Dr. Michael Knapp and Dr. Angelina Sarapulova. Dr. Michael Knapp is always patient to help me solve problems during XRD test. Dr. Angelina Sarapulova helps me to have a deep understanding of XRD refinement.

I thank Guiying Tian, Qiang Fu and Weibo Hua, who gave me help since I came to Germany. They are very knowledgeable and often communicate with me about my scientific work.

I am also very grateful to Heinz-Robert Goebel and Liuda Mereacre, who gave me a lot of technical supports.

At last, I give my heartfelt thanks to all the people in our institute. I cannot write down all the thanks here, but I remember all the help, love and encouragement.